Metal Oxide/Hydroxide - Graphene Nanocomposite Materials: Preparation and Catalytic Applications

Thesis submitted to the
University of Calicut in partial fulfillment of
the requirements for the degree of

DOCTOR OF PHILOSOPHY IN CHEMISTRY
in the Faculty of Science

By

SHANIBA C.P.

Research and Post Graduate Department of Chemistry
Sree Neelakanta Government Sanskrit College
Pattambi
(Affiliated to University of Calicut, Kerala, India)

2018

Sree Neelakanta Govt. Sanskrit College
Pattambi, Palakkad Dt, Kerala - 679 306
(Accredited by NAAC with A Grade)
Ph: 0466-2212223 e-mail: sngscollege@gmail.com
Website: www.sngscollege.org

CERTIFICATE

Certified that the research work presented in the thesis entitled **"Metal Oxide/Hydroxide - Graphene Nanocomposite Materials: Preparation and Catalytic Applications"** is an authentic record of research work carried out by **Shaniba C. P.** under my supervision at the Department of Chemistry, Sree Neelakanta Govt. Sanskrit College, Pattambi, in partial fulfillment of the requirements for the degree of Doctor of Philosophy in Chemistry and no part thereof has been included for the award of any other degree.

Place: Pattambi
Date:

Dr. Resmi M. R.
(Supervising Guide)
Research and Post Graduate
Department of Chemistry
S.N.G.S. College, Pattambi

Sree Neelakanta Govt. Sanskrit College
Pattambi, Palakkad Dt, Kerala - 679 306
(Accredited by NAAC with A Grade)
Ph: 0466-2212223 e-mail: sngscollege@gmail.com
Website: www.sngscollege.org

CERTIFICATE

This is to certify that the thesis entitled **"Metal Oxide/Hydroxide-GrapheneNanocomposite Materials: Preparation and Catalytic Applications"** bound herewith is a bonafide work done by Ms.Shaniba.C.P under my guidance in the Department of Chemistry, S.N.G.S. College,Pattambi. I also certify that the corrections/ suggestions from the adjudicators have been incorporated in the revised thesis.

Place: Pattambi
Date:

Dr. Resmi M. R.
(Supervising Guide)
Research and Post Graduate
Department of Chemistry
S.N.G.S. College, Pattambi

DECLARATION

I hereby declare that the thesis entitled **"Metal Oxide/Hydroxide - Graphene Nanocomposite Materials: Preparation and Catalytic Applications"** is the bonafide report of the original work carried out by me under the supervision of **Dr. Resmi M. R.** at the Department of Chemistry, Sree Neelakanta Govt. Sanskrit College, Pattambi, and no part thereof has been included in any other thesis submitted previously for the award of any degree.

Place: Pattambi **Shaniba C. P.**

Date:

Dedicated To

My
Uppa,Umma, Rafi
Jinumol, Monutten, Saidutty sir
&
Resmi Teacher

ACKNOWLEDGEMENTS

I begin my hearty gratitude towards God for his amazing grace of blessing in my life which cannot be expressed or limited to a single word. I feel highly blessed by Almighty the Supreme who controls all of us.

A number of people have directly and indirectly assisted and contributed to the successful completion of this Ph.D work and I thank them all. In particular, I am proud to express my deep sense of gratitude to ***Dr. M. R. Resmi,*** *Asst. Professor, Department of Chemistry, Sree Neelakanta Govt. Sanskrit College, for being my supervising guide and also for giving me proper encouragement throughout the work. Her meticulous dynamic guidance, scholastic suggestions, constant encouragement and comprehensive discussions at every stage have helped me to bring the work to a satisfactory completion.*

I express my gratitude to ***Dr. P. Venugopalan****, Head, Department of Chemistry, SNGS College, Pattambi for providing the necessary library and laboratory facilities and all other faculty members Anjaly teacher, Femina teacher,Vinod sir, Manoj sir, Binitha teacher, Roy sir, Remani teacher, Usha teacher and Jincy teacher for their constant encouragement andvaluable advices on time.*

I extend my gratitude to the non-teaching staff Surettan, Raghuvettan, Vijayalakshmi chechi, Syamalechi, Usha chechi, Mohanettan, Rasikikka, Saidikka and Babuettan for their unconditional love, help and support.

I would like to thank Sudheeshettan (Labplanet) for his timely support to overcome the technical problems and for supplying chemicals.

I thank Sandeep for his help and support during my banglore days.

I am thankful to Dr. Sheela S, Principal, SNGS College Pattambi and also the former Principals Dr. Suma K. K, Prof. AnithaKumari P.N, Prof. P.

M. Raghavan and Dr. K. Premalatha. My acknowledgement will never be completed without memorising the former principal Prof. M. P. Raveendrakumar (Late), who helped a lot in the different stages of my research work.

I thank administrative staff especially Reji sir (HA), Reghu sir (superintend) in the SNGS College for clearing official procedures as early as possible.

My sincere thanks to University of Calicut for upgrading SNGS College as a research centre and providing me a golden opportunity to do PhD here.

I express my genuine thanks to Dr. N. K. Renuka, Dr. M Sathian, the doctoral committee members.

My special thanks to ***Dr. P. Raveendran****, HOD, Department of Chemistry, University of Calicut for his support, help during writing the papers and throughout the PhD work.*

I am extremely indebted to ***Dr. P. Muhammed Ashraf,*** *Principal Scientist, Fishing Technology Division, ICAR - Central Institute of Fisheries Technology, Cochin, for his significant support in analyzing the data and valuable suggestions in finalizing my research work. Thanks don't seem sufficient but it is said with appreciation and respect to him for his support, encouragement and understanding.*

I would like to thank ***Dr. T. Pradeep****, Professor in Chemistry, IIT Madras, for analyzing TEM in critical situation.*

I warmly thank ***Dr. Sampath****, Sr. Scientist, I.I.Sc., Bangalore for his whole hearted support, encouragement, advice in analyzing the data and sparing his valuable time for discussions.*

I take this opportunity to sincerely express my thanks to Dr. Paulson Mathew, Asst. Professor, St. Thomas College, Thrissur, for his timely help in doing the GC-MS analysis and advice.

My special thanks to Dr. Shibu M Eappen, Dr. Akash for helping in various characterizations of the prepared catalysts. I am thankful to SAIF-STIC, Cochin for various sample analysis.

My uppa, umma have been the constant source of affection, support and encouragement for me. I do not have words to express my indebtedness to them for their prayers and moral boosting throughout my life. It is no exaggeration to say that I could not complete the PhD work without their generous help, boundless love, encouragement and support.

My husband (Rafeek) is the best motivation a woman can have. His strength and determination inspire me every day, and the completion of this Thesis would have been a long and windy road if not for his continuous encouragement. Rafi, Rifa Jabin (daughter), Ihan Swamith (son) have shown indefinable patience, love and support during the long and demanding years of hectic research activity. Their committed affection has worked as raindrops in the desert in many difficult situations in my research journey. Words cannot express my gratitude to them.

I am thankful to my sister (Shameeja) and brother in law (Kammunni). I know that I cannot thank them enough for all they have done for me in life.

I also would like to thank Brothers (Shafeek, Shanavaz), and sisters in law (Fathima Suhara, Rashida) for their affection and moral support. It is my pleasure to mention here the names of the new generation members of my family Diya Nazreen, Adul Aman, Isha Hanan, Sheza Nour for their everlasting love and support.

I thank my mother in law and in law relatives exclusively Hakkeem, Kunjumanikakka and Kunjakka for their love and helps extended towards me.

I thank UGC of India for the fellowship granted to me under Junior Research Fellowship.

I take this opportunity to convey my hearty thanks to all my teachers from my school days to post graduate level especially Saidutty sir, Basheer sir and Napheesa teacher.

I may not be able to complete the present work if my friends are not there to mentally support me from all sides. I will never forget the help and support that have done by Akbar and Deepthi. Vijayasree, Sudha, Divya, Vinu, Silija, Sowmya, Nikesh, Renuka chechi, Rajeena & Sreeja have helped me a lot to bring the work to a satisfactory completion.

I express my apology that I could not mention personally one by one.

Shaniba C. P.

CONTENTS

LIST OF TABLES

LIST OF FIGURES

Chapter 1

Metal Oxide / Hydroxide – Graphene Nanocomposite Materials

1.1 Introduction

Graphene is considered as one of the most promising two dimensional nanomaterials with a honeycomb network of sp^2 hybridized carbon atoms (Figure 1.1) which has been envisioned as the basic material for many nanocarbon forms like zero dimensional fullerenes and one dimensional carbon nanotubes [1-3]. A three dimensional graphite crystal contains many graphene sheets stacked together with an interplanar distance of 0.335 nm [4]. In 1962, it was Hanns Peter Bohem who coined the term 'graphene' by combining the words 'graphite' and suffix-'ene' for single layer of planar sp^2 hybridized carbon sheets [5-7].The free standing single-layer of graphene was first discovered in 2004 from graphite by means of a mechanical peeling strategy. The inventors of this material having many unique properties, Andre Geim and Konstantin Novoselov at the University of Manchester received the Nobel prize for Physics in 2010 [8-10].

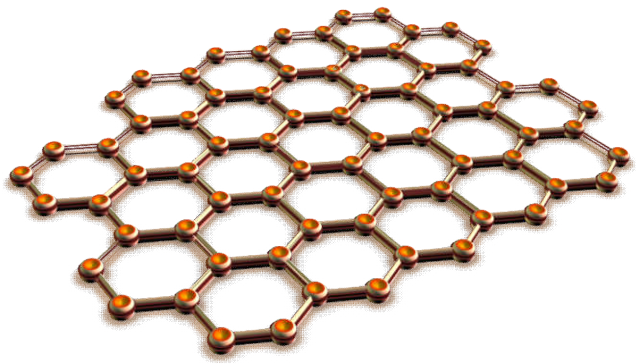

Figure 1.1: Schematic Diagram Illustrating Single Layer of Graphene with Two Dimensional Hexagonal Honey Comb Lattice

Because of the uniqueness in its structure, graphene is observed to possess many outstanding characteristics including high electron mobility at room temperature (250,000 cm^2/V) [11], electrical conductivity

of up to 6000S/cm^{-1} [12], quantum Hall effect and electron confinement effects [13, 14].In addition, graphene also possess many excellent mechanical and thermal properties such as large theoretical specific surface area (2630 m^2 g^{-1}) [15, 16], high Young's modulus (~ 1.0 TPa) [17] and the highest thermal conductivity of 5000 $Wm^{-1}K^{-1}$ [18]. It possess very unique optical properties as well. Graphene is highly transparent with absorption of < 2.3% towards visible light [19]. Thus, graphene can be considered as a promising candidate for a broad range of potential applications (shown in Figure 1.2.). Next-generation nanotechnology is anticipated to be dominated by many graphene based sophisticated products including electronic transistors [20], integrated circuits [21], transparent and flexible electronics [22], high performing nanocatalysts [23, 24], lithium ion batteries [25], solar cells [26], transparent conducting films [27], sensors [28, 29] as well as supercapacitors [30, 31].

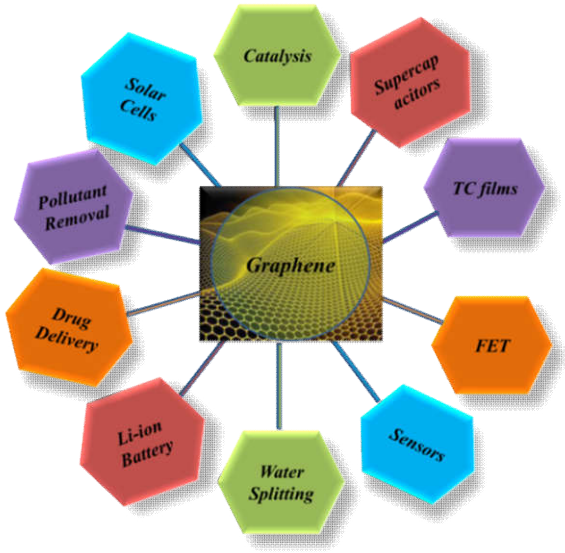

Figure 1.2: Schematic Diagram Showing Potential Applications of Graphene

The strong covalent C=C bonds between adjacent sp^2 carbon atoms make graphene a highly flexible and strongest material known [32-38]. In graphene, the carbon-carbon bond length is about 0.142 nm and in bulk graphite the graphene sheets are stacked with an inter-planar distance of 0.335 nm and the planes are bonded to each other by weak van der Waals forces [9]. A single two-dimensional hexagonal sheet of carbon atoms is termed as single-layer graphene (SLG). Bi-layer and few-layer graphene (BLG and FLG) having 2 and 3 to 10 layers of such two-dimensional carbon sheets, respectively also exhibit some properties different from bulk graphite. If more than 10 such layers are present, properties are more or less same as that of bulk graphite and they are of less scientific interest [32-38]. One of the best characterization technique for graphene is Transmission Electron Microscopy (TEM) in which graphene monolayers are seen as transparent films on the supporting substrate, whereas HRTEM images clearly show the hexagonal lattice. However, TEM is not considered as an authoritative tool to discriminate between graphene monolayers and stacked nanosheets with two or more layers. Atomic Force Microscopy (AFM) and Raman spectroscopy are the widely accepted prevailing tools which provide an insight about the thickness of the material and number of layers [33, 38].

1.2 Preparation Methods of Graphene

With the tremendous growth in the graphene research in recent years, graphene has captured the position of the leading material capable of being the basic part of the next revolutionary technologies.

As a substitute of many of the currently used materials, it is anticipated to create a new market and ultimately leading to scientific and technological revolution. However, for the commercialization of graphene, its scalable and cost-effective production is absolutely necessary. If graphene price does not come down, its commercial and extensive use could be hindered [39]. At present there are different methods for the preparation of graphene which can be evaluated on the bases of different required functions. Some of them are on the basis of purity (quality) of graphene and also based on the size of the sheets [40]. Another aspects to consider are the scalability of the process, how laborious it is and the controllability of the methods. Graphene production methods can be broadly categorized in to two types. The detachment of graphene from an already exciting graphite crystal, the so-called exfoliation strategies which is the top-down approach, and the second one is directly growing the graphene layer on a substrate surface by various methods which can be termed as the bottom-up approach [40].

1.2.1 Exfoliation Strategies

It is possible to yield good quality graphene from highly pure graphite if the weak van-der Waals force between graphene sheets can be broken. Mechanical as well as chemical energies can be used to detach the graphene sheets. These are the easiest methods and highly pure product can be obtained in some of them. In the scotch tape exfoliation method, graphene is detached from graphite crystal using an adhesive tape [41]. Depending upon the wafer used the sizes range

from nanometers to several tens of micrometers for single and few layer graphene. The quality of the prepared graphene is high with almost no defects [40]. However, it is not a scalable method since it is laborious to get larger amounts of graphene by this strategy [42].

Graphite oxide route of exfoliation is one of the most commonly used methods for the preparation of graphene. This method involves the intercalation of graphite with strong oxidizing agents such as sulphuric acid, nitric acid and potassium permanganate and subsequent functionalization of the graphene framework with oxygen moieties. It is then followed by expansion of graphite layers via sonication. During the process of sonication, different functional groups like epoxide or hydroxyl groups present on the framework make the sheets hydrophilic and water molecules easily enter in to the interlayer spacing and easy exfoliation is resulted. Thus, an aqueous dispersion of graphene oxide is obtained. The layers become negatively charged and the recombination of graphite layers is inhibited by the electrostatic repulsion. The reduction of the graphene oxide to graphene is usually accomplished by either thermal or a chemical approach to get graphene [43, 44]. This method is considered as one of the high-yield (>50%) production methods of graphene. However, it is very difficult to dispose of all the oxygen moieties which make a compromise on the graphene quality [40, 44, 45].

There are several reports in which graphene was prepared by liquid phase exfoliation using various solvent systems [46-49]. Because of the possibilities of scalable production and low cost, liquid-phase

exfoliation has been considered as one of the most feasible approach for industrial production of good quality graphene. Liquid phase exfoliation of natural graphite, avoiding the drastic and uncontrollable oxidation of graphene is easy to implement even in large scale units. It involves ultrasonication of natural graphite powders in different organic solvents like N-methyl-2-pyrrolidone (NMP), N'N-dimethylformamide (DMF), γ-butyrolactone (GBL), etc. for several hours sometimes applying a voltage. However, poor graphene yield, especially compared to the graphene oxide route, is the main disadvantage of this process. Among various solvents, NMP gives the highest yield of graphene probably due to its surface energy close to that of graphite which makes the energy barrier due to the interacting forces between graphene layers comes down. In order to dispose of the thicker flakes, the dispersion has to be centrifuged. Graphene prepared by this method was revealed to be of superior quality and have low concentration of defects and less oxygen functional groups compared to the final product obtained in the graphene oxide route. The primary reason for the very low yield is the fact that solvent molecules are incapable of going into interlayer spaces and only the surface layers of graphite are peeled off during the sonication process [46-49].

1.2.2 Growth on Surfaces

To grow graphene directly on a surface by various means is a totally different strategy from the exfoliation methods discussed so far. One major difference lies in the fact that the size of the acquired layers does not depend on the initial precursor taken. This growth can be

achieved mainly by two different ways. One of them utilizes the carbon already exist in the substrate and in the second one carbon is added from a source material, usually hydrocarbons, by chemical vapour deposition.

Epitaxial growth means the oriental growth of a crystalline material over the surface layer of another crystalline substrate, where there is interaction between the two. One of such techniques of graphene preparation is the epitaxial growth of graphene on SiC crystal. It is a very promising technique to synthesize high quality graphene monolayers of uniform wafer size. The technique involves the annealing of SiC crystal at high temperature, about 1300 ^{o}C, under vacuum. The dimensions of graphene formed depend on the SiC substrate and the number of layers depends on the decomposition temperature. Generally, single or bi-layer graphene grows on the Si face of the crystal, whereas few layer graphene forms on the carbon face. The nature of the product obtained depends on the various experimental parameters like temperature, pressure or heating rate. If the temperature and pressure are too high, then instead of graphene sheets nanotubes will be formed. By this process epitaxial graphene with different dimensions are formed depending upon the size of the wafer. Epitaxial graphene growth on SiC technique has been advanced now so that by the number of graphene layers grown can be carefully controlled as well as can be patterned using standard microelectronics methods. Hass et al. has presented a comprehensive review on this topic, covering issues of epitaxial multilayer graphene grown on different faces of SiC, their morphology and electronic properties [50]. In

the method of graphene preparation by ultrahigh vacuum annealing of the SiC surface, the sublimation rate of silica is higher than that of carbon, excess carbon is left behind on the surface, which rearranges to form graphene sheets. The obtained graphene possess high-quality and large area. SiC is well suited to high-frequency semiconductor devices itself. Thus the graphene prepared through this method can be used for high-frequency graphene based transistors. It's an expensive process and is not compatible with many electronics production technologies, which somewhat limit its development. However, due to their capability at high voltage and temperature, SiC devices are being developed for consumer applications [40, 50-54].

Chemical vapor deposition (CVD) is a well-known process and is considered as an alternative method for mechanical exfoliation. It is the frequently used method for large scale production of high quality mono or few layer graphene sheets. In CVD method, graphene is grown directly on a transition metal substrate using hydrocarbon gases as carbon source at a deposition temperature of about 1000^{o}C. Ni and Cu films are generally used as the substrate with methane as the precursor gas. The methane decomposes on the surface in order to grow a thin film of carbon, whereas the hydrogen evaporates. The carbon diffuses into the Ni substrate. When the Ni is cooling down in an argon atmosphere, the solubility of carbon on the Ni substrate decreases and the carbon precipitates to form mono to multilayer graphene sheets on the surface. The average number of layers and the shape of graphene depend on the Ni thickness and can be controlled by patterning of the Ni layer [40, 55-65]. First report on few layer graphene

synthesized by CVD, was found in 2006. In their work camphor was first evaporated at 180 ºC and then pyrolyzed, in another chamber of the CVD furnace at 700-800 ºC using argon as carrier gas. Graphene, thus obtained, was found to have multiple folds as evident from the HRTEM images and estimated to have approximately 35 layers of graphene sheets [66]. Substrate free FLG was synthesized by Wang et al. using MgO supported Co catalysts [67]. Ruoff et al. reported single layer graphene with less than 5% of few layer graphene when copper is used instead of Ni as growing substrate [60]. Bae and coworkers reported the production of 30 inch long graphene films using the CVD approach [57].

One of the major advantages of the epitaxial and CVD growth techniques is their high compatibility with the current complementary metal-oxide-semiconductor (CMOS) technology. Two major disadvantages of the CVD technique are the difficulty to control the film thickness and the easy formation of secondary crystals. Moreover, expensive substrate is needed for graphene growth which limits its application for large scale production. However, for mass production of high quality graphene with less defects, the CVD approach has become an important method [40, 55-65].

Unzipping of carbon nanotubes to form graphene nanoribbons have been reported by a number of research groups. Kosynkin et al. report the preparation of regular size graphene sheet through "chemical method" by the action of concentrated sulphuric acid followed by treatment with $KMnO_4$ to unzip MWCNT [68]. In another report by Jiao et al., argon plasma etching of nanotube is done resulting in the

formation of graphene nanoribbons partly embedded in a polymer film [69]. Cano- Marquez reported graphene nanoribbon production by treating multi-walled carbon nanotubes by employing lithium and ammonia [70, 71].

1.3 Graphite oxide, Graphene Oxide (GO) and Reduced Graphene Oxide (rGO)

Graphite oxide consists of graphene sheets functionalized with different oxygen moieties mainly epoxide and hydroxyl groups [72]. It is produced by one of the drastic oxidative treatment of graphite developed by Brodie, Hummers or Staudenmeir or by methods with slight modifications from these strategies [52, 73, 74]. Unlike graphite, Graphite oxide is an electrically insulating material with wide band gap and is thermally less stable because of the presence of the oxygen functional groups [72]. Chemical reduction using hydrazine hydrate can be used to restore its electrical conductivity and thermal stability to a large extend [75]. The structure and properties of graphite oxide can vary based on the synthesis method employed and the level of oxidation present. Large extent of disorder as well as irregular packing of layers is present in graphite oxide which makes the study of its structure rather difficult. Since graphite oxide (GO) is a hydrophilic derivative of graphite, the solvent water molecules can easily enter in to their layers and cause exfoliation with mild sonication. Exfoliated graphite oxide is called graphene oxide, which is another two dimensional material with many interesting properties. Graphene oxide is also electrically insulating in nature mainly due to their disrupted sp^2

bonding network [75-79]. Electrical conductivity can be recovered by restoring the л-electron network by means of a suitable reduction strategy which can be considered as one of the most important reactions of graphene oxide and the product formed is known as reduced graphene oxide (rGO) since some of the edge functional groups may retain in the graphene sheets even after the reduction process. Thus, the chemical conversion of graphite to graphite oxide followed by exfoliation by sonication is the most popular method of graphene production in large scale suitable for many applications. Even though this route is of low cost and of high-yield, the product quality will be comparatively inferior compared to other methods. However, for many specific applications of graphene, for example, as catalyst support, the rGO is found to be well suited [40,43-45, 75-79].

1.4 Nanocomposites

In a composite, if at least one of the components shows dimensions in the nanometre range (1 nm = 10^{-9}m) it can be called a nanocomposite. According to Kamigaito, (reported in 1994) "A nanocomposite is a multiphase solid material where one of the phases has one, two or three dimensions of less than 100 nanometers (nm), or structures having nano-scale repeat distances between the different phases that make up the material" [80]. The properties of the nanocomposite like mechanical, electrical, thermal, optical, electrochemical or catalytic properties may differ markedly from that of the component materials [81,82].The properties of nanocomposite materials depend not only on the properties of their individual

components but also on their morphology and interfacial characteristics. Nanocomposites are found in nature. For example, the abalone shell and bone can be considered as made up of nanocomposites [80-84].

1.4.1 Graphene Based Nanocomposites

There is a tremendous increase in the research related to graphene and graphene based nanocomposite materials after the discovery of large-scale production methods of graphene, graphene oxide, reduced graphene oxide and other forms of exfoliated graphite materials. Graphene based nanocomposites find potential applications in diverse fields of research such as electronics, sensing, catalysis and energy related areas.

Particularly, the catalytic, magnetic and optoelectronic properties of graphene based nanocomposites have attracted increasing attention in recent years. Because of the unique sp^2 hybridization of carbon bonds in graphene which results in the delocalization of electrons, excellent electronic conduction is exhibited by graphene. With the incorporation of various functional materials, such as metals, metal oxide NPs and conducting polymers the electronic conduction as well as the electronic structure of graphene can be further modified. Thus, novel advanced functional materials with enhanced electrical and electronic properties can be produced in this manner. In nanocomposites of uniform composition, the synergistic effect between graphene and nanoparticles enable graphene based nanocomposites suitable for various sophisticated applications in many fields like

electronics, solar energy harvesting, chemical and biological sensors, electrochemical, energy storage and conversion and so on. Apart from improving the properties of graphene, the other components prevent the aggregation of individual graphene sheets, blocking the van der Waals interactions between the graphene layers. More efforts and new straight forward and economically viable strategies to synthesize graphene-based nanocomposites are essential in the current scenario [85-93].

1.5 Heterogeneous Catalysis

Heterogeneous catalysts play a crucial role in various chemical transformations today, especially in various fields such as energy related systems, environmental protection and organic synthesis [94]. However, most of the conventional heterogeneous catalytic systems contain noble metals, metal oxides or sometimes enzymes as their active ingredient. This leads to their high cost and sometimes serious environmental pollution issues when they are commercially employed. In recent years, the conventional catalysts have been increasingly replaced by carbon-based materials as catalysts or as support matrix for improving the catalytic performance of other active components, as part of the efforts to overcome the issues caused by the conventional catalytic systems [95].

1.5.1 Role of Carbon Nanostructures in Catalysis

The performance of a heterogeneous catalyst is mainly decided by the nature, concentration and accessibility of the active sites that are

capable of chemisorbing the reactants and form surface intermediates. Carbon nanomaterials exhibit several unique properties which are beneficial in improving the overall catalytic performance when they are used as supports in heterogeneous catalytic systems [95]. Some of the reasons which favor the use of carbon based materials are the following.

Because the surfaces of graphene like carbon nanomaterials are relatively inert, the occurrence of unwanted reactions will not occur on these surfaces or will not be catalyzed by the support surface. In addition, there won't be any reaction of the support with the active phase.Some of the carbon materials are relatively cheap in comparison to other conventional catalytic supports. The expensive active components can be recovered in a straight forward manner by simple calcinations in the presence of oxygen. In non-oxidizing atmospheres, the carbon materials are stable at high temperatures. Although graphene usually have a hydrophobic nature, graphene oxide has hydrophilicity [95].

In graphitic forms of carbon such as fullerenes, carbon nanotubes, carbon nano onions etc. have been generally considered as materials which possess an intriguing potential for catalytic applications [96-102]. Earlier carbon nanostructure based catalytic studies were focused on simple redox reactions. Now the area has expanded enormously and literature reports demonstrate that catalysts with carbon forms are capable of catalyzing reactions that involve sophisticated transformations of complex functional groups including

C–C or carbon–heteroatom bond formations. The reaction involving hydrogenation of nitrobenzene to produce aniline at ambient temperature and under UV irradiation has been reported to be catalyzed by C_{60} [103]. Similarly, for several reactions such as methane decomposition [104], oxidation of p-toluidine [105], and conversion of aniline to azobenzene [106] carbon nanotube based heterogeneous catalytic systems have been employed.

The major advantages of graphene as an important component in catalytic systems are its huge specific surface area, superior thermal conductivity and electron mobility [96]. In most of the cases, graphene itself exhibit weak catalytic activity. However carbo-catalysis is an emerging area today. Different strategies have been employed by researchers to improve catalytic performance of graphene including the doping with hetero-atoms such as nitrogen, boron and sulphur [107-109]. Another strategies are chemical modifications of graphene and self-assembly. Thus, there are several recent reports in which graphene and its derivatives have been successfully utilized as catalysts for various electrochemical, photochemical and other chemical reactions [85-93].

1.5.1.1 Holey Graphene Framework (HGF)

Holey Graphene Framework (HGF) is essentially graphene sheets with holes on its two dimensional lattice ranging from a few to tens of nanometers in average diameter [110]. It should be noted that there is a possibility that graphene sheets prepared from any preparation method may contain intrinsic defects. For example, the most common types of defects on graphene surface are Stone–Wales

(pentagon–heptagon pairs) or vacancy sites, which are typically nanometers in size [111-113]. Recently, there are several reports on novel types of graphene structures with many desired properties that are characterized by large holes on the carbon network [110-137]. Compared to the conventional defects that are difficult to observe using high-resolution microscopic techniques, these pore openings can be easily identified by microscopic techniques such as TEM because of the much larger size of the holes (ranging from a few to hundreds of nanometers) [112]. The HGF structures can be obtained from lithographic methods as well, which are also called "graphene nanomeshes". Such HGF, usually possess spherical hole geometry with uniform sizes [110].

The perforated structure of HGF is advantageous in many of the applications [110-145]. For example when holey graphene sheets are used as fillers for polymeric composites, the results show that they are better reinforcing fillers compared to the starting graphene sheets [111]. Further, making holes in graphene is found to a method for opening its band gap and to increase its specific surface area holey graphene also finds its application in catalysis, sensing, electrochemical energy storage and so on [114-145]. Therefore in recent years there is an increased interest in the development of HGF and its applications. HGF is shown to have excellent absorption performances for oils, solvents, and dyes when it is employed as a water cleaning agent. The saturated holey graphene after its use as a sorbent can be readily cleaned by means of burning in air and can be reused [146].

1.5.1.2 Nitrogen Doped Holey Graphene (NHG)

For improving the catalytic activity of holey graphene framework, there are several reports in which various structural modifications are introduced, such as doping of heteroatoms like N or B [147-157]. Among them, the substitution of nitrogen (N) atoms appears to be the most popular one [147-150]. There are a few reports in which nitrogen doped holey graphene (NHG) are used as multifunctional metal-free electrochemical catalysts for ORR and HER [147-150]. The holes on the surface structure of individual graphene sheets produce more exposed active edge sites and nitrogen doping is capable of further improving the catalytic performance [147-157].

1.6 Heterogeneous Photocatalysis

Heterogeneous photocatalysis is essentially a catalytic process in which electron–hole pairs are generated on the surface of certain semiconductors illuminated by light of suitable energy matching with its band gap. There is a huge interest in this area of research in recent years [158]. Examples of various heterogeneous photocatalytic reactions in which large quantity of research work is going on recent years are,

1) Hydrogen production via photocatalytic water splitting. Providing clean H_2 fuel by means of solar energy harvesting is the ultimate target of water splitting experiments [159-163].

2) Photocatalytic conversion of carbon dioxide and water in to solar hydrocarbon fuels mimicking photosynthesis. The

semiconductor catalyst absorbs solar energy and converts chemicals in to other forms [164-168].

3) The photocatalytic remediation of contaminants in waste water. For various contaminants like hydrocarbons, alcohols, carboxylic acids, phenols, organic dyes, surfactants, pesticides and antibiotics this technology can be successfully employed [169-173]. For the reductive deposition of heavy metals from aqueous solution to surfaces as well (e.g., Pt^{4+}, Au^{3+}, Rh^{3+}, Cr (VI)) this technology can be effectively utilized [174-178].

1.6.1 Electronic Structure of Semiconductor Photocatalysts

The electronic energy structure of a semiconductor can be classified in to three distinguished regimes, i.e., the conduction band (CB), the valence band (VB) and the forbidden band. For an undoped semiconductor, there won't be any allowed energy states in the forbidden gap. Energy has to be applied to promote electron from valence band to conduction band. The energy required for this purpose depends on the band gap which is different for different semiconductors. Thus, the energy of the photon required for this electronic excitation varies with the band structure of the semiconductor used. This light absorption by semiconducting materials will lead to the formation of electron-hole pairs responsible for the photocatalytic redox reactions [160].

On irradiation, the electrons present in the valence band (VB) of the semiconductor photocatalysts are excited to the conduction band

(CB), while the holes are left behind in the valence band thus, creating the electron-hole pairs. The band gap must be equal to the wavelength of the light in order to achieve better absorption of light by the photocatalyst. The holes are capable of oxidizing adsorbed H_2O or HO^- to reactive hydroxyl radicals ($HO^{\bullet}$) and this can initiate the degradation or the disinfection process. The electrons in the conduction band produce superoxide radical anions that can also degrade the pollutants [160].

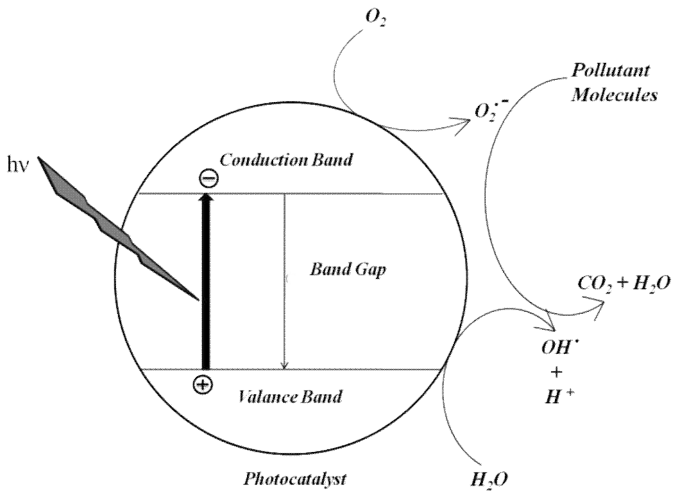

Figure 1.3: Representation of Pollutant Degradation on a Semiconductor Photocatalyst

As mentioned before, when a semiconductor absorbs a photon with energy greater than the bandgap, a valence band electron is excited to the conduction band, generating a photoexcited electron/hole pair. These negative and positive charges induce redox reactions after migrating to the surfaces of photocatalyst particles, as summarized in the following equations:

$$2H^+ + 2e^- \longrightarrow H_2$$

$$H_2O + 2h^+ \longrightarrow \tfrac{1}{2}\, O_2 + 2H^+$$

$$H_2O + 2(e^- + h^+) \longrightarrow H_2 + \tfrac{1}{2}\, O_2$$

The first prerequisite for water splitting is related to thermodynamics; the conduction and valence band edges should include the redox potentials for water splitting (H^+/H_2 and O_2/H_2O). The energy difference between these two redox potentials is 1.23 eV in the case of a four-electron transfer process, corresponding to the energy of a photon with a wavelength of approximately 1000 nm [160].

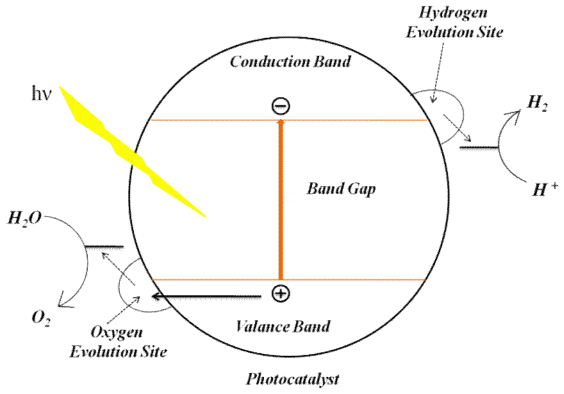

Figure 1.4: Representation of Photocatalytic Water Splitting on a Semiconductor Photocatalyst

1.6.1.1 Zinc Oxide

From the 1960s onwards, ZnO has a special place in the material science research field. ZnO shows mainly three different types of crystalline structures, i.e, wurtzite, zinc-blende and rarely noticed rock- salt structure [179]. The wurtzite structure is having a hexagonal

symmetry and it possesses lattice spacing a= 0.325nm and c=0.521nm. The ratio between c and a is approximately 1.6 and it is very close to the ideal hexagonal cell value c/a =1.633. In the structure of ZnO, each tetrahedral Zn atom is surrounded by four oxygen atoms and vice-versa. This tetrahedral coordination is typical of sp^3 covalent bonding. But these materials also possess a substantial ionic character. ZnO is a II-VI compound semiconductor whose ionicity exists in the borderline between covalent and ionic semiconductor. The wurtzite structure is thermodynamically stable at ambient conditions. The zinc-blende structure of ZnO can be stabilized only by growth on cubic substrates. At relatively high pressures, the rocksalt NaCl structure can be obtained [179].

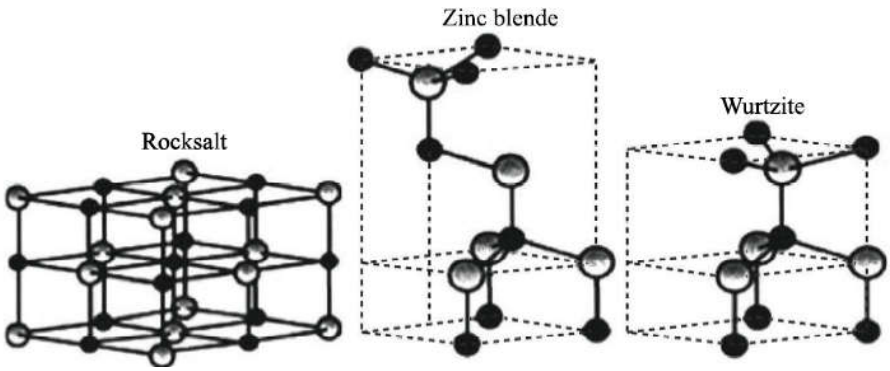

Figure 1.5: Different Crystalline Forms of ZnO

The factors that bring ZnO in to the class of multifunctional, smart materials can be listed as its unique optical, physical and chemical properties such as high chemical stability, high electrochemical coupling coefficient, and broad range of radiation absorption, electric conduction, chemical sensing and high

photostability. Zinc oxide has triggered worldwide research interest mainly because of its applications in the field of sensors, transducers and catalysts [180-191]. In addition, ZnO is characterized by a direct broad energy band gap of 3.37 eV, a high binding energy value of 60 MeV and high thermal and mechanical stability at room temperature. These characteristics enable ZnO well suited material for various fields such as electronics, optoelectronics and laser technology [192--200]. The lack of a centre of symmetry in wurtzite combined with large electromechanical coupling results a strong piezo- and pyro-electric property for ZnO [194]. It can be used as a key material in the ceramics industry due to its hardness and rigidity. ZnO finds its use in the areas of biomedicine and pro-ecological systems because of its low toxicity, biocompatibility and biodegradability [201-203].

Nano forms of Zinc oxides fall in three different categories such as one- (1D), two- (2D), and three-dimensional (3D) structures. A collection of ZnO nanostructures with different growth morphology one-dimensional structured ZnO being the largest group, containing nanorods [204-206], -needles [207], helixes, -springs and -rings [208], -ribbons [209], -tubes [210-212], –belts [213], -wires [214-216] combs [217] and so on. 2D structures of zinc oxide such as nanoplate/nanosheet and nanopellets also have been reported [218,219]. Three dimensional ZnO structures include flower, dandelion, snowflakes, coniferous urchin-like morphology materials [220–222]. ZnO is generally transparent in nature and can be made highly conductive by doping. In addition, it is also a battery active material which attains an energy density of 650A/g and

has a good electrical conductivity (up to 230 S/cm), which is larger than those of other metal oxide materials.

A variety of methods are available for the production of ZnO such as hydrothermal synthesis, vapour deposition methods, the sol-gel process, precipitation from aqueous solutions, precipitation from micro-emulsions and by means of mechano-chemical processes. From each production processes, it is possible to obtain ZnO forms differing in shape, size and spatial structure. Two major production routes for ZnO are hydrothermal method and microwave preparation [223].

1.6.1.1.1 Hydrothermal and Microwave Methods for ZnO Preparation

The hydrothermal method is a simple and environmental friendly technique in which no need of organic solvents or additional processing of the product such as grinding, calcination, etc. are required. The hydrothermal synthesis is carried out in a pressure vessel (an autoclave) in which the precursor materials and the solvent are heated to a temperature of 100–300 °C and is left for several days. After the heating and cooling process, crystallites nucleated initially grows bigger. This synthesis strategy has many advantages. It can be carried out at low temperatures. Depending on the composition of the starting mixture, temperature and pressure, diverse shapes and dimensions of the resulting crystals can be obtained. The product has high degree of crystallinity and purity [224,225]. When pH of the solution increases, crystallinity and size of the particles increases, which

reduces the efficiency of the process. The size of the particles increases with increase in time, temperature and surfactant concentration [224].

A number of reports [226-228] reveal that the use of microwave reactors possess significant benefits. In microwave reactor, it is possible to heat the solutions by avoiding loss of energy on heating the entire vessel. When microwaves are used many chemical reactions proceed with greater speed and give high yield compared to the traditional methods. By the use of the microwave reactor it is possible to shorten the reaction time several fold, and the product obtained will be in its purest form. The morphology of the product obtained and the aggregation possibilities depend strongly on the precursor used for the ZnO preparation. Also, the morphology and size of the nanoparticles/nanowires of ZnO is decided by the oxidizing agents used and the coordinating abilities of the solvents. The presence of trace quantities of water catalyze the reaction which affect the size of the ZnO nanocrystallites formed. Depending on the reaction conditions, the zinc oxide can be produced with diameters in the range 24–185 nm [224].

1.6.1.2 Titania

TiO_2 is considered as a large band gap semiconductor, with band gaps of 3.2, 3.02, and 2.96 eV for the anatase, rutile and brookite phases, respectively. The valence band of TiO_2 is composed of the 2p orbitals of oxygen hybridized with the 3d orbitals of titanium, while the conduction band is solely by the 3d orbitals of titanium. As described before, when TiO_2 is exposed to near-UV light, electrons in

the valence band will get excited to the conduction band leaving behind holes (h^+). The excited electrons (e^-) in the conduction band are now in a purely 3d state and because of dissimilar parity; the transition probability of e^- back to the valence band is less, which makes a reduction in the probability of e^-/h^+ recombination, making the electron and holes available for redox reactions on the surfaces. Anatase TiO_2 is considered to be the most active photocatalytic component based on charge carrier dynamics, chemical properties and the activity for the photocatalytic degradation of organic compounds. The anatase phase has an inherent surface band bending that forms spontaneously in a deeper region with a steeper potential compared to the rutile phase. Thus, in anatase the surface hole trapping dominates because of the spatial charge separation which is achieved by the transfer of photogenerated holes towards the surface of the particle *via* the strong upward band bending. However, in the rutile phase, the bulk recombination of electrons and holes is more, so only holes very close to the surface are trapped and transferred to the surface making it a poor photocatalyst compared to anatase [229-234].

1.6.1.3 Nickel Hydroxide

Nickel hydroxide has been used as an electrode material for battery technologies for about 65 years. It is one of the components formed from the surface layers of nickel metal and nickel-based alloys either electrochemically or by the corrosion process. In 1966 Bode et al. first recognized the two known pseudo polymorphs of $Ni(OH)_2$, designated as α- and β-$Ni(OH)_2$[235,236]. The β-$Ni(OH)_2$ has a hexagonal

closest-packed structure of Ni^{2+} and OH^- ions, without other intercalated ion and is iso-structural with brucite, $Mg(OH)_2$ occurs naturally as the mineral theophrastite [237,238]. The angle between a and b axes (γ) in β-$Ni(OH)_2$ is 120. The α structure consists of $Ni(OH)_2$ layers with intercalated anions or water molecules occupying the space between layers. The degree of hydration varies within the range $0.41 \leq x \leq 0.7$. Although the material is basically hydrated, it is denoted α-$Ni(OH)_2$ by omitting the water molecules [239,240].

Today, nickel-based batteries are universal, including nickel–cadmium (Ni-Cd) and nickel metal hydride (Ni-MH) technologies [241,242]. Mc Breen in 2011 reported the application of nickel hydroxides in modern battery technologies[242]. Decades of work has determined a much more complete description of the nickel hydroxides than the simple two-phase model. There have been numerous advances in the preparation and characterization of nickel hydroxide materials [235]. There are now numerous reported methods to synthesize hydroxides of nickel. As a result, finding a suitable method to prepare nickel hydroxide with appropriate properties can be a time-consuming and overwhelming task. Desired properties may include the phase (α or β), crystallinity (stacking fault disorder, purity, etc.), product morphology (porosity, nanostructure, etc.) and general form (bulk powder, thin film on a metallic substrate, etc.). In common, by chemical precipitation or by impregnation-precipitation, α-$Ni(OH)_2$ can be prepared in bulk quantities. By electrochemical precipitation it also can be deposited as a thin layer on a conductive substrate. α or β structured materials can be prepared by sol-gel method, by means of a bulk material or

deposited on a substrate by spin- or dip-coating. By the chemical ageing of α-$Ni(OH)_2$, high-purity β-$Ni(OH)_2$ material can be produced. By hydrothermal or solvothermal synthesis, bulk quantities of micro- or nanostructured α- or β-$Ni(OH)_2$ can be prepared. Nickel hydroxides are common components of corrosion deposits and electrochemically formed surface layers on nickel metal and nickel-based alloys [235].

In hydrothermal (aqueous) and solvothermal (non-aqueous) synthesis the precursor materials and the solvent are placed in a pressure vessel and then the reaction mixture is heated. Typical reaction temperatures for $Ni(OH)_2$ synthesis are 150–200 °C, above the boiling point of water. Because the vessel has a fixed volume, as the solution is heated, the pressure increases. Therefore, the boiling point increases and the solution remain liquid at such high temperatures that the precursors fully dissolve [(243)]. The scale of this method is limited by the size of the pressure vessel. In the laboratory, this is usually in the range of hundreds of millilitres to a few litres. For industrial applications, larger pressure vessels on the order of hundreds of litres, are commonly used. Therefore, hydrothermal and solvothermal methods may be used for large-scale production of $Ni(OH)_2$ as well [235].

In general, β-$Ni(OH)_2$ tends to form at the high temperatures used in hydrothermal synthesis. However, it is possible to produce α-$Ni(OH)_2$ materials by introducing an intercalation agent into the reaction mixture [244], by using a non-aqueous solution [245] by limiting the reaction time or by using a low reaction temperature [246] . For example, the addition of urea to a reaction mixture results in the

formation of NH_3-intercalated α-$Ni(OH)_2$[244]. Hydrothermal and solvothermal syntheses may be used to produce $Ni(OH)_2$ nanoscale materials with unique morphologies. It can be prepared micrometre-scale 'nanoflower' aggregates composed of nanosheets [245, 247, 248]. The morphology is maintained when the nanoflowers are calcined, to form NiO [248], or chemically aged, to form crystalline β-$Ni(OH)_2$ [247]. However, prolonged ageing can flatten the nanoflowers. It is possible to produce 'nanoribbons' or 'nanobelts'.

Nowadays, Nickel hydroxide have a variety of useful applications in different fields of chemistry, physics and engineering which include photocatalysis[249-251], electrocatalysis and electrosynthesis[252-254], supercapacitors[247,255-259], electrochromic devices [260-262], electrochemical sensors [248, 263–265], etc.

1.7 Objectives

The overall objective of this research is the development of novel and efficient graphene based catalytic systems by adapting simple strategies like hydrothermal method, their characterization using various spectroscopic and microscopic techniques and their application in various environment related issues. Our main focus is on the removal of persistent contaminants like chlorinated aromatic hydrocarbons from the environment, water purification by sun light assisted photocatalytic antibiotic degradation for the prevention of the growth of antibiotic resistant bacteria and photocatalytic production of 'green fuel', hydrogen via water splitting.

References

1. I. V. Lebedeva, A. A. Knizhnik, A. M. Popov and B. V. Potapkin, *J. Phys. Chem. C.,* 2012, **116**, 6572-6584.

2. Y. Kumar, A. Ahmed and S. Erande, *IOSRJECE.,* 2012, **2**, 41-44.

3. U. K. Sur, *Int. j. electrochem.,* 2012, **237689** (1-12). Doi:10. 1155/2012/237689.

4. A. Fasolino, J. H. Los and M. I. Katsnelson, *Nat. Mater*., 2007, **6**, 858-861.

5. H. P. Boehm and Angew. *Chem. Int. Ed.,* 2010, **49**, 9332-9335.

6. H. P. Boehm, R. Setton, and E. Stumpp, *Carbon.,* 1986, **24**, 241-245.

7. H. P. Boehm, R. Setton, and E. Stumpp, *Pure &Appl. Chem.,* 1994, **66**, 1893-1901.

8. K. S. Novoselov, A. K. Geim, S. V. Morozov, D. Jiang, Y. Zhang, S. V. Dubonos, I. V. Grigorieva, and A. A. Firsov, *Science.,* 2004, **306**, 666-669.

9. K. S. Novoselov, D. Jiang, F. Schedin, T. J. Booth, V. V. Khotkevich, S. V. Morozov and A. K. Geim, *Proc. Natl. Acad. Sci. U. S. A.,* 2005, **102**, 10451-10453.

10. M. S. Dresselhaus and P. T. Araujo, *ACS Nano.,* 2010, **4**, 6297-6302.

11. M. Ortila, C. Faugeras, P. Plochocka, P. Neugebauer, G. Martinez, D. K. Maude, A. L. Barra, M. Sprinkle, C. Berger, W. A. de Heer and M. Potemski, *Phys. Rev. Lett*., 2008, **101**, 26-31.

12. X. Du, I. Skachko, A. Barker and E. Y. Andrei, *Nat. Nanotechnol.,* 2008, **3**, 491-495.

13. Y. Zhang, Y. W. Tan, H. L. Stormer, and P. Kim, *Nature.,* 2005, **438**, 201-204.

14. K. S. Novoselov, Z. Jiang, Y. Zhang, S. V. Morozov, H. L. Stormer, U. Zeitler, J. C. Maan, G. S. Boebinger, P. Kim and A. K. Geim, *Science.,* 2007, **315**, 1379-1379.

15. Y. Zhu, S. Murali, W. Cai, X. Li, J. W. Suk and J. R. Potts, *Adv. Mater*., 2010, **22**, 3906-3924.

16. C. M. Weber, D. M. Eisele, J. P. Rabe, Y. Liang, X. Feng, L. Zhi, K. Mullen, J. L. Lyon, R. Williams, D. A. V. Bout and K. J. Stevenson, *Small*, 2011, **6**, 184-189.

17. C. Lee, X. Wei, J. W. Kysar, J. Hone, *Science.,* 2008, **321**, 385-388.

18. A. Balandin, S. Ghosh, W. Bao, I. Calizo, D. Teweldebrhan, F. Miao and C. N. Lau, *Nano Lett*., 2008, **8**, 902-907.

19. S. Pang, Y. Hernandez, X. Feng and K. Mullen, *Adv. Mater*., 2011, **23**, 2779-2795.

20. F. schwierz, *Nat. Nanotechnol.,* 2010, **5**, 487-496.

21. S. J. Han, A. V. Garcia, S. Oida, K. A. Jenkins and W. Haensch, *Nat. Commun.,* 2014, **5**, 1-6.

22. G. Eda, G. Fanchini and M. Chhowalla, *Nat. Nanotechnol.,* 2008, **3**, 270-274.

23. D. Deng, K. S. Novoselov, Q. Fu, N. Zheng, Z. Tian and X. Bao, *Nat. Nanotechnol.,* 2016, **11**, 218-230.

24. X. Fan, G. Zhang and F. Zhang, *Chem. Soc. Rev.,* 2015, **44**, 3023-3035.

25. B. Qiu, M. Xing and J. Zhang, *J. Am. Chem. Soc.,* 2014, **136**, 5852-5855.

26. H. Ding, S. Zhang, P. C. Juan, T. Y. Liu, Z. F. Du and D. L. Zhao, *RSC Adv.,* 2016, 6, 41092-41102.

27. S. J. An, Y. Zhu, S. H. Lee, M. D. Stoller, T. Emilsson, S. Park, A. Velamakanni, J. Anand R. S. Ruoff, *J. Phys. Chem. Lett.,* 2010, **1**, 1259-1263.

28. X. Dong, W. Huang and P. Chen, *Nanoscale Res Lett*., 2011, **6**, 60-65.

29. K. -L. Wu, Y. –M. Cai, B. –B. Jiang, W. –C. Cheong, X. –W. Wei, W. Wang and N. Yu, *RSC Adv.,* 2017, **7**, 21128-21135.

30. Z. Sun and X. Lu, *Ind. Eng. Chem. Res.,* 2012, **51**, 9973-9979.

31. L. Ma, M. Zheng, S. Liu, Q. Li, Y. You, F. Wang, L. Mad and W. Shena, *Chem. Commun.,* 2016, **52**, 13373-13376.

32. M. J. Allen, V. C. Tung and R. B. Kaner, *Chem. Rev.,* 2010, **110**, 132–145.

33. C. N. R. Rao, A. K. Sood, K. S. Subrahmanyam, Govindaraj and Angew. *Chem. Int. Ed*., 2009, **48**, 7752-7777.

34. A. C. Ferrari, F. Bonaccorso, V. Falko, K. S. Novoselov, S. Roche, P. Boggild, S. Borini, F. H. Koppens, V. Palermo, N. Pugno, J. A. Garrido, R. Sordan, A. Bianco, L. Ballerini, M. Prato, E. Lidorikis, J. Kivioja, C. Marinelli, T. Ryhanen, A. Morpurgo, J. N. Coleman, V. Nicolosi, L. Colombo, A. Fert, M. Garcia-Hernandez, A. Bachtold, G. F. Schneider, F. Guinea, C. Dekker, M. Barbone, Z. Sun, C. Galiotis, A. N. Grigorenko, G. Konstantatos, A. Kis, M. Katsnelson, L. Vandersypen, A. Loiseau, V. Morandi, D. Neumaier, E. Treossi, V. Pellegrini, M. Polini, A. Tredicucci, G. M. Williams, B. H. Hong, J. H. Ahn, J. M. Kim, H. Zirath, B. J. van Wees, H. van der Zant, L. Occhipinti, A. D. Matteo, I. A. Kinloch, T. Seyller, E. Quesnel, X. Feng, K. Teo, N. Rupesinghe, P. Hakonen, S. R. Neil, Q. Tannock, T. Lofwander and J. Kinaret, *Nanoscale.,* 2015, **7**, 4598-4810.

35. E. P. Randviir, D. A. C. Brownson and C. E. Banks, *Mater. Today.,* 2014, **17**, 426-432.

36. K. S. Novoselov, V. I. Falko, L. Colombo, P. R. Gellert, M. G. Schwab and K. Kim, *Nature.,* 2012, **490**, 192-200.

37. A. K. Geim, *Science.,* 2009, **324**, 1530-1534.

38. A. K. Geim and K. S. Novoselov, *Nat. Mater.,* 2007, **6**, 183-191.

39. M. Yiand Z. Shen, *RSC Adv.,* 2016, **6**, 72525-72536.

40. N. Krane, *Growth Lakel.,* 1993, **4**, 1-5.

41. M. Cai, D. Thorpe, D. H. Adamson and H. C. Schniepp, *J. Mater. Chem.,* 2012, **22**, 24992-25002.

42. Y. Hernandez, V. Nicolosi, M. Lotya, F. M. Blighe, Z. Sun, S. De, I. T. McGovern, B. Holland, M. Byrne, Y. K. Gunko, J. J. Boland, P. Niraj, G. Duesberg, S. Krishnamurthy, R. Goodhue, J. Hutchison, V. Scardaci, A. C. Ferrari and J. N. Coleman, *Nat. Nanotechnol.,* 2008, **3**, 563-568.

43. W. Hummers Jr and J. R. Offeman, *J. Am. Chem. Soc.,* 1958, **80**, 1339-1339.

44. S. Park and R. S. Ruoff, *Nat. Nanotechnol.,* 2009, **4**, 217-224.

45. S. V. Tkachev, E. Y. Buslaeva, and S. P. Gubin, *Inorg. Mater.,* 2011, **47**, 5-14.

46. M. Zhou, T. Tian, X. Li, X. Sun, J. Zhang, P. Cui, J. Tang, and L. C. Qin, *Int. J. Electrochem. Sci.,* 2014, **9**, 810-820.

47. X. Cui, C. Zhang, R. Hao and Y. Hou, *Nanoscale.,* 2011, **3**, 2118-2126.

48. J. N. Coleman, *Acc. Chem. Res.,* 2013, **46**, 14-22.

49. Y. Arao, F. Mori and M. Kubouchi, *Carbon.,* 2017, **118**, 18-24.

50. J. Hass, W. A. de Heer and E. H. Conrad, *J. Phys. : Condens. Matter.,* 2008, **20**, 323202-323228.

51. C. Berger, Z. Song, X. Li, X. Wu, N. Brown, C. Naud, D. Mayou, T. Li, J. Hass, A. N. Marchenkov, E. H. Conrad, P. N. First, W. A. de Heer, 2006, *Science.,* **312**, 1191-1196.

52. S. Shivaraman, R. A. Barton, X. Yu, J. Alden, L. Herman, M. V. S Chandrashekhar, J. Park, P. L. McEuen, J. M. Parpia, H. G. Craighead, and M. G. Spencer, *Nano Lett.,* 2009, **9**, 3100-3105.

53. V. Y. Aristov, G. Urbanik, K. Kummer, D. V. Vyalikh, O. V. Molodtsova, A. B. Preobrajenski, A. A. Zakharov, C. Hess, T. Hanke, B. Buchner, I. Vobornik, J. Fujii, G. Panaccione, Y. A. Ossipyan and M. Knupfer, *Nano Lett.,* 2010, **10**, 992-995.

54. Q. Huang, J. J. Kim, G. Ali, and S. O. Cho, *Adv. Mater.,* 2013, **25**, 1144-1148.

55. A. Reina, X. Jia, J. Ho, D. Nezich, H. Son, V. Bulovic, M. S. Dresselhaus and J. Kong, *Nano Lett.,* 2009, **9**, 30-35.

56. S. Chen, L. Brown, M. Levendorf, W. Cai, S. –Y. Ju, J. Edgeworth, X. Li, C. W. Magnuson, A. Velamakanni, R. D. Piner, J. Kang, J. Park and R. S. Ruoff, *ACS Nano*., 2011, **5**, 1321-1327.

57. S. Bae, H. Kim, Y. Lee, X. Xu, J. Park, Y. Zheng, J. Balakrishnan, T. Lei, H. R. Kim, Y. I. Song, Y. J. Kim, K. S. Kim, B. Zyilmaz, J. H. Ahn, B. H. Hong and S. Iijima, *Nat. Nanotechnol.,* 2010, **5**, 574-578.

58. P. W. Sutter, J. I. Flege and E. A. Sutter, *Nat. Mater.,* 2008, **7**, 406-411.

59. W. Strupinski, K. Grodecki, A. Wysmolek, R. Stepniewski, T. Szkopek, P. E. Gaskell, A. Gruneis, D. Haberer, R. Bozek, J. Krupka and J. M. Baranowski, *Nano Lett.,* 2011, **11**, 1786-1791.

60. X. Li, W. Cai, J. An, S. Kim, J. Nah, D. Yang, R. Piner, A. Velamakanni, I. Jung, E. Tutuc, S. K. Banerjee, L. Colombo and R. S. Ruoff, *Science.,* 2009 , **324**, 1312-1314.

61. H. Ago, Y. Ito, N. Mizuta, K. Yoshida, B. Hu, C. M. Orofeo, M. Tsuji, K. Ikeda and S. Mizuno, *ACS Nano.,* 2010, **4**, 7407-7414.

62. K. S. Kim, Y. Zhao, H. Jang, S. Y. Lee, J. M. Kim, K. S. Kim, J. -H. Ahn, P. Kim, J. -Y. Choi and B. H. Hong, *Nature.,* 2009, **457**, 706-710.

63. A. Reina, S. Thiele, X. Jia, S. Bhaviripudi, M. S. Dresselhaus, J. A. Schaefer and J. Kong, *Nano Res.,* 2009, **2**, 509-516.

64. C. Mattevi, H. Kim and M. Chhowalla, *J. Mater. Chem.,* 2011, **21**, 3324-3334.

65. Y. Zhang, L. Zhang and C. Zhou*, Acc. Chem. Res.,* 2013, **46**, 2329-2339.

66. P. R. Somani, S. P. Somani and M. Umeno, *Chem. Phys. Lett.,* 2006, **430**, 56-59.

67. X. Wang, H. You, F. Liu, M. Li, L. Wan, S. Li, Q. Li, Y. Xu, R. Tian, Z. Yu, D. Xiang, and J. Cheng, *Chem. Vap. Deposition.,* 2009, **15**, 53-56.

68. D. V. Kosynkin, A. L. Higginbotham, A. Sinitskii, J. R. Lomeda, A. Dimiev, B. K. Price, and J. M. Tour, *Nature.,* 2009, **458**, 872-877.

69. L. Jiao, L. Zhang, X. Wang, G. Diankov, and H. Dai, *Nature.,* 2009, **458**, 877-880.

70. A. G. Cano-Marquez, F. J. Rodrıguez-Macıas, J. Campos- Delgado, C. G. Espinosa-Gonzalez, F. Tristan-Lopez, D. Ramıre- Gonzalez, D. A. Cullen, D. J. Smith, M. Terrones, and Y. I. Vega-Cantu, *Nano Lett.,* 2009, **9**, 1527-1533.

71. W. Choi, I. Lahiri, R. Seelaboyina and Y. S. Kang, *Crit. Rev. Solid State Mater. Sci.,* 2010, **35**, 52-71.

72. S. Stankovich , D. A. Dikin , R. D. Piner , K. A. Kohlhaas , A. Kleinhammes, Y. Jia , Y. Wu , S. B. T. Nguyen and R. S. Ruoff, *Carbon.,* 2007, **45**, 1558-1565.

73. L. Staudenmaier, *Ber Dtsch Chem Ges*., 1898, **31,** 1481–1487.

74. B. C. Brodie, *Phil. Trans. R. Soc. Lond.,* 1859, **149**, 249-259.

75. S. Park, J. An, J. R. Potts, A. Velamakanni, S. Murali and R. S. Ruoff, *Carbon.,* 2011, **49**, 3019-3023.

76 . S. Abdolhosseinzadeh, H. Asgharzadeh and H. S. Kim, *Sci. Rep.,* 2015, **5**, 1-7.

77. Q. Ke and J. Wang, *J Materiomics.,* 2016, **2**, 37-54.

78. M. Acik and Y. J. Chabal, *J. Mat. Sci. Res.,* 2013, **2**, 101-112.

79. H. L. Poh, F. S. A. Ambrosi, G. Zhao, Z. Sofer and M. Pumera, *Nanoscale.,* 2012, **4**, 3515-3522.

80. O. Kamigaito, *J Jpn Soc Powder Powder Metall.,* 1991, **38**, 315-321.

81. P. M. Ajayan, L. S Schadler and P. V. Braun, *Nanocomposite Science and Technology*, 2004, Wiley: New York, Wiley□VCH Verlag GmbH & Co. KGaA, DOI: 10. 1002/3527602127.

82. H. Ishida, S. Campbell and J. Blackwell, *Chem. Mater.,* 2000, **12**, 1260-1267.

83. P. H. C. Camargo, K. G. Satyanarayana, F. Wypych, *Mat. Res.,* 2009, **12**, 1-39.

84. C. C. Okpala, *IJERD.,* 2013, **8**, 17-23.

85. B. Garg, T. Bisht and Y. -C. Ling, *Molecules.,* 2014, **19**, 14582-14614.

86. D. G. Papageorgiou, I. A. Kinloch and R. J. Young, *Prog. Mat. Sci.,* 2017, **90**, 75-127.

87. N. Hashim, Z. Muda, M. Z. Hussein, I. M. Isa, A. Mohamed, A. Kamari, S. Abubakar, M. Mamat and A. M. Jaafar, *J. Mater. Environ. Sci.,* 2016*,* **7**, 3225-3243.

88. C. Hu, T. Lu, F. Chen and R. Zhang, *J. Chin. Adv. Mat. Soc.,* 2013, **1**, 21-39.

89. H. Chang and H. Wu, *Energy Environ. Sci.,* 2013, **6**, 3483-3507.

90. Y. Cheng, Y. Fan, Y. Pei and M. Qiao, *Catal. Sci. Technol.,* 2015, **5**, 3903-3916.

91. X. Huang, Z. Yin, S. Wu, X. Qi, Q. He, Q. Zhang, Q. Yan, F. Boey and H. Zhang, *Small.,* 2011, **7***,* 1876-1902.

92. R. K. Upadhyaya, N. Soinb and S. S. Roy*, RSC Adv.,* 2014, **4**, 3823-3851.

93. V. Singh, D. Joung, L. Zai, S. Das, S. I. Khondaker and S. Seal, *Prog. Mater. Sci.,* 2011, **56**, 1178-1271.

94. Y. Liu, G. Zhao, D. Wang and Y. Li, *Natl Sci Rev.,* 2015, **2**, 150-166.

95. B. Sels and M. V. Voorde, *Nanotechnology in Catalysis: applications in the chemical industry, energy development and environment protection,* 2017, Weinheim : Wiley-VCH, Science.

96. S. P. Lonkar and A. A. Abdala, *J Thermodyn. Catal*., 2014, **5**, 1-10.

97. K. Varshney, *Int. j. eng. res. sci.,* 2014, **2**, 660-677.

98. V. Georgakilas, J. A. Perman, J. Tucekand R. Zboril, *Chem. Rev.,* 2015, **115**, 4744-4822.

99. J. Bartelmess and S. Giordani, *Beilstein J. Nanotechnol.* 2014, **5***,* 1980-1998.

100. B. Coq, J. M. Planeix and V. Brotons, *Appl. Catal. A.,* 1998, **173**, 175-183

101. M. S. Dresselhaus, G. Dresselhaus and P. C. Eklund, *Science of Fullerenes and Carbon Nanotubes: Their Properties and Applications, Academic press, Elsevier,* 1996.

102. P. Serp and B. Machado, *RSC cat.,* 2015, **23**, 1-555.

103. B. Li and Z. Xu, *J. Am. Chem. Soc.,* 2009, **131**, 16380-16382.

104. N. Muradov, *Catal. Commun.,* 2001, **2**, 89-94.

105. M. Croston, J. Langston, R. Sangoiy, and K. S. V. Santhanam, *Int. J. Nanosci.,* 2002, **1**, 277-283.

106. M. Croston, J. Langston, G. Takacs, T. C. Morrill, M. Miri, K. S. V. Santhanam and P. Ajayan*, Int. J. Nanosci.,* 2002, **1**, 285-293.

107. Y. Zhao, C. Zhang, T. Liu, R. Fan, Y. Sun, H. Tao and J. Xu*e*, *Int. J. Electrochem. Sci.,* 2017, **12**, 3537-3548

108. B. Dai, K. Chen, Y. Wang, L. Kang, and M. Zhu, *ACS Catal.,* 2015**,** **4**, 2541-2547.

109. L. Wang, H. Dong, Z. Guo, L. Zhang, T. Hou, and Y. Li, *J. Phys. Chem. C.,* **120,** 17427-17434.

110. Y. Lin, Y. Liao, Z. Chen and J. W. Connell, *Mater. Res. Lett.,* 2017, 5, 209-234.

111. Y. Lin, K. A. Watson, J. W. Kim, D. W. Baggett, D. C. Working and J. W. Connell, *Nanoscale.,* 2013, **5**, 7814-7824.

112. F. Banhart, J. Kotakoski and A. V. Krasheninnikov, *ACS Nano.,* 2011, **5**, 26-41.

113. H. Terrones, R. T. Lv, M. Terrones and M. S. Dresselhaus, *Rep. Prog. Phys.,* 2012, **75**, 062501-062530.

114. O. Akhavan, *ACS Nano.,* 2011, **4**, 4174-4180.

115. Z. Zeng, X. Huang, Z. Yin, H. Li, Y. Chen, H. Li, Q. Zhang, J. Ma, F. Boey and H. Zhang, *Adv. Mater*., 2012, **24**, 4138-4142.

116. X. Zhao, C. M. Hayner, M. C. Kung and H. H. Kung, *Adv. Energy Mater.,* 2011, **1**, 1079-1084.

117. T. Han, Y. Huang, A. Tan, V. Dravid and J. Huang, *J. Am. Chem. Soc.,* 2011, **133**, 15264-15267.

118. R. K. Paul, S. Badhulika, N. M. Saucedo and A. Mulchandani, *Anal. Chem*., 2012, **84**, 8171-8178.

119. Y. Fang, Y. Lv, R. Che, H. Wu, X. Zhang, D. Gu, G. Zheng and D. Zhao, *J. Am. Chem. Soc.,* 2013, **135**, 1524-1530.

120. X. Zhao, C. M. Hayner, M. C. Kung and H. H. Kung, *ACS Nano.,* 2011, **5**, 8739-8749.

121. J. C. Charlier, *Acc Chem Res.,* 2002, **35**, 1063-1069.

122. Y. Xu, C. Y. Chen, Z. Zhao, Z. Lin, C. Lee, X. Xu, C. Wang and Y Huang, *Nano Lett.,* 2015, **15**, 4605-4610.

123. X. Han, M. R. Funk, F. Shen, Y. C. Chen, Y. Li, C. J. Campbell, J. Dai, X. Yang, J. W. Kim, Y. Liao, J. W. Connell, V. Barone, Z. Chen, Y. Lin, and L. Hu, *ACS Nano.,* 2014, **8**, 8255-8265.

124. Y. Xu, Z. Lin, X. Zhong, X. Huang, N. O. Weiss, Y. Huang and X. Duan, *Nat. Commun*., 2014, **5**, 4554-4561.

125. J. Bai, X. Zhong, S. Jiang, Y. Huang and X. Duan, *Nat. Nanotechnol*., 2010, **5**, 190-194.

126. B. Choi, S. Chang, Y. Lee, J. Bae, H. Kim and Y. Huh, *Nanoscale.,* 2012, **4**, 5924-5930.

127. Z. Wang, D. Xu, H. Wang, Z. Wu and X. Zhang, *ACS Nano.,* 2013, **7**, 2422-2430.

128. O. Akhavan and E. Ghaderi, *Small.,* 2013, **9**, 3593-3601.

129. G. Ning, Z. Fan, G. Wang, J. Gao, W. Qian and F. Wei, *Chem. Commun*., 2011, **47**, 5976-5978.

130. G. Ning, C. Xu, L. Mu, G. Chen, G. Wang, J. Gao, Z. Fan, W. Qian and F. Wei, *Chem. Commun*., 2012, **48**, 6815-6817.

131. X. Zhu, G. Ning, X. Ma, Z. Fan, C. Xu, J. Gao, C. Xu and F. Wei, *J. Mater. Chem. A.,* 2013, **1**, 14023-14030.

132. Z. Fan, Q. Zhao, T. Li, J. Yan, Y. Ren, J. Feng and T. Wei, *Carbon.,* 2012, **50**, 1699-1703.

133. X. Wang, L. Jiao, K. Sheng, C. Li, L. Dai and G. Shi, *Sci. Rep*., 2013, **3**, 1-5.

134. S. Chen, J. Duan, M. Jaroniec and S. Qiao, *J. Mater. Chem. A*., 2013, **1**, 9409-9413.

135. S. Chen, J. Duan, Y. Tang and S. Qiao, *Chem. Eur. J.,* 2013, **19**, 7118-7124.

136. Z. Jiang, B. Pei and A. Manthiram, *J. Mater. Chem. A.,* 2013, **1**, 7775-7781.

137. J. G. Radich and P. V. Kamat, *ACS Nano.,* 2013, **7**, 5546-5557.

138. Y. Chen, Z. P. Michael, G. P. Kotchey, Y. Zhao, and A. Star, *ACS Appl. Mater. Interfaces.,* 2014, **6**, 3805-3810.

139. K. Xia, X. Tian, S. Fei and K. You, *Int J Hydrogen Energy.,* 2014, **39**, 11047-11054.

140. X. -H. Li and M. Antonietti, *Angew. Chem. Int. Ed.,* 2013, **52**, 1-6.

141. Z. Jiang, Z. Jiang, X. Tian and W. Chena, *J. Mater. Chem. A.,* 2014, **2**, 441-450.

142. X. Lv, W. Lv, W. Wei, X. Zheng, C. Zhang, L. Zhi and Q. Yang, *Chem. Commun*., 2015, **51**, 3911-3914.

143. Z. Jiang, Y. Shi, Z. Jiang, X. Tian, L. Luo and W. Chen, *J. Mater. Chem. A.,* 2014, **2**, 6494-6503.

144. D. H. Wang, Y. Hu, J. J. Zhao, L. L. Zeng, X. M. Tao and W. Chen, *J. Mater. Chem. A.,* 2014, **2**, 17415-17420.

145. Y. -Y. Peng, Y. –M. Liu, J. –K. Chang, C. –H. Wu, M. –D. Ger, N. –W. Pu and C. –L. Chang, *Carbon.,* 2015, **81**, 347-356.

146. Z. Xing, J. Tian, Q. Liu, A. M. Asiri, P. Jiang and X. Sun, 2014, *Nanoscale.,* 2014, **6**, 11659-11663.

147. Z. Jiang, Z. Jiang and W. Chen, *J Power Sources.,* 2014, **251**, 55-65.

148. J. Ge, B. Zhang, L. Lv, H. Wang, T. Ye, X. Wei, J. Su, K. Wang, X. Lin, J. Chen, *Nano Energy. .,* 2015, **15**, 567-575.

149. D. Yu, L. Wei, W. Jiang, H. Wang, B. Sun, Q. Zhang, K. Goh, R. Sia and Y. Chen, *Nanoscale.,* 2013, **5**, 3457-3464.

150. X. Zhou, Z. Bai, M. Wu, J. Qiao and Z. Chen, *J. Mater. Chem. A.,* 2015, **3**, 3343-3350.

151. J. Mahmood, E. K. Lee, M. Jung, D. Shin, I. Jeon, S. Jung, H. Choi, J. Seo, S. Bae, S. Sohn, N. Park, J. H. Oh, H. Shin and J. Baek, *Nat Commun*., 2015, **6**, 6486 (1-7).

152. M. Patel, W. Feng, K. Savaram, M. Khoshi, R. Huang, J. Sun, E. Rabie, C. flach, R. Mendelsohn and E. Garfunke, H. He*, Small.,* 2015, **11**, 3358-3368.

153. J. Xu, Y. Lin, J. W. Connell and L. Dai, *Small.,* 2015, **46**, 6179-6185

154. X. Wang , L. Lv , Z. Cheng , J. Gao , L. Dong , C. Hu , and L. Qu, *Adv. Energy Mater*., 2016, **6**, 1502100 (1-7).

155. J. Shui, Y. Lin, J. W. Connell, J. Xu, X. Fanand L. Dai, *ACS Energy Lett.,* 2016, **1**, 260-265

156. Z. Jiang, and Z. Jiang, *ACS Appl. Mater. Interfaces.,* 2014, ***6***, 19082-19091.

157. M. Kotal, H. Kim, S. Roy and I. Oh, *J. Mater. Chem. A.,* 2017, **5**, 17253-17266.

158. X. Li, J. Yu, S. Wageh, A. A. Al-Ghamdi, and J. Xie, *Small.,* 2016, **12**, 6640-6696.

159. X. Chen, S. Shen, L. Guo and S. S. Mao, *Chem. Rev.,* 2010, **110**, 6503-6570.

160. K. Maeda and K. Domen, *J. Phys. Chem.,* 2007, **111**, 7851-7861.

161. F. E. Osterloh, *Chem. Mater*., 2007, **20**, 35-54.

162. A. Kudo and Y. Miseki, *Chem. Soc. Rev.,* 2009, **38**, 253-278.

163. X. Li, J. Yu, J. Low, Y. Fang, J. Xiao, X. Chen, *J. Mater. Chem. A.,* 2014, **3**, 2485-2534.

164. S. C. Roy, O. K. Varghese, M. Paulose and C. A. Grimes, *ACS Nano*, 2010, **4**, 1259-1278.

165. A. M. Appel, J. E. Bercaw, A. B. Bocarsly, H. Dobbek, D. L. DuBois, M. Dupuis, J. G. Ferry, E. Fujita, R. Hille, P. J. A. Kenis, C. A. Kerfeld, R. H. Morris, C. H. F. Peden, A. R. Portis, S. W. Ragsdale, T. B. Rauchfuss, J. N. H. Reek, L. C. Seefeldt, R. K. Thauer and G. L. Waldrop, *Chem. Rev.,* 2013, **113**, 6621-6658.

166. S. N. Habisreutinger, L. Schmidt-Mende and J. K. Stolarczyk, *Angew. Chem. Int. Ed.,* 2013, **52**, 7372-7408.

167. X. Li, J. Wen, J. Low, Y. Fang and J. Yu, *Sci. China Mater.,* 2014, **57**, 70-100.

168. M. Marszewski, S. Cao, J. Yu and M. Jaroniec, *Mater. Horiz.,* 2015, **2**, 261-278.

169. M. Hoffmann, S. Martin, W. Choi and D. Bahnemann, *Chem. Rev.,* 1995, **95**, 69-96.

170. A. D. Paola, E. Garcia-Lopez, G. Marci and L. Palmisano, *J. Hazard. Mater.,* 2012, **211**, 3-29.

171. M. Pelaez, N. T. Nolan, S. C. Pillai, M. K. Seery, P. Falaras, A. G. Kontos, P. S. M. Dunlop, J. W. J. Hamilton, J. A. Byrne, K. OShea, M. H. Entezari and D. D. Dionysiou, *Appl. Catal.* B., 2012, **125**, 331-349.

172. H. Park, Y. Park, W. Kim and W. Choi, *J. Photochem. Photobiol. C.,* 2013, **15**, 1-20.

173. X. Lang, X. Chen and J. Zhao, *Chem. Soc. Rev.,* 2014, **43**, 473-486.

174. S. Pourbeyram, *Ind. Eng. Chem. Res.,* 2016, **55**, 19, 5608-5617.

175. M. R. Gandhi, S. Vasudevan, A. Shibayama and M. Yamada, *Chemistry Select.,* 2016, **1**, 4358-4385.

176. M. J. Lü, J. Li, X. Y. Yang, C. A. Zhang, J. Yang, H. Hu and X. B. Wang, *Chin. Sci. Bull.,* 2013, **58**, 2698-2710.

177. B. Y. Z. Hiewa, L. Y. Leea, X. J. Leea, S. T. Gopakumar, S. Gan, S. S. Lim, G. T. Pan, T. C. K. Yang, W. S. Chiu, P. S. Khiew, *Process Saf. Environ. Prot.,* 2018, **116**, 262-286.

178. S. J. Shan, Y. Zhao, H. Tang and F. Y. Cui, *Earth Environ. Sci.,* 2017, **68**, 012003(1-7).

179. A. Sirelkhatim, S. Mahmud, A. Seeni, N. H. M. Kaus, L. C. Ann, S. K. M. Bakhori, H. Hasan, D. Mohamad, *Nano-micro Lett.,* 2015, **7**, 219-242.

180. M. Purica, E. Budianu and E. Rusu, *Thin Solid Films.,* 2001, **383**, 284-286.

181. T. Aoki, Y. Hatannaka and D. C. Look, *Appl. Phys. Lett.,* 2000, **76**, 3257-3258.

182. C. R. Gorla, N. W. Emanetoglu, S. Liang, W. E. Mayo, Y. Lu, M. Wraback and H. Shen, *J. Appl. Phys*., 1999, **85**, 2595-2602.

183. S. H. Jo, J. Y. Lao, Z. F. Ren, R. A. Farrer, T. Baldacchini and J. T. Fourkas, *Appl. Phys. Lett*., 2003, **83**, 4821-4823.

184. M. S. Arnold, P. Avouris, Z. W. Pan and Z. L. Wang, *J. Phys. Chem*., 2003, **107**, 659-663.

185. F. C. Lin, Y. Takao, Y. Shimizu and M. Egashira, *Sens. Actuators B Chem.,* 1995, **24**, 843-850.

186. K. S. Weissenrieder and J. Muller, *Thin Solid Films.,* 1997, **300**, 30-41.

187. J. Muller and K. S. Weissenrieder, *J. Anal. Chem*., 1994, **349**, 380-384.

188. W. Water, S. E. Chen, T. H. Meen and L. W. Ji, *Ultrasonics.,* 2012, **52**, 747-752.

189. J. Singh, J. Im, J. E. Whitten, J. W. Soares, A. M. Meehan and D. M. Steeves, *Proc. of SPIE,* 2008, **7030**, *70300T* (1-8).

190. H. Q. Yan, R. R. He, J. Johnson, M. Law, R. J. Saykally and P. Yang, *J. Am. Chem. Soc*., 2003, **125**, 4728-4729.

191. E. Bacaksiz, M. Parlak, M. Tomakin, A. Ozcelik, M. Karakiz and M. Altunbas, *J. Alloy. Compd.,* 2008, **466**, 447-450.

192. J. Wang, J. Cao, B. Fang, P . Lu, S. Deng and H. Wang, *Mater. Lett.* 2005, **59**, 1405-1408.

193. Z. L. Wang, *J. Phys. : Condens. Matter.,* 2004, **16**, R829-R858.

194. Z. L. Wang, *ACS Nano*., 2008, **2**, 1987-1992.

195. M. Chaari and A. Matoussi, *Phys. B Condens. Matter.,* 2012, **407**, 3441-3447.

196. M. T. Mohammad, A. A. Hashim and M. H. Al-Maamory, *Mater. Chem. Phys.,* 2006, **99**, 382-387.

197. L. Znaidi, G. J. A. A. Soler Illia, S. Benyahia, C. Sanchez, A. V. Kanaev, *Thin Solid Films.,* 2003, **428**, 257–262.

198. G. C. Yi, C. Wang and W. I. Park, *Semicond. Sci. Technol.,* 2005, **20**, S22-S34.

199. B. V. kumar, H. S. B. Naik, D. Girija and B. Vijaya kumar, *J. Chem. Sci.,* 2011, **123**, 615-621.

200. K. Matsubara, P. Fons, K. Iwata, A. Yamada, K. Sakurai, H. Tampo, S. Niki, *Thin Solid Films.,* 2003, **431-432**, 369-372.

201. U. Ozgur, Y. I. Alivov, C. Liu, A. Teke, M. A. Reshchikov, S. Doğan, V. Avrutin, S. J. Cho, H. J. Morkoc, *J. Appl. Phys.,* 2005, **98**, 041301 (1-103).

202. S. Bhattacharyya and A. Gedanken, *Microporous Mesoporous Mater.,* 2007, **110**, 553-559.

203. B. Ludi and M. Niederberger, *Dalton Trans.* 2013, **42**, 12554-12568.

204. D. Banerjee, J. Y. Lao, D. Z. Wang, J. Y. Huang, Z. F. Ren, D. Steeves, B. Kimball and M. Sennett, *Appl. Phys. Lett.,* 2003, **83**, 2061-2063.

205. Y. B. Hahn, *Korean J. Chem. Eng.* 2011, **28**, 1797-1813.

206. T. Frade, Melo, M. E. Jorge, A. Gomes, *Mater. Lett.,* 2012, **82**, 13-15.

207. R. Wahab, S. G. Ansari, Y. S. Kim, H. K. Seo and H. S. Shin, *Appl. Surf. Sci.,* 2007, **253**, 7622-7626.

208. X. Y. Kong, Y. Ding, R. Yang and Z. L. Wang*, Science.,* 2004, **303**, 1348-1351.

209. Z. W. Pan, Z. R. Dai and Z. L. Wang, *Science. .,* 2001, **291**, 1947-1949.

210. J. J. Wu, S. C. Liu, C. T. Wu, K. H. Chen and L. C. Chenm, *Appl. Phys. Lett.,* 2002, **81**, 1312-1314.

211. W. J. Chen, W. L. Liu, S. H. Hsieh and T. K. Tsai, *Appl. Surf. Sci.,* 2007, **253**, 6749-6753.

212. J. Liu, X. Huang, J. Duan, H. Ai and P. Tu, *Mater. Lett.,* 2005, **59**, 3710-3714.

213. Y. Huang, J. He, Y. Zhang, Y. Dai, Y. Gu, S. Wang and C. J. Zhou, *JMater. Sci.,* 2006, **41**, 3057-3062.

214. B. Nikoobakht, X. Wang, A. Herzing and J. Shi, *Chem. Soc. Rev.,* 2013, **42**, 342-365.

215. L. C. Tien, S. J. Pearton, D. P. Norton and F. J. Ren, *Mater. Sci.,* 2008, **43**, 6925-6932.

216. J. Cui, *Mater. Charact.,* 2012, **64**, 43-52.

217. T. Xu, P. Ji, M. He and J. J. Li, *Nanomater.,* 2012, 797935 (1-5). Doi:10. 1155/2012/797935.

218. W. S. Chiua, P. S. Khiew, M. Clokea, D. Isaa, T. K. Tana, S. Radimanb, R. A. Shukorb, M. A. Abd–Hamid, N. M. Huangc and H. N. Limd, *Chem. Eng. J.,* 2010, **158**, 345-352.

219. M. J. Yacaman, C. G. Wing, M. Miki, D. Q. Yang, K. N. Piyakis and E. Sacher, *J. Phys. Chem. B.,* 2005, **109**, 9703-9711.

220. V. Polshettiwar, B. Baruwati and R. S. Varma, *ACS Nano.,* 2009, **3**, 728-736.

221. Q. Xie, Z. Dai, J. Liang, L. Xu, W. Yu and Y. Qian, *Solid State Commun.,* 2005, **136**, 304-307.

222. J. Liu, X. Huang, Y. Li, K. M. Ulieman, F. Sun and X. He, *Scr. Mater.,* 2006, **55**, 795-798.

223. M. Bitenc and Z. C. Orel, *Mater. Res. Bull.,* 2009, **44**, 381-387.

224. A. K. Radzimska and T. Jesionowski, *Materials.,* 2014, **7**, 2833-2881.

225. A. B. Djuriscic, X. Y. Chen and Y. H. Lung, *Recent Pat. Nanotechnol.,* 2012, **6**, 124-134.

226. S. J. Chen, L. H. Li, X. T. Chen, Z. Xue, J. M. Hong and X. Z. You, *J. Cryst. Growth,* 2003, **252**, 184-189.

227. J. Zhang, J. Wang, S. Zhou, K. Duan, B. Feng, J. Weng, H. Tang and P. J. Wu, *Mater. Chem.,* 2010, **20**, 9798-9804.

228. J. Ma, J. Liu, Y. Bao, Z. Zhu, X. Wang and J. Zhang, *Ceram. Int.,* 2013, **39**, 2803-2810.

229. O. Carp, C. L. Huisman and A. Reller, *Prog Solid State Ch.,* 2004, **32**, 33–177.

230. A. L. Linsebigler, G. Lu and J. T. Yates Jr, *Chem. Rev.,* 1995, **95**, 735-758.

231. R. Li, Y. Weng, X. Zhou, X. Wang, Y. Mi, R. Chong, H. Han and C. Li, *Energy Environ. Sci.,* 2015, **8**, 2377-2382.

232. H. Yan, X. Wang, M. Yaon and X. Yao, *Prog. Nat. Sci. Mater. Int.,* 2013, **23**, 402-407.

233. A. Fujishima, X. Zhang and D. A. Tryk, *Surf Sci Rep.,* 2008, 63, 515-582.

234. C. Dette, M. A. Perez-Osorio, C. S. Kley, P. Punke, C. E. Patrick, P. Jacobson, F. Giustino, S. J. Jungand K. Kern, *Nano Lett*., 2014, **14**, 6533-6538.

235. D. S. Hall, D. J. Lockwood, C. Bock and B. R. MacDougall, *Proc. R. Soc. A,* 2015*,* **471**, 20140792 (1-65).

236. P. Oliva, J. Leonard and J. F. Laurent, *J Power Sources.,* 1982, **8**, 229-255.

237. A. Livingstone and D. Bish, *Scotland. Mineral. Mag.,* 1982, **46**, 1-5.

238. T. Marcopoulos and M. Economou, *Am. Mineral.,* 1981, **66**, 1020-1021.

239. R. S. McEwen, *J. Phys. Chem.,* 1971, **75**, 1782-1789.

240. C. Tessier, P. H. Haumesser, P. Bernard and C. Delmas , *J. Electrochem. Soc.,* 1999, **146**, 2059-2067.

241. T. B. Reddy andD. Linden, *Linden's handbook of batteries*, 2011, 4th edn. New York, NY:McGraw-Hill.

242. J. Mc Breen, *Nickel hydroxides. In Handbook of battery materials,* 2011, 2nd edn. Weinheim, Germany:Wiley-VCH Verlag GmbH & Co. KGaA.

243. A. Rabenau, *Angew. Chemie Int.,* 1985, **24**, 1026-1040.

244. M. Dixit, G. N. Subbanna and P. V. Kamath, *J. Mater. Chem.,* 1996, **6**, 1429-1432.

245. L. -X. Yang, Y. -J. Zhu, H. Tong, Z. -H. Liang, L. Li, L. Zhang, *J Solid State Chem.,* 2007, **180**, 2095-2101.

246. L. Dong, Y. Chu and W. Sun, *Chem. Eur. J.,* 2008, **14**, 5064-5072.

247. X. Ma, J. Liu, C. Liang, X. Gong and R. Che, *J. Mater. Chem. A.,* 2014, **2**, 12692-12696

248. Y. Fan, Z. Yang, X. Cao, P. Liu, S. Chen and Z. Cao, *J. Electrochem. Soc.,* 2014, **161**, B201-B206.

249. J. Ran, J. Yu and M. Jaroniec, *Green Chem.,* 2011, **13**, 2708-2713.

250. Z. Yan, X. Yu, Y. Zhang, H. Jia, Z. Sun and P. Du, *Appl. Catal. B.,* 2014, **160-161**, 173-178.

251. J. Yu, Y. Hai and B. Cheng, *J. Phys. Chem. C.,* 2011, **115**, 4953-4958.

252. M. Gao, W. Sheng, Z. Zhuang, Q. Fang, S. Gu, J. Jiang and Y. Yan, *J. Am. Chem. Soc.,* 2014, **136**, 7077-7084.

253. M. E. G. Lyons, A. Cakara, P. O'Brien, I. Godwin and R. L. Coyle, *Int. J. Electrochem. Sci.,* 2012, **7**, 11768-11795.

254. M. Vidotti, R. Torresi, D. Torresi, *Quim. Nova,* **33**, 2176-2186.

255. M. Aghazadeh, M. Ghaemi, B. Sabour and S. Dalvand, *J. Solid State Electrochem*., 2014, **18**, 1569-1584.

256. J. C. Chen, C. T. Hsu and C. C. Hu, *J. Power Sources.,* 2014, **253**, 205-213.

257. H. Cheng, A. D. Su, S. Li, S. T. Nguyen, L. Lu, C. Y. H Lim and H. M. Duong*, Chem. Phys. Lett.,* 2014, **601**, 168-173.

258. J. Huang, T. Lei, X. Wei, X. Liu, T. Liu, D. Cao, J. Yin and G. Wang, *J. Power Sources.,* 2013, **232**, 370-375.

259. M. Sebastian, C. Nethravathi and M. Rajamathi, *Mater. Res. Bull*., 2013, **48**, 2715-2719.

260. S. I. C. Torresi, C. Gabrielli, A. H. L. Goff and R. Torresi, *J. Electrochem. Soc*., 1991, **138**, 1548-1553.

261. R. Mortimer, M. Sialvi, T. Varley and G. Wilcox, *J. Solid State Electrochem.,* 2014, **18**, 3359-3367.

262. P. K. Sharma, M. C. A Fantini and A. Gorenstein, *Solid State Ionics.,* 1998, **113-115**, 457-463.

263. Y. Miao, L. Ouyang, S. Zhou, L. Xu, Z. Yang, M. Xiao and R. Ouyang, *Biosensors Bioelectr.,* 2014, **53**, 428-439.

264. S. Rastgar and S. Shahrokhian, *Talanta.,* 2014, **119**, 156-163.

265. H. Yang, G. Gao, F. Teng, W. Liu, S. Chen and Z. Ge, *J. Electrochem. Soc.,* 2014, **161**, B216-B219.

Chapter 2

Experimental Methods and Characterization Techniques

2.1 Introduction

Catalytic activity of a nanocomposite strongly depends on the way it is prepared. Even a small change in the conditions employed for preparation can influence the property of the composite. Therefore extreme care should be taken for choosing of the preparation method so that, a nanocomposite with desired properties can be obtained. Monitoring of the various features and chemical composition of the nanocomposites prepared by means of different characterization techniques is also an essential part for obtaining good quality nanocomposite with tailored properties. Present chapter describes the experimental methods and characterization techniques employed for the preparation of catalytically active metal oxide/hydroxide - graphene nanocomposite materials utilized in this Ph. D project.

2.2 Materials Used

The list of materials used for the synthesis of Metal oxide/ hydroxide – graphene nanocomposite materials are given in Table 2.1. All these chemicals were of analytical grade and employed as such without any further purification. For catalyst preparation, deionized water was used whenever water was mentioned as the solvent.

Table 2.1: List of Chemicals Used and Suppliers

Sl. No	Materials	Manufacturers/Suppliers
1	Ammonium hydroxide	MERCK specialties Pvt. Ltd
2	Cefixime trihydrate	Innova Captab Pvt. Ltd India
3	1-chloro naphthalene	Sigma Aldrich chemicals Pvt. Ltd India
4	1,4-dichloro benzene	Sigma Aldrich chemicals Pvt. Ltd India
5	Ethanol	Excise Department. Govt. of Kerala
6	Graphite	Sigma Aldrich chemicals Pvt. Ltd India
7	Glucose-D	MERCK specialties Pvt. Ltd
8	Hydrochloric acid	MERCK specialties Pvt. Ltd
9	Hydrogen peroxide	MERCK specialties Pvt. Ltd
10	Isopropyl alcohol	MERCK specialties Pvt. Ltd
11	Methanol	MERCK specialties Pvt. Ltd
12	Nikel nitrate	MERCK specialties Pvt. Ltd
13	4-nitro phenol	MERCK specialties Pvt. Ltd
14	Potassium permanganate	MERCK specialties Pvt. Ltd
15	Sodium ascorbate	MERCK specialties Pvt. Ltd
16	Sodium bisulphite	MERCK specialties Pvt. Ltd
17	Sodium borohydride	Sigma Aldrich chemicals Pvt. Ltd India
18	Sodium nitrate	MERCK specialties Pvt. Ltd
19	Sulphuric acid	MERCK specialties Pvt. Ltd
20	Triethyl silane	Sigma Aldrich chemicals Pvt. Ltd India
21	Titanium dioxide	Degussa p25
22	Urea	MERCK specialties Pvt. Ltd
23	Zinc nitrate	MERCK specialties Pvt. Ltd

2.3 Catalyst Designations

In the present investigations, 4 sets of metal oxide/hydroxide graphene catalysts containing a total of 21 catalytic systems were

prepared. The designations of various catalysts used in the present thesis are given in Table 2.2

Table 2.2: Designations Used for Different Catalysts

Sl. No	Notation	Designations
1	GO	Graphene oxide
2	rGO	Reduced graphene oxide
3	$Ni(OH)_2$	Nickel hydroxide
4	$Ni(OH)_2$/rGO	Nickel hydroxide - Reduced graphene oxide nanocomposite
5	ZnO_M	Zinc Oxide prepared via microwave irradiation
6	ZnO_H	Zinc Oxide prepared via hydrothermal method
7	G_S	Graphene prepared via liquid phase exfoliation
8	G_H	Graphene prepared via hydrothermal method
9	G_M	Graphene prepared via microwave irradiation
10	ZnO/G_S	Graphene composite with Zinc oxide via liquid exfoliation with a weight ratio of 10:1
11	H-ZnO/rGO	zinc oxide-Reduced graphene oxide composite prepared via hydrothermal method with a weight ratio of 10:1
12	M-ZnO/rGO	Reduced graphene oxide composite with zinc oxide prepared via microwave irradiation with a weight ratio of 10:1
13	HGF	Holey graphene
14	TiO_2/HGF2	Titania - Holey graphene nanocomposite with a titania to HGF weight ratio of 2:1
15	TiO_2/HGF5	Titania - Holey graphene nanocomposite with a titania to HGF with a weight ratio of 5:1
16	TiO_2/HGF10	Titania - Holey graphene nanocomposite with a titania to HGF weight ratio of 10:1
17	TiO_2/rGO	Titania-Reduced graphene oxide nanocomposite with a titania to rGO weight ratio of 5:1
18	NHG	Nitrogen doped holey graphene
19	TiO_2/NHG2	Titania – Nitrogen doped holey graphene nanocomposite with a titania to NHG weight ratio of 2:1
20	TiO_2/NHG5	Titania – Nitrogen doped holey graphene nanocomposite with a titania to NHG weight ratio of 5:1
21	TiO_2/NHG10	Titania – Nitrogen doped holey graphene nanocomposite with a titania to NHG weight ratio of 10:1

2.4 Analytical Techniques

In order to find out the nature and morphology of the catalyst as well as the active phase responsible for the catalytic process, the prepared catalytic systems were characterized using various physico-chemical characterization techniques. X-ray diffraction (XRD), Fourier Transform Infrared (FTIR) spectroscopy, Scanning electron microscopy (SEM), Transmission electron microscopy (TEM), RAMAN spectroscopy, X-Ray photoelectron Spectroscopy (XPS), CHNS analysis, UV - VIS Diffused Reflectance Spectroscopic (DRS) Analysis and Photoluminescence spectra (PL) were employed to characterize the prepared heterogeneous catalysts. The products of the catalytic reactions were confirmed using Ultraviolet-Visible Absorption Spectroscopy and Total organic carbon (TOC) analyzer. The percentage chemical composition of the products was analyzed with gas chromatograph and gas chromatography-mass spectroscopy (GC-MS). An insight to the theory and experimental details of the characterization techniques used in the present thesis work are also summarized in this section.

2.4.1 X-Ray Diffraction (XRD) Analysis

X ray diffraction (XRD) is one of the most powerful techniques used for qualitative and quantitative analysis of crystalline compounds which provides a picture of crystal structure and interplanar spacing present in the studied material. An X-ray diffractometer consists of mainly three basic components: an X-ray tube, a sample holder, and an X-ray detector. A beam of monochromatic X-rays with a wavelength

of 1.5406A strikes on a set of parallel and equidistant planes called lattice planes or Bragg's planes present in the sample crystalline material at an angle θ. A portion of the X-ray beam is scattered by the layer of atoms at the surface and its unscattered portion penetrates to the second layer of the atoms, where again a fraction is scattered and the remaining part passes on to the third layer. A diffraction pattern is formed by the constructive and destructive interferences of the reflected X-Rays

For constructive interference, Bragg obtained a formula given by,

$$n\lambda = 2d \sin \theta$$

Where λ is the wavelength of the X-radiation, n is an integer, d is the spacing between atomic planes in the crystalline planes and θ is the diffraction angle or glancing angle. This equation correlates the wavelength of electromagnetic radiation to the diffraction angle and the lattice spacing in a crystalline sample. The intensities of diffracted X-rays are measured and plotted against diffraction angle 2θ. From the 2θ values of the peaks, the lattice spacing d values can be calculated [1-3].

In this work, XRD analysis was employed as a powerful technique to characterize the synthesized catalysts. The diffraction patterns were recorded on Bruker AXS D8 advance diffractometer which used CuKα radiation (λ=1.5406 Å) and the measurements were performed in the 2θ values from 3° to 90°. For All the metal

oxide/hydroxide – graphene nanocomposite materials, the diffraction from (001) of GO and (002) plane of graphite corresponding to the 2θ values around 10° and 26.6° were analyzed.

2.4.2 Fourier Transform Infrared (FTIR) Spectroscopic Analysis

Fourier Transform Infrared Spectroscopy is the technique that provides information about the chemical bonding and the nature of functional group present in a compound. Also we can identify unknown materials, determine its quality or consistency of a sample and determine the amount of components in a mixture. The resulting vibrational spectrum obtained for the sample represents its molecular fingerprint. When an IR radiation is passed through a sample, a portion of this radiation is absorbed by the sample and some gets transmitted. Because each material contains different combinations of atoms, no two compounds produce exactly the same infrared spectrum. This makes Infrared spectroscopy an excellent tool for qualitative analysis of materials.

The FTIR instrument essentially consists of source, Michelson interferometer, sample compartment, detector and computer. The IR radiation coming from the source is absorbed by the molecule exposed to it; each absorption peak is in accordance with the characteristic bond strengths and atoms involved in bonding of the group responsible for that particular absorption [4-7].

During FTIR analysis, a parallel IR beam is directed to a beam splitter from which 50% of the radiation is reflected and goes to fixed

mirror and the other 50% get transmitted and falls on a moving mirror. Both the beams get reflected and come back to the beam splitter and recombine again. This recombination will result in the formation of an interference pattern. The interferogram obtained will contain all the information about the IR frequencies absorbed by the source. The infrared frequencies which the specimen are transmitted are translated into an IR absorption plot by Fourier transformation. The FTIR spectral pattern thus obtained is analyzed and harmonized with known signatures of recognized materials in the FTIR library. FTIR analysis is an indispensable characterization technique for materials. It requires only small quantities of sample and is non-destructive in nature.

In the present investigation all the prepared catalytic systems were analyzed by FTIR spectral technique. The FTIR spectral patterns of the catalysts were measured using Thermo Nicolet Avatar 370 spectrometer in the region of 400–4000 cm^{-1}. Its interpretation is done by correlating the peaks in the spectra of samples with that of known absorption frequencies of different types of structural moieties. All the metal oxide/hydroxide - graphene nanocomposite catalysts, FTIR spectral analysis confirmed the presence of graphene by the identification of bands corresponding to aromatic C=C stretching vibrations.

2.4.3 Scanning Electron Microscopic (SEM) Analysis

The Scanning electron microscope is a powerful and frequently used instrument to study surface topography and morphological features. By measuring the emitted electrons from the sample, SEM

produces a high resolution image of the sample. During the interaction between the beam of electrons and the sample a variety of signals can be detected including secondary electrons, backscattered electrons, photons (characteristic X-rays) and Auger electrons. The secondary electrons originating from the surface which is responsible for the topological contrast, provides information about the surface morphology. The backscattered electrons which arise from the bulk provide valuable information regarding differences in composition. Photons and characteristic X-rays are used for elemental analysis. From the SEM analysis a 3D image of the material obtained with a resolution lower than that of the TEM.

In a typical scanning electron microscope, the essential components include electron gun, electron lenses, specimen stage, detectors for all signals of interests, display/data output devices. An electron beam is thermionically emitted from an electron gun with a tungsten filament cathode. It has an energy ranging from 0.2 keV to 40 keV, which is focused by one or two condenser lenses to the spot. The focused beam is scanned across the sample by a deflection coil in the electron column. The final lens deflects the beam in the x and y axes so that it scans in a faster fashion over a rectangular area of the sample. Once the beam hits the sample, electrons and X-rays are ejected from the sample. These X-rays, backscattered electrons, and secondary electrons are collected by the detector, and convert them into a signal that is sent to a screen similar to a television which produces the final image [8-10].

The morphology and topography of the synthesized metal oxide/ hydroxide – graphene nanocomposite materials prepared in the present study were analyzed by SEM. The SEM measurements of the catalyst systems were done on JEOL model JSM -63790LV scanning electron microscope. In the graphene based nanocomposite catalysts, especially in the holey graphene composite, macro-pore structure can be easily visualized with the help of SEM images.

2.4.4 Transmission Electron Microscopic (TEM) Analysis

Transmission Electron Microscopy is a crucial technique to determine the size and shape of the nanostructured materials as well as to obtain structural information. Typically a transmission electron microscope consists of an emission source for generation of the electron beam, a vacuum system through which the electrons travel, a series of lenses (condenser lens, objective lens, projector lenses) as well as electrostatic plates. The electrons emitted by light source at the top of a microscope, travel through vacuum in the column of the microscope. The TEM uses electromagnetic lenses to focus the electrons into a very thin beam. The beam of electrons travels through the specimen which interacts with the specimen as it passes through it. Depending on the density of the specimen present, some of the electrons are scattered and disappear from the beam. The unscattered electrons hit a fluorescent screen at the bottom of the microscope, which gives rise to a shadow image of the material with its image displayed in varied darkness according to their density. The magnified images are recorded by hitting a fluorescent screen, a monitor, or on a

layer of photographic film, or to be detected by a sensor such as CCD camera. The great advantages of TEM are that it has high magnification power ranging from 50 to 10^6 and it has the ability to provide both image and diffraction information from a single sample [11, 12].

In the present study, the nature of graphene layers (mono or few layered) of catalytic systems synthesized were analyzed by TEM. JEOL/JEM 2100 transmission electron microscope was used to take the HR-TEM images of graphene and the representative metal oxide/hydroxide – graphene nanocomposite materials. TEM analysis is essential for the better understanding of graphene based nanocomposites.

2.4.5 Ultraviolet-Visible Absorption Spectroscopy

Ultraviolet-Visible spectroscopy investigates the absorption of light by molecules mainly caused by electronic excitations. This technique measure the intensity of the light in the visible and ultraviolet range passing through the sample, is referred absorbance spectroscopy or reflectance spectroscopy. The sample will absorb the light when light is passing through it or is reflected from its surface. The wavelength of that particular absorption can be recorded by the optical spectrometer. An absorption spectrum of the sample is obtained by plotting absorbance against wavelength. The intensity of absorption can be expressed as transmittance (T) defined by $T = I/I_o$ where I_o is the intensity of radiation incident on the sample and I is the intensity of the radiation rising from the sample. The wavelength at the maximum

of the absorption band will give details about the molecule or ions present in the sample and also the extent of absorption is proportional to the amount of species absorbing the light. Molecules and semiconductor materials undergo electronic transitions in this spectral range. The band gap of a semiconductor can be calculated using Kubelka-Munk plots. The quantitative measurements of the concentrations are obtained using Beer-Lambert law which gives a relation between the absorbance, the sample thickness and the concentration of the absorbing species. This relation can be expressed as $A=\varepsilon cl$, Where A= absorbance, ε = molar absorption coefficient, c = concentration of the compound in the solution and l = path length of the light in the sample. Ultraviolet-visible spectrometer or ultraviolet-visible spectrophotometer essentially consists of light source, sample holder, a diffraction grating and detector. The diffuse reflectance spectroscopic (DRS) accessory also can be attached separately for solid samples [13].

In the present investigation, UV–Vis DRS of Titania- holey graphene and Titania - Nitrogen doped holey graphene photocatalysts were performed in a Varian, Cary 5000 UV-Vis-NIR Spectrophotometer in the spectral range of 175-3300 nm. In the antibiotic degradation studies, Thermo Scientific EVOLUTION 160 UV-Visible spectrophotometer is used to calculate the amount of initial and final concentration of the antibiotic in the aqueous solutions, investigated in the range 200 nm to 800nm.

2.4.6 X-ray Photoelectron Spectroscopy (XPS)

X-Ray Photoelectron Spectroscopy (XPS) which is also known as Electron Spectroscopy for Chemical Analysis (ESCA) is widely in use for the surface chemical analysis quantitatively and qualitatively. XPS give information about the chemical state and chemical environment of elements in the sample and the empirical formula of the samples under investigation. The most important objective of XPS is the determination of elemental composition within the range of parts per thousand but under special conditions detection within a range of parts per million is also possible. XPS was developed during mid-1950's by Kai Siegbahn and his coworkers and its basic principle is photoelectric effect. It involves the irradiation of sample with X-rays and the measurement of kinetic energy of the ejected photoelectrons from top of the surface (0 nm) to 10 nm depth of a sample. XPS is a single photon in - electron out process. Due to the tiny cross section of 1s orbital, H and He elements cannot easily detect by XPS analysis and is capable of analyzing elements with atomic number 3 and above. Usually XPS uses Al Kα lines or Mg Kα lines as X-rays. During XPS analysis the atoms in the surface of sample will absorb the radiation and emit the core shell electrons when the low energy X-rays are directed towards the sample. The measurement of K.E of photoelectron provides information about binding energy (B.E) of the core electrons by the following equation derived by Ernest Rutherford (1914).

$$E_{B.E} = E_{photon} - (E_{K.E} + \varphi)$$

The B.E of each electron ($E_{B.E}$) can be measured by this equation where, E_{photon} is the energy of incident X-ray, $E_{K.E}$ is the K.E of the ejected electron, which can measured by the instrument and φ is the work function i.e. the minimum amount of energy required to eject the electrons and is characteristic of the elements present and the instrument.

A typical XPS spectrum represents a plot of intensity of ejected electrons versus B.E of ejected electrons. Each element has a characteristic XPS peak corresponding to the B.E of electrons in a particular shell. Therefore by analyzing the B.E, the identification of respective elements on the surface of a sample is possible. The number of ejected electrons with a particular B.E is directly proportional to the amount of that element in the sample. The B.E of ejected electrons not only depends on the energy of shell in which it resides but also on the chemical and physical environment around each atom. So this may cause chemical shift in the XPS spectra and gives idea about the oxidation state and chemical environment of each element. XPS is mainly used to study inorganic compounds, semiconductors, catalysts, ceramics etc. XPS can also be used to analyze the depth of analyte in multi layered materials since; the intensity of photo emitted electrons depends on depth of layers [14, 15].

XPS instrument consists of an energy analyzer for the photoelectrons and an electron detector. The analysis and detection of photoelectrons requires that the sample be placed in a high vacuum chamber. Since the photoelectron energy depends on the X-ray energy,

the excitation source must be monochromatic. The energy of the photoelectrons is analyzed by an electrostatic analyzer, and the photoelectrons are detected by an electron multiplier tube or a multichannel detector such as micro channel plate. XPS evaluates the valence states, bonding environments and the molecular composition of surface layers. Identifies elements from lithium to uranium, with detection levels down to 0.5 at %. Uses roaster scanning to produce images with a spatial resolution of 20 microns. By sputtering materials from the surface, generates composition distribution for materials. Evaluates the surface of catalysts to determine reactive species. High vacuum of order of 10^{-10} Torr reduces contamination for reliable analysis. The small spot size facilitates analysis of small areas and features.

XPS analysis offered useful information regarding the elemental composition, nature of binding between different species in the catalysts of present investigation. The XPS of $Ni(OH)_2$/rGO were done using Kratos analytical X-ray photo electron spectrometer with monochromatic Al-Kα (1486.6 eV) X-ray source (a voltage of 15 kV, a wattage of 250 W) irradiation. Various chemical environments of each element in the composite were readily discriminated by the deconvolution of XPS spectral peaks.

2.4.7 Photoluminescence Emission Spectroscopy

Photoluminescence spectroscopy is a contactless, nondestructive method of probing the electronic structure of materials. It is a process in which a substance absorbs photons (electromagnetic

radiation) and then re-radiates photons. Quantum mechanically, this can be described as an excitation to a higher energy state and then return to a lower energy state accompanied by the emission of a photon. The period between absorption and emission is typically extremely short, in the order of 10 nanoseconds. Under special circumstances, this period can be extended to minutes or hours. The intensity and spectral content of this photoluminescence is a direct measure of various important material properties. Photoluminescence in the ultraviolet-visible region comprises of two similar phenomena: fluorescence and phosphorescence.

Fluorescence occurs when a molecule in the lowest vibrational energy level of an excited electronic state returns to a lower energy electronic state by emitting a photon. Since molecules return to their ground state by the fastest mechanism, fluorescence is only observed if it is a more efficient means of relaxation than the combination of internal conversion and vibrational relaxation. Phosphorescence occurs when a molecule in the lowest vibrational energy level of an excited triplet electronic state normally relaxes to the ground state by an intersystem crossing to a singlet state or by external conversion [16, 17].

Photoluminescence spectrometer consists of a light source, excitation monochromator, emission monochromator, sample holder and a detector. An excitation wavelength is selected by first monochromator (for excitation), and luminescence is observed through a second monochromator (for emission), usually positioned at 90° to the incident light to minimize the intensity of scattered light reaching

the detector. If the excitation wavelength is fixed and the emitted radiation is scanned, an emission spectrum is produced. The essentials of a luminescence experiment is that the sample is irradiated at one wavelength and emission is observed over a range of wavelengths. The excitation monochromator selects the excitation wavelength and the emission monochromator selects one wavelength at a time to observe.

In the present study, photoluminescence spectra is used for the investigation of emission properties of the samples. PL spectra of TiO_2/HGF TiO_2/NHG TiO_2/rGO and bare TiO_2 were recorded using a Perkin Elmer Model LS 55 spectrofluorimeter with an excitation wavelength of 320 nm.

2.4.8 Raman Spectroscopy

Raman spectroscopy is a powerful tool to analyze structural/morphological properties of solid at a local level, given the strong sensitivity of the phonon characteristics to the crystalline nature of the materials. Raman spectroscopy can readily probe a sample of any form (solid, liquid or gas) by measuring the wavelength and intensity of the scattered monochromatic light. It is a vibrational spectroscopic technique and it differs from the infrared spectroscopy being a technique which involves an indirect coupling of high frequency radiation (such as visible light) with vibrations of chemical bonds. Raman spectrum is very sensitive to the length, strength, and arrangement of chemical bonds in a material. When the incident photon interacts, the molecules are excited to higher virtual energy states. Most of the energy would be reradiated at the Rayleigh

scattering. A small portion of energy is transferred which results in exciting the vibrating modes, and scattered radiations in this Raman process are called stokes and antistokes radiations. If the subsequent reradiation has a frequency lower (a smaller wavenumber) than that of the incident exciting light, it is the stokes radiation. The vibrational energy is deducted by measuring the difference between the frequency of the Raman line and the Rayleigh line. Existing vibrations, e.g. through thermal activation, can also couple with and add their energies to the incident beam, which is called antistokes scattering. The resulting Raman line appear at higher frequencies or larger wavenumbers. Stoke and antistokes scattering spectra are mirror images on opposite side of the Rayleigh line. However stokes scattering spectra are mostly used, since they are less temperature sensitive. Raman effect is extremely weak and thus, intense monochromatic continuous gas lasers are used as the exciting light. The energy range of Raman analysis is the order of 200 to 4000 cm^{-1} [18-20].

In a typical Raman spectrometer, a laser is used to excite the sample in Laser Raman Spectrometers which gives sufficient intensity to produce a useful amount of Raman scattering and allows for clean spectra, free of extraneous bands. Lasers used in Raman spectroscopy must exhibit good wavelength stability and low background emission. The probe is a collection device that collects the scattered photons, filters out the Rayleigh scattered radiations and any background signal from the fibre optic cables, and sends the Raman scattered radiations to

the spectrograph. Many probes also focus and deliver the incident laser beam.

When Raman scattered photons enter the spectrograph, they are passed through a transmission grating to separate them by wavelength and passed to a detector, which records the intensity of the Raman signal at each wavelength. This data is plotted as the Raman spectrum.

In the present investigation, Raman spectral analysis is used for better understanding of the quality and nature of graphene prepared by the liquid phase exfoliation of graphite. Raman analysis was done with a Thermofischer Scientific, Laser Raman spectroscopy with 532nm. Raman analysis provide better information about the number and defects of layers in graphene. Raman spectra of graphene are characterized by three important bands. They are D, G and 2D bands. Frequencies and intensities of each of these bands provide valuable information. The intensity of the D band is indicative of the presence of defects in the graphene layers. From the position of 2D band, the number of stacked layers in the sample can be determined and the shift of 2D band towards lower wavenumbers indicates the presence of graphene monolayers.

2.4.9 Total Organic Carbon (TOC) Analysis

Total Organic Carbon (TOC) measurement is commonly used for determining the degree of organic contamination in water. It is a non-specific test, which means TOC will not give you which particular compounds are present as contaminants (most samples are complex

mixtures which contain thousands of different organic carbon compounds). Instead, TOC will inform the sum of all organic carbon within those compounds. From TOC analysis, we can measure total carbon (TC), inorganic carbon (IC), total organic carbon (TOC), purgeable organic carbon (POC) and non-purgeable organic carbon (NPOC). TOC analysis involves three steps which are sampling, oxidation and detection. To meet the required regulations, it is recommended that the sampling system have automatic sampling, acidification, and sparging for TOC analysis, automatic dilution capability and autocalibration using a single stock standard in order to improve reproducibility and increase throughput. To determine the level of TOC, the organic carbons must be oxidized. There are several types of oxidation methods. These methods, which convert TC into CO_2, include:

1) Photocatalytic oxidation: Organics are converted to carbon dioxide in the presence of UV light and photocatalyst.

2) Chemical oxidation: sample is mixed with Persulfate in a UV-irradiated chamber to convert organics to carbon dioxide.

3) High-temperature combustion: sample is mixed with oxidation catalyst in a chamber heated to 95-100 ^{o}C to convert organics to carbon dioxide.

TOC Analysers have three types of detection systems. Non-dispersive infrared (NDIR), Direct conductometric detectors (Non selective conductometric) and membrane conductometric detectors (Selective conductometric). NDIRs, which consist of a light source, cell and a detection portion. It takes a preliminary reading to determine

a baseline. When the sample enters the NDIR cell, CO_2 molecules absorb the infrared light coming from the source, reducing the total transmittance of infrared light that reaches the detector. After CO_2 has been removed from the cell, the percentage transmittance returns to 100% [21, 22].

In conductometric TOC detectors, CO_2 is measured in the liquid phase. The two conductometric type detectors are direct conductometric and membrane or selective conductometric ones. Both the two conductometric type detectors have stable calibration and high sensitivity. The primary difference between these two conductometric detectors is that the direct detector is susceptible to interference from ionic contamination such as acids, bases and halogenated organics. In the membrane – based conductometric detectors, the membrane is a protective barrier to interfering ions, enabling the analysis of CO_2 only. This will result in a more accurate TOC reading.

In the present study, TOC analysis was used for better understanding of the Total Organic Carbon content in the water after the photocatalytic antibiotic degradation. TOC analysis was done with TOC-L Shimadzu TOC analyser which utilizes 680°C combustion catalytic oxidation method.

2.4.10 CHNS Analysis

CHNS analysis provide rapid determination of carbon, hydrogen, nitrogen and sulphur in organic matrices and other types of materials. The technique is capable of handling a wide variety of sample types, including solids, liquids, volatile and viscous samples, in the fields of pharmaceuticals, polymers, chemicals, environment, food

and energy. CHNS analysis gives evidence about the structure of an unknown compound as well as its purity. The inventor of elemental analysis was Antoine Lavoisier, who first used the principle of gravimetric estimation of adsorbed gases on the sample as a quantitative measurement to determine the composition of elements in the sample. CHNS analysis in its simplest form, as it is done nowadays, requires high temperature combustion in an oxygen-rich environment and is based on the classical Pregl-Dumas method. This combustion can be carried out under both static conditions i.e. by the introduction of a set volume of oxygen as well as by dynamic conditions i.e. a constant flow of oxygen for a set period of time. Often, catalysts are also added to the combustion tube in order to aid the conversion. It can also be termed as combustion analysis since, in the combustion process (furnace at ca. 1000 □), sample in the presence of excess oxygen get converted to the oxidized products i.e., carbon to carbon dioxide; hydrogen to water; nitrogen to nitrogen gas/ oxides of nitrogen and sulphur to sulphur dioxide. The determination of masses of these combustion products yields an idea about the composition of elements in the sample.

In the CHNS instrument, a measured amount of sample (usually 2 to 3 mg) is taken (for solids or viscous liquids, samples are weighed out into tin capsules; for liquids, samples can be sealed in individual aluminum vials) and is combusted in a reactor at a temperature of 1000 °C with the passage of excess of oxygen. At this temperature the sample and the tin container will melt and undergo decomposition and rapid combustion with the formation of oxidized

products. Formation of CO is also possible due to partial oxidation. Then the carrier gas will carry these combustion products towards a silica tube packed with an oxidation catalyst, such as tungsten trioxide (WO_3), where complete oxidation will occur. The reduction catalyst copper is kept at 1000 °C and it will reduce NO_2 to N_2. The leaving gas stream from the column enriched with CO_2, H_2O, N_2 and SO_2 will then direct towards a gas chromatograph where quantitative measurement of these gases will occur and produces a staircase type signal. In the signal, the step height corresponds to the amount of element in the sample. Calibration is carried out by the elemental analysis of standard samples [23, 24].

In the present study CHNS analysis was employed for the determination of percentage of C, H and N in the NHG sample and was done on the CHNS analyzer of model Elementar Vario EL III.

2.4.11 Gas Chromatography

Chromatography is a technique for separating chemical substances that mainly relies on differences in partitioning or adsorption behavior between a flowing mobile phase and a stationary phase which separate the components in a mixture. The important chromatographic methods are gas chromatography (GC) and liquid chromatography (LC, often termed as high-performance liquid chromatography (HPLC)). In GC, based on the difference in polarity, boiling point and the structure of the individual compounds the mixture is separated. The sample is dissolved in low concentrated organic solvent and then injected into the gas chromatograph for carrying out

the GC analysis. To obtain a useful gas chromatogram, in some cases the sample has to be derivatized with specific reagents. The main reason for the derivatization is to make the sample volatile. After injection of the volatile sample into the gas chromatograph, it is carried through the column by a carrier gas (Carrier gases for chromatograms must be of high purity and chemically inert towards the sample eg: He, Ar, N_2, CO_2 and H_2). The carrier gas system may contain a molecular sieve to remove water or other impurities. A column is a long, thin path (usually capillary tube) that contains a material with which the sample components interact more or less strongly depending on their structure (may be polarity). The separated components reach the detector. One of the common detectors, i.e. flame ionization detector, is used in the present studies. When the detector detects a material eluted from the column at a certain retention time, it will be shown as a peak in the chromatogram. Generally, the integrated area of the peak over time is proportional to the amount of material. This constitutes the usefulness of GC in quantifying the amounts of components in a mixture. Often standards are used in GC, which are known compounds that will indicate the presence of those compounds in the mixture based on their retention time in the column. Standards are therefore very useful in establishing the presence of specific compounds in a mixture [25-29].

In the present study, benzene was analyzed using Thermo Fisher Trace GC 700 Gas Chromatograph equipped with a flame ionization detector as per the standard procedure. The gas chromatograph (Shimadzu Gas Chromatograph GC-2010 PLUS)

equipped with a molecular sieve column and a TCD detector was used for the hydrogen production experiments.

2.4.12 Gas Chromatography-Mass Spectrometry

The percentage formation of dechlorinated products present were evaluated by gas chromatography–mass spectrometry (GC-MS). It is an analytical method that combines the features of gas chromatography and mass spectrometry to identify different substances within a test sample. In the GC-MS instrument, chemical mixtures are separated in the GC component and the components at the molecular level are identified in the MS component. It is one of the most accurate tools for analyzing organic samples. In the GC-MS, mixture will separate into individual substances in the GC and whatever is emerged from the column opening will flow into the MS. MS identifies the compounds by determining the mass of the analyte molecule and then by comparing it with the standard mass spectral library of known mass spectra of known compounds, covering several thousand compounds. MS is considered as the only definitive analytical detector in GC [30-33].

In the present study the dechlorinated product tetralin and naphthalene were analyzed using Thermo scientific Trace GC 1300 equipped with Mass ISQLTC, Single Quadrupole Mass Spectrometer.

2.5 General Description of Methods Adapted for the Preparation of Different types of Metal Oxide / Hydroxide - Graphene Nanocomposite Materials

Graphene for the graphene nanocomposite materials was prepared from the precursor graphite via two different methods. One

was via graphite oxide prepared by modified Hummers method and the other one was graphene prepared by liquid phase exfoliation using mixture of isopropyl alcohol and water as solvents. The outline of the different preparation methods adapted for the present study is provided in this section.

2.5.1. Preparation of Nickel hydroxide/Graphene Nanocomposite

2.5.1.1. Preparation of Graphene Oxide

The modified Hummer's method was used for the preparation of graphite oxide. Here, flake graphite was subjected to oxidative treatment. 2 g of flake graphite was reacted with 96 ml of concentrated H_2SO_4 and 1g of $NaNO_3$ in a 500 ml beaker kept in an ice bath. While stirring the mixture, 6 g of $KMnO_4$ was added slowly with vigorous stirring and the temperature was maintained below 20 ^oC. The ice bath was removed and the temperature was brought up to 35 ^oC. The stirring continued for 18 hours. As the reaction extended, the mixture turned out to be pasty with a brown colour. Successively, 150 ml of water was moderately added to the paste. Addition of water to a concentrated H_2SO_4 medium raised the temperature. The mixture was diluted to 240 ml with water; 5 ml of 30% of H_2O_2 was added. Then suspension so obtained was stirred continuously for 2 h and filtered to obtain a yellow – brown paste. It was then washed with 10% HCI, deionized water and ethanol. Then it was dried at 60 ^oC to get Graphite oxide. This Graphite oxide readily forms a stable colloidal suspension in water upon ultrasonication for 30 min and stable dispersion of graphene oxide (GO) in water was obtained.

2.5.1.2. Preparation of Nickel Hydroxide / Graphene Nanocomposite

Graphene oxide (GO) was prepared by the method in 2.5.1.1. To the GO solution (400 ml), nickel nitrate powder (0.02 mol) and urea (0.2 mol) were added. The mixture was stirred for 1 h. Then 3 g $NaHSO_3$ was added stirred for 5 min and was kept in an autoclave maintained at 180 ^oC for 6 h. After cooling, the composite was filtered, washed with distilled water, ethanol and then dried at 60 ^oC to get $Ni(OH)_2$/rGO nanocomposite. $Ni(OH)_2$ and rGO were prepared in the same way without $Ni(NO_3)_2$ and GO respectively.

2.5.2. Preparation of Zinc Oxide/Graphene Nanocomposite

2.5.2.1 Preparation of ZnO Via Hydrothermal Method (ZnO_H)

Pure ZnO was prepared by hydrothermal reaction. In the typical reaction, 2.7402 g of Zn $(NO_3)_2$ was dispersed in 150 ml distilled water. Then, required amount of ammonium hydroxide (NH_4OH) was added to adjust the mixture to a pH value of 12, followed by ultrasonication for half an hour. The reaction was continued in a Teflon-lined stainless steel autoclave and heated for 16h at 120 ^oC. Then obtained ZnO nanostructures were filtered, washed and dried in a hot air oven at 70 ^oC for 4 h, resulting in the formation of ZnO.

2.5.2.2 Synthesis of ZnO/ Graphene Nanocomposite Via Hydrothermal Method (H-ZnO/rGO)

Graphite oxide was synthesized following the procedure in 2.5.1.1.This Graphite oxide (75 mg) readily formed a stable colloidal

suspension in 150 ml water upon ultrasonication for 30 min and stable dispersion of graphene oxide (GO) in water was obtained. The dispersion was brown in colour. 0.75 g of as prepared ZnO was added to this dispersion and stirred for 1 h. 0.3 g glucose was added into the above mentioned solution under ultrasonication for 30 min. Then the solution was transferred into Teflon-lined stainless steel autoclave and heated for 16 h at 120 ^{o}C. The ZnO/graphene nanocomposites were filtered, washed and dried in a hot air oven at 70 ^{o}C for 4 h, resulting to the formation of ZnO/graphene nanocomposite. Bare ZnO and graphene (G_H) were also prepared.

2.5.2.3 Preparation of ZnO Via Microwave Method (ZnO_M)

Pure ZnO was synthesized by microwave irradiation method. In a typical experiment, 2.7402g of $Zn(NO_3)_2$ was dispersed in 150 ml distilled water. Then, required amount of ammonium hydroxide (NH_4OH) solution was added to adjust the mixture to a pH value of 12, followed by ultrasonication for 30 min. Then the solution was subjected in to an automated focused household microwave synthesis system and treated for 10 min at 700 W. Then the obtained product was filtered, washed and dried in a hot air oven at 70 ^{o}C for 4 h, resulting to the formation of ZnO.

2.5.2.4 Preparation of ZnO/Graphene Nanocomposite (M-ZnO/rGO)

Graphite oxide was synthesized as per the procedure described in 2.5.1.1. A stable colloidal suspension of this graphite oxide (75 mg)

was formed in 150 ml water upon ultrasonication for 30 min and stable dispersion of graphene oxide (GO) in water was obtained. The dispersion was brown in colour and then added 2.7402g Zn $(NO_3)_2$. Ammonium hydroxide (NH_4OH) solution was added to adjust the mixture to a pH value of 12 and 0.3 g glucose was added into the above mentioned solution under ultrasonication for 30 min. It was then subjected to microwave irradiation using an automated focused household microwave synthesis system for 10 min at 700 W. It was observed that the colour of suspension had changed from brown into black, indicating the successful chemical reduction of GO. The as-synthesized product was washed thoroughly with the distilled water and centrifuged at 3000 rpm for 20 min to remove the residue. The obtained final product was dried in a hot air oven at 70 °C for 4 h, resulting to the formation of ZnO/graphene nanocomposite. Bare ZnO and graphene (G_M) were also prepared.

2.5.2.5 Synthesis of ZnO/ Graphene Nanocomposite Via Liquid Phase Exfoliation Method (ZnO/G_S)

2.5.2.6 Preparation of Graphene (G_S)

Graphite flakes were subjected to the one-step, greener liquid-phase exfoliation method to synthesize graphene. 0.05g graphite flakes were added in to a mixture of isopropyl alcohol and deionized (DI) water (in the ratio 2 to 3) and ultrasonicated for 3h.The mixture was then centrifuged and washed with DI water twice. The sediment was dried at 80°C overnight and the graphene was collected. The as-synthesized graphene (50 mg) was re-dispersed in to isopropyl alcohol

via ultrasonication. Pure ZnO was synthesized by the method described in 2.5.2.3 for the nanocomposite.

2.5.2.7 Preparation of ZnO/Graphene Nanocomposite (ZnO/G_S)

In a typical experiment, 2.7402 g of $Zn(NO_3)_2$ was dispersed in 150 ml distilled water. Then, required amount of ammonium hydroxide (NH_4OH) solution was added to adjust the mixture to a pH value of 12, followed by ultrasonication for 30 min. Then the solution was subjected into an automated focused household microwave synthesis system and treated for 10 min at 700 W. Finally, the ZnO formed was filtered, washed and dried in a hot air oven at 70 ^oC for 4 h, resulting in the formation of ZnO powder. 0.5 g of this ZnO was dispersed again in isopropyl alcohol via ultrasonication. The graphene dispersion was then added into the zinc oxide dispersion which is further ultrasonicated to achieve an even mixing. Next, the mixture was centrifuged and nanocomposite residue obtained was washed with ethanol and DI water twice. The ZnO/graphene nanocomposite was dried at 70 ^oC.

2.5.3. Synthesis of TiO_2/HGF Nanocomposites

2.5.3.1 Synthesis of Holey Graphene

Graphene oxide (GO) was prepared by modified Hummers method described in the section 2.5.1.1. 10 ml of diluted hydrogen peroxide aqueous solution (0.3% H_2O_2) was added in to 200 ml of GO aqueous dispersion in Teflon lined autoclave. The mixture was sealed, heated at 180 ^oC for 6 h and naturally cooled down to room

temperature and the as prepared HGF was immersed in 0.05 M sodium ascorbate solution at 100 ^{o}C for 2 h. The HGF was lastly immersed in pure water to remove any impurities if present. It was washed well with distilled water, filtered and dried. rGO was prepared following the same procedure without adding any H_2O_2.

2.5.3.2 Synthesis of TiO_2/HGF Nanocomposite

Commercial Degussa p25 TiO_2 was used for the nanocomposite preparation. 0.1g HGF and 1.9g commercial Degussa p25 TiO_2 were mechanically mixed in an agate mortar for 1h. Then it was calcined at 250 ^{o}C for 3 h to get TiO_2/HGF nanocomposite. TiO_2 nanocomposites of rGO was also prepared in a similar way for comparison purpose.

2.5.4 Synthesis of TiO_2/NHG Nanocomposite

2.5.4.1 Synthesis of NHG Nanocomposites

The holey graphene was prepared as described in 2.5.3.1. 10 ml of HGF aqueous dispersion was diluted with 25 ml of DI water and 2 g of urea was added and ultrasonicated for 1h. The solution was sealed in a Teflon lined autoclave and maintained at 180 ^{o}C for 18 h. The resulting nitrogen doped holey graphene obtained was filtered and washed with DI water for several times and dried.

2.5.4.2 Preparation of NHG/TiO_2 Nanocomposite

Here also, Degussa p25 TiO_2 was used for the nanocomposite preparation. 0.1g NHG and 1.9g commercial Degussa p25 TiO_2 were

mechanically mixed in the agate mortar for 1h. Then it was calcined at 250 ^{o}C for 3 h to get TiO_2/NHG nanocomposite.

2.6 Procedure of Methods Adapted for The Catalytic Studies Done by the Metal Oxide/Hydroxide - Graphene Nanocomposite Materials

2.6.1 Dechlorination of Aryl Chlorides with Triethylsilane (TES)

For the reductive dechlorination of chloronaphthalene, 0.3 g of $Ni(OH)_2$/rGO catalyst and 10mmol TES (1.5 ml) were taken in an RB flask. To this, 0.3 mmol chloronaphthalene (except for the studies of optimisation of initial concentration) was added and the mixture was refluxed for 3h. The products were then extracted with acetonitrile and analysed using GC-MS measurements were performed for the product analysis.

The catalytic dechlorination of the dichlorobenzene was also carried out using a similar procedure except that the initial dichlorobenzene concentration taken was 0.6mmol (0.0886g) and GC measurements (Thermo scientific Trace GC 700 equipped with FID detector) was carried out. The peak positions were obtained by injecting standard compounds and percentage composition was calculated from the integrated area of each peak.

2.6.2 Reduction of p-Nitrophenol

For the reduction of p-nitrophenol, $NaBH_4$ was used as the reducing agent. In the typical catalytic test, 115 μL of 2.696 mM aqueous dispersion of the catalyst was added to 1 mL of 0.5 mM p-nitrophenol aqueous solution (the molar mass of the catalyst is 0.62 % of the substrate p-nitrophenol, the relative molecular weight of

nickel hydroxide was counted as 92.714 without water molecule). Then a 3.5 mL $NaBH_4$ aqueous solution (22.6578 mM) was added to begin the reaction. UV-Vis spectroscopy (Thermo Scientific EVOLUTION 160 UV-Visible spectrophotometer) in the wavelength range 400 to 800 was used to monitor the reaction mixture in every 2 min.

2.6.3 Photocatalytic Antibiotic Degradation Studies

All experiments of photocatalytic degradation were carried out in natural sunlight. A Thermo Scientific EVOLUTION160 spectrophotometer in the wavelength range 200 to 800 nm was used to measure absorbance of solutions.

For photocatalytic degradation studies, 100 ml of aqueous solution of required concentration of cefixime and 0.05g of TiO_2/NHG photocatalyst (except for catalyst weight optimization studies) were taken in a beaker, stirred for 30 minutes in darkness and subsequently exposed to sunlight for about 90 minutes with constant stirring. After a specific time interval, 5 ml of the solution was withdrawn and centrifuged for 30 min at 3500 rpm and its absorbance was observed by measuring λmax of cefixime at 287.5 nm using UV-Vis spectrophotometer. The decrease in concentration of the antibiotic due to photodegradation can be measured in this way. All the experiments were carried out on sunny days in hours when sunlight availability was maximum.

The efficiency of degradation of cefixime was calculated using the formula:

$$E\ (\%) = (C_0 - C) / C_0 \times 100 \ldots (1),$$

Where C_0 represents the concentration of cefixime at zero irradiation time and C is its concentration at an irradiation time t. E (%) is the efficiency of degradation of cefixime over the TiO_2/NHG.

2.6.3.1 Accumulated Light Energy Calculations

Instantaneous Intensity of sunlight was measured in every five minutes interval of irradiation using the application LUX METER installed on an android mobile platform and conversion to accumulated light energy was carried out as per the Table 2.3 given below.

Table 2.3: Accumulated Light Energy Calculations Carried Out Ffor During the Study on the Effect of Initial Cefixime Concentration on the Photocatalytic Performance.

Irradiation Time(min)	In hours	Light intensity (Lux)	Integrated area of intensity× time graph (A)	Wh/m^2 (A*0.0094444)	Wh (* exposed area of reaction mixture)	kWh
0	0	261000	61556.5	581.36	642.56558	0.64
5	0.083	261000				
10	0.167	261000				
15	0.250	172000				
20	0.333	172000	111757	1055.4778	1166.5985	1.17
25	0.417	214000				
30	0.500	261000				
35	0.583	172000	167708	1583.9014	1750.6545	1.75
40	0.667	261000				
45	0.750	216000				
50	0.833	161000	216865	2048.1598	2263.7901	2.26
55	0.917	214000				
60	1	214000				
65	1.083	261000	316042.5	2984.8318	3299.0749	3.30
70	1.167	172000				
75	1.250	162000				
80	1.333	209000				
85	1.417	172000				
90	1.5	214000				

2.6.4 Photocatalytic Water Splitting Studies

The reaction was carried out in a fabricated 316 stainless steel reactor with a sapphire window through which light can be passed in to the chamber having an outlet closed with septum through which the gaseous products formed can be taken out. Methanol was used as the sacrificial reagent. Typically, 250 mg of the material was suspended in 50 mL solution containing H_2O and methanol in 4:1 ratio, except for the studies on the effect of the amount of sacrificial agent. The suspension was degassed for 30 min with high-purity nitrogen prior to irradiation. The solution was continuously stirred using magnetic stirrer for uniform dispersion of the photocatalyst. For illumination, a light source of 400W high pressure mercury lamp was used. H_2 evolution was monitored by recording the gas chromatogram for every one hour interval. The experiment was continued for a total of 5 hours. The carrier gas used was argon. The gas chromatograph (Shimadzu Gas Chromatograph GC-2010 PLUS) equipped with a molecular sieve column and a TCD detector was used for the purpose.

References

1. M. Birkholz, *Thin film analysis by X-ray scattering,* WILEY-VCH Verlag GmbH & Co. KGaA, Weinheim, 2006.
2. C. Whiston, *X-ray Methods-Analytical Chemistry by Open Learning,* John Wiley & Sons, New York, 1987.
3. H. Lipson, H. Steeple, *Interpretation of X-ray powder diffraction patterns*, Macmillan, London, 1970.
4. R. M. Silverstein, G. C. Bassler and T. C. Morrill, *Spectrometric Identification of Organic Compounds,* Wiley, New York, 1981.
5. B. H. Stuart, *Infrared Spectroscopy: Fundamentals and Applications,* Wiley, Chichester, United Kingdom, 2004.
6. P. R. Griffiths and J. A. de Haseth, *Fourier Transform Infrared Spectroscopy,* John Wiley & Sons, New York, 1986.
7. J. Connes and P. Connes, *J. Opt. Soc. Am.,* 1966, **56**, 896-910.
8. A. Howie, Characterisation of Catalysts, ed. J. Thomas and R. M. Lambert, John Wiley, New York, 1989.
9. F. Liu, J. Wu, K. Chen and D. Xue, *Microscopy: Science, Technology,Applications and Education*, ed. A. M. Vilas and J. Diaz, Formatex Research Center, 2010, **3**, 1781-1792.
10. W. Zhou, R. Apkarian, Z.L. Wang and D. Joy, *Scanning Microscopy for Nanotechnology-Techniques and applications,* ed. W. Zhou and Z.L. Wang, Springer Science Business Media, LLC, NY, USA, 2006, 1-21.
11. D. B. Williams, C. B. Carter, *The Transmission Electron Microscope*, Springer, Boston, MA, 1996.
12. A. Muller and J. Grazul, *J. Electron Microsc.,* 2001, **50**, 219-226.
13. L. D. S. Yadav, *Organic Spectroscopy*, ed. L. D. S. Yadav, Springer, Dordrecht, 2005, ch.2, 7-51.
14. P. V. Heide, *X-Ray Photoelectron Spectroscopy,* John Wiley & Sons, Inc, New York, 2011.
15. J. Azoulay, *Vaccum*., 1983, **33**, 211-213.
16. C. Ronda, *Luminescence from Theory to Applications*, Wiley-VCH, New York, 2008.

17. P. Goldberg, *Luminescence of Inorganic Solids*, Academy Press, New York, 1966.

18. C. V. Raman and K. S. Krishnan, *Nature*., 1928, **121**, 501-502.

19. C. V. Raman, *Indian J. Phys.,* 1928, **2**, 399-419.

20. N. Ahlawat, *IJCSMC*, 2014, **3**, 680-685.

21. I. Bisutti, I. Hilke, M. Raessler, *Trends Analyt Chem.,* 2004, **23**, 716-726.

22. Y. S. Fung, Z. Wu, and K. L. Dao, *Anal. Chem.,* 1996, **68**, 2186-2190,

23. V. P. Fadeeva, V. D. Tikhova and O. N. Nikulicheva, *J Anal. Chem.*, 2008, **63**, 1094-1106.

24. E. I. Braun, P. Pantano,*Carbon.,* 2014, **77**, 912-919.

25. F. A. Settle, *Handbook of Instrumental Techniques for Analytical Chemistry*,Prentice Hall PTR, Upper Saddle River, New Jersey, 1997.

26. C. M. Marvin, *GC/MS A practical user's guide*, John Wiley & Sons, Inc, USA, 2008.

27. B. Jonathan and M. M. James, *Analytical chemistry in a GMP environment*, John Wiley & Sons, Inc., USA, 2000.

28. R. L. Grob, *Modern Practice of Gas Chromatography*, Wiley, New York, 1995.

29. W. Harris and H. Habgood, *Programmed Temperature Gas Chromatography*, J. Wiley & Sons, New York, 1966.

30. H. J. Hubschmann, *Handbook of GC-MS: Fundamentals and Applications,* Wiley-VCH, Weinheim, 2009.

31. S. Ahuja and N. D. Jespersen, *Modern Instrumental Analysis,* Elsevier, Amsterdam, 2006.

32. O. D. Sparkman, Z. Penton and F. G. Kitson, *Gas Chromatography and Mass Spectrometry: A Practical Guide,* Academic Press, Oxford, 2011.

33. S. Sharmila and L. J. Rebecca*, J. Chem. Pharm. Res.,* 2012, **4**, 4883-4887.

Chapter 3

Nickel Hydroxide Platelets /Reduced Graphene Oxide ($Ni(OH)_2$/rGO) Nanocomposite and its Catalytic Applications

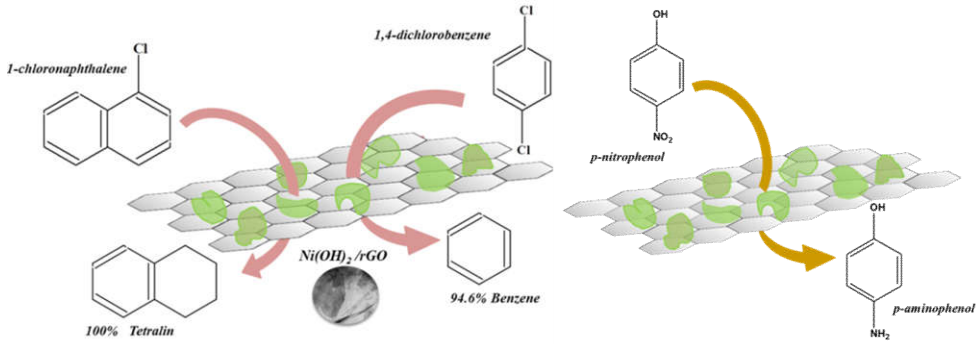

3.1 Introduction

Graphene forms a versatile two-dimensional material with a variety of applications due to its unique properties [1-6]. Along with single layer graphene, few layer graphene with layers up to 10 also show exceptional properties and a subject of increasing interest [7]. The most common strategy in the bulk scale production of graphene is the oxidation of graphite in harsh conditions and the subsequent exfoliation of the graphite oxide formed followed by its reduction to reduced graphene oxide (rGO) [8, 9]. The chemical oxidation of graphite introduces many oxygen-containing functionalities such as epoxides, alcohols and carboxylates in the graphene sheet [10, 11]. As a result, graphite oxide and exfoliated graphene oxide are moderately acidic and behaves as a powerful oxidant which makes it a potential candidate for catalytic applications. Furthermore, impregnation of transition metals or other catalytically active substances to graphene-based materials having relatively high surface area can provide additional advantages with regard to the catalytic performance [12-14].

In a heterogeneous catalyst, the nature, concentration and accessibility of the active reaction sites that are capable of chemisorbing the reactants and can form surface intermediates which determine the performance of the catalytic system. Graphene derivatives, such as graphene oxide (GO) and reduced graphene oxide (rGO) offer a wide range of possibilities to synthesize metal oxide/hydroxide-graphene nanocomposite materials in which the graphene sheet functions either as supports for immobilizing active catalytic species on the surface or as metal free catalysts. The use of

these nanocomposite materials in organic synthesis as alternative heterogeneous reusable systems for various selective transformations of simple and complex molecules are now increasing rapidly [15]. Graphene nanocomposite materials are among the leading next generation functional materials because of a variety of potential applications [12-14, 16-29]. $Ni(OH)_2$ nanocrystals grow on graphene with various degrees of oxidation including lightly oxidized, highly conducting graphene [30]. The morphology, size, and crystallinity of the nanocrystals can be tuned by the surface chemistry of the underlying graphene substrates. A general method of their preparation involves the distribution of catalytically active materials on top of graphene sheets employing various strategies to achieve improved performance. There are several reports on the use of $Ni(OH)_2$/rGO nanocomposites in various applications including energy storage [21-23], electrocatalytic conversions[24] and catalytic reactions[12-14,25], especially the hydrogenation of nitrobenzene[25] and reduction of p-nitrophenol [12-14]. These nanocomposites exhibit enhanced activities from that of the component materials.

Polychlorinated aromatic hydrocarbons are ubiquitous contaminants in air, water, sediments and soil due to their excessive use for various purposes [31-34]. They are chemically stable their bioaccumulation causes a threat to all living organisms [35, 36]. Because of their xenobiotic nature, organochlorine contaminants do not get naturally deteriorated in the environment and this increases the gravity of the problem [37]. The commonly adopted method of remediation of solid wastes containing organochlorines is incineration, which causes

the production dioxin [38]. Reductive dechlorination, on the other hand, does not result in any dioxin release. Thus, the catalytic, reductive dechlorination has been widely accepted as one of the most suitable methods for the removal of organochlorine contaminants, because of its simplicity, effectiveness and safety [39]. Generally, transition metals or their compounds are used as heterogeneous catalysts [37, 40-44]. Dechlorination involves the breaking of carbon-chlorine bond, which can be speeded up by a catalyst, resulting in the formation of comparatively safer hydrocarbon products [40, 45, 46]. The dechlorination of aromatic systems is far more difficult in comparison with the aliphatic ones [46, 47]. Previous studies by Muradyan et al. reported dechlorination of polychlorinated aromatic hydrocarbons with a maximum of 75 % conversion for a period of 3h using colloidal nickel catalysts along with graphite oxide, employing organosilanes as the hydrogen source [48].

Nitrophenols are considered to be amongst the most prevalent organic pollutants, often present in industrial effluents and agricultural waste water. It possess some major adverse effects such as it could cause adverse changes in the blood, liver and central nervous system, and it could transform hemoglobin into methemoglobin, causing serious hypoxia. The US Environmental Protection Agency has reported nitrophenols as very hazardous and harmful environmental pollutant even at low concentrations.Therefore, the hydrogenation of nitrophenol is not only important in an academic point of view, but also benefits the chemical industry and environment [49-51]. Thus, the development of an effective and ecofriendly method to remove

nitrophenols from water is of great importance in which, selective hydrogenation is a simple, fast and can be considered as an effective measure for the conversion of nitrophenol to more green products such as aminophenol. Aminophenol is very useful chemical and essential in many industrial applications. It is an important intermediate used for the synthesis of a variety of analgesic and antipyretic drugs such as paracetamol, acetanilide and phenacetin. It is also used as a photographic developer, corrosion inhibitor and even as a hair-dyeing agent [49-51].

Herein, we present a green, simple, low-cost, scalable hydrothermal approach for the synthesis of $Ni(OH)_2$/rGO nanocomposite by direct reaction between rGO and nickel nitrate. During the hydrothermal process, nickel nitrate was directly converted into $Ni(OH)_2$. In the present work, we demonstrated the complete dechlorination of 1,4-dichlorobenzene to benzene and 1-chloronaphthalene to tetralin using exfoliated $Ni(OH)_2$ platelets anchored on reduced graphene oxide catalyst within a period of 3h. $Ni(OH)_2$/rGO composite was also used for the catalytic reduction of 4-nitrophenol to p-aminophenol in the presence of $NaBH_4$. The reduced graphene oxide is capable of working as a better catalytic support because of the high electron richness of graphene which can substantially facilitate reduction reactions.

Quantitative analyses of the final products were carried out using gas chromatography for reaction with DCB using suitable standards. The dechlorination of 1-chloronaphthalene [52-54] was studied

in detail with which the optimisation of various key parameters of the reaction such as the weight of the catalyst loaded, initial reactant concentration, and reaction time.

Very recently, Jia et al. have studied in detail the dependence of the catalytic activity of $Ni(OH)_2$ on the interlayer spacing of the catalyst and they have observed that the highest catalytic performance was shown by $Ni(OH)_2$ catalyst with highest interlayer spacing [55]. According to them when the interlayer spacing is high, various anions and gases masking reaction sites escape and as a consequence the catalyst efficiency get improved substantially. A similar effect was observed in our studies also. We could observe a substantial enhancement in catalytic performance for the catalyst with exfoliated $Ni(OH)_2$ platelets anchored on reduced graphene oxide compared to bare $Ni(OH)_2$ with a layered morphology containing many intercalated species. This dramatic enhancement in catalytic activity can be attributed to the absence of these intercalated species that causes poisoning.

Supercapacitors are recently attracting attentions from researchers all over the world extensively as a promising energy storage device mainly because of their advantages such as high capability and power density, long life spans as well as rapid charge/discharge stability [19]. The $Ni(OH)_2$/rGO nanocomposites have shown good performance as supercapacitor materials. There are several reports in this regard reporting the applications of $Ni(OH)_2$/rGO nanocomposites prepared through different routes in the

field of energy storage [16-29]. In the present work, the $Ni(OH)_2$/rGO nanocomposite was also studied by electrochemical measurements in order to find out its suitability in supercapacitor applications. $Ni(OH)_2$/rGO nanocomposite exhibited enhanced electrochemical performance and remarkable cyclic stability than bare $Ni(OH)_2$ and rGO.

3.2 Experimental Methods

The chemicals used for the preparation of $Ni(OH)_2$/rGO catalysts, their suppliers and the synthesis process are mentioned in the Chapter 2.

3.3 Results and Discussion

We have prepared $Ni(OH)_2$/rGO nanocatalyst and employed it for a variety of applications such as the heterogeneous catalyst for reductive dechlorination of 1-chloronaphthalene, 1,4-dichloro benzene, reduction of p-nitrophenol to p-aminophenol and carried out electrochemical studies to find out its potential use for supercapacitor applications.

3.3.1 Catalyst Characterizations

In order to examine the active phase responsible for catalysis and to know the effect of $Ni(OH)_2$ and graphene in the catalytic application, the prepared catalytic system was characterized using XPS, FTIR spectroscopy, XRD and SEM and TEM analysis.

3.3.1.1 XPS Analysis

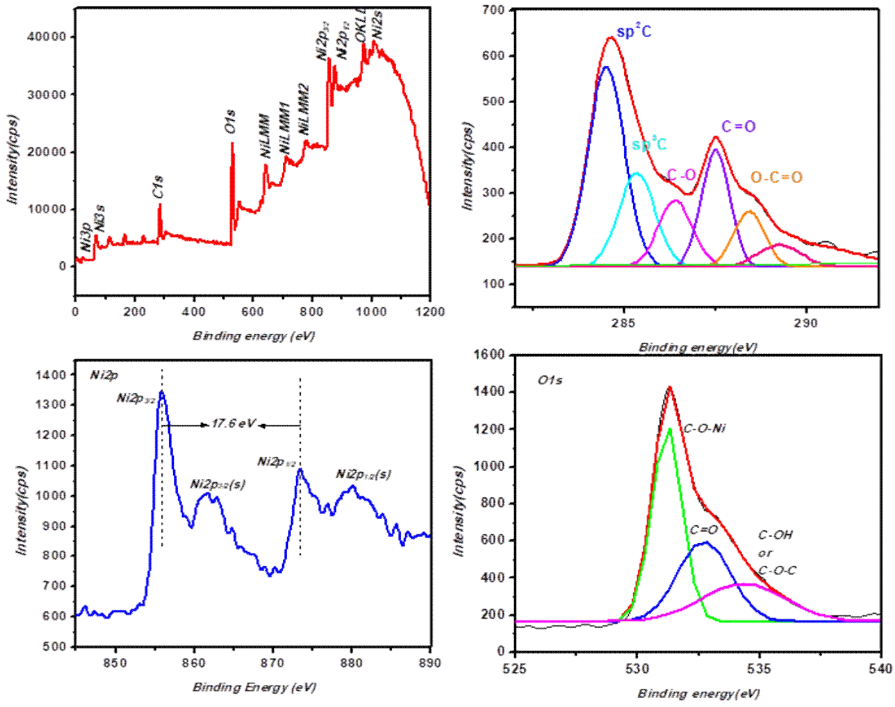

Figure 3.1: (a) XPS Survey Spectrum of $Ni(OH)_2$/rGO Nanocomposite; (b) Deconvoluted Spectra of the C1s c) Ni2p and d) O1s Regions

The elemental composition of the $Ni(OH)_2$/rGO nanocomposite was investigated using X-ray photoelectron spectroscopy (XPS) and the results were presented in Figure 3.1. The survey spectrum (0-1200 eV) of $Ni(OH)_2$/rGO showed mainly peaks corresponding to carbon (C 1s), oxygen (O 1s) and nickel (Ni 2p). In the de-convoluted spectrum of the C1s region (Figure 3.1b.) the most prominent peak was that of sp^2 hybridized non-oxygenated ring carbons of the C=C bond (284.6 eV). The peak of sp^3 hybridized carbons of C–C bond was observed at a binding energy value 285.3 eV. Similarly the peaks at

binding energy values 286.4 eV, 287.2 and 288.3 were attributed to the C in C–O bonds attached to hydroxyl and epoxy groups, the C in carbonyl groups and the carboxylate carbon respectively. Two major peaks of the Ni 2p (Figure 3.1c) centered around 873.3 eV and 855.9eV with a spin-energy separation of 17.6 eV are due to the Ni $2p_{1/2}$ and Ni $2p_{3/2}$, suggesting the presence of the $Ni(OH)_2$ phase. In addition, some extra peaks marked as satellite peaks (880.1 eV, 860.7 eV) around the Ni $2p_{1/2}$ and Ni $2p_{3/2}$ signals were also observed, typical of Ni 2p region in XPS. Figure 3.1 d shows the deconvoluted O1s spectrum with three peaks. The peak at 531.2 eV can be ascribed to oxygen belonging to C-O-Ni bond. The peak at 532.8eV can be assigned to the oxygen of C=O groups or may be a shoulder peak of O 1s in $Ni(OH)_2$, and the peak at 534.3 eV can be ascribed to oxygen atoms of C-OH and/or C-O-C groups (hydroxyl and/or epoxy) respectively [19].

3.3.1.2 XRD Analysis

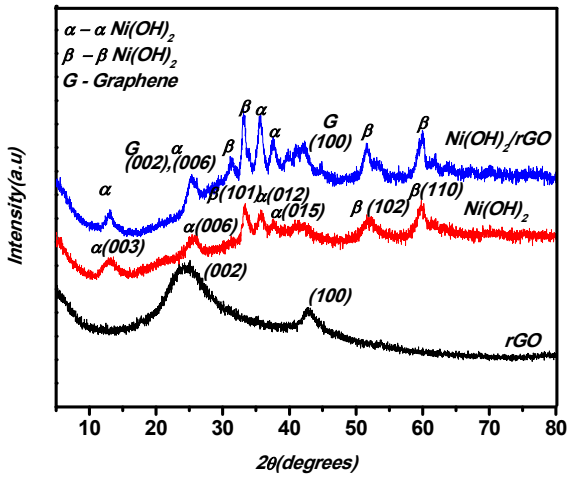

Figure 3.2: X-ray Diffraction Patterns of (a) rGO, (b) $Ni(OH)_2$, (c) $Ni(OH)_2$/ rGO

The XRD patterns recorded for the rGO, $Ni(OH)_2$, $Ni(OH)_2$/rGO composite prepared were shown in Figure 3.2. For $Ni(OH)_2$, the four peaks appeared at 2θ values of 12.8° (003), 25.4° (006), 35.6° (012), 37.7° (015)corresponds to that of α-$Ni(OH)_2$ and four peaks at 2θ values corresponds to β-$Ni(OH)_2$ which are 31.2° (100), 33.0° (101), 51.5° (102) and 60.1° (110)[20, 24, 57-60]. The characteristic peak for the reduced graphene oxide, at 25.2°, corresponding to the (002) diffraction plane represented by the intensification of (006) plane of α-$Ni(OH)_2$ at 25.4° in the nanocomposite. The presence of rGO in the composite was again confirmed by the characteristic peak for the rGO at 42.7° which corresponds to (100) plane.

3.3.1.3 FTIR Spectral Analysis

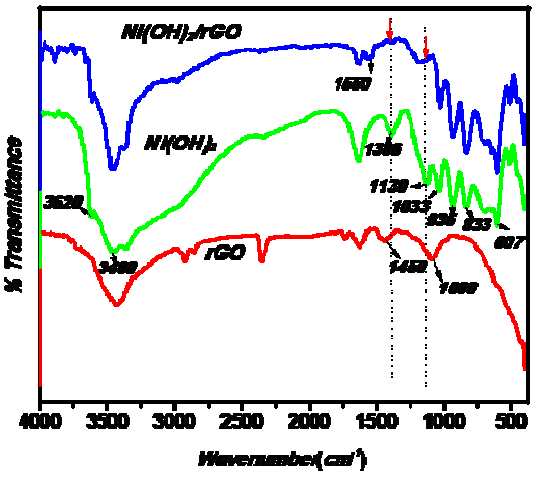

Figure 3.3: FTIR Spectra of (a) rGO, (b) $Ni(OH)_2$, (c) $Ni(OH)_2$/rGO

The FTIR spectra obtained for the $Ni(OH)_2$/rGO nanocomposite, rGO and $Ni(OH)_2$ are presented in Figure 3.3. The sharp shoulder peak at 3620 cm^{-1} may be due to the O-H stretching vibrations characteristic of $Ni(OH)_2$ and the broad absorption band centred around 3460 cm^{-1} can be attributed to other OH vibrations including adsorbed moisture. The band at 1630 cm^{-1} can be attributed to the bending vibration of water molecules. A band at 1560 cm^{-1}, observed for $Ni(OH)_2$/rGO composite corresponds to C=C stretching of rGO which indicates the formation of $Ni(OH)_2$/ rGO composite. The band at 1386 cm^{-1} may be due to the presence of interlayer NO_3^- anions in $Ni(OH)_2$ which was disappearing in the nanocomposite. Similarly, the peak at 1130 cm^{-1}, which is plausibly due to intercalated bisulphite ions, was also substantially reduced in intensity in the spectrum of the nanocomposite. The infrared peaks at 1386 $cm^{-1}$and 1130 cm^{-1} were getting vanished in the nanocomposite possibly as a result of the escape of the intercalated anions and gases during the exfoliation of nickel hydroxide platelets associated with the composite formation. The peaks below 1000 cm^{-1}can be attributed to Ni–O stretching and Ni–OH bending vibrations [24, 56, 57]. In rGO, the C=C stretching band was seen at 1450 $cm^{-1}$and the C-O stretching of residual –OH groups at the edges were observed at 1090 cm^{-1}.

3.3.1.4 SEM and TEM Analysis

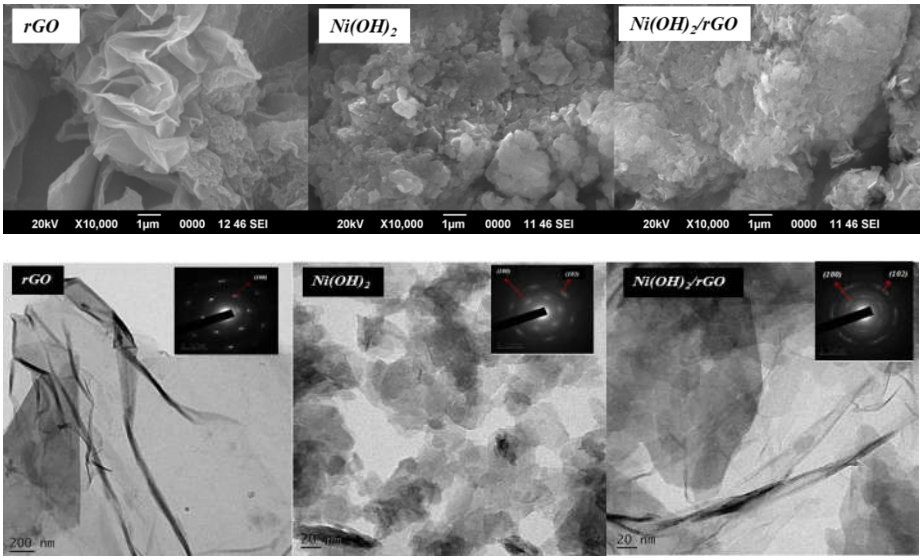

Figure 3.4: The SEM Images a) rGO b) $Ni(OH)_2$ c) $Ni(OH)_2$/rGO and the TEM Images of d) rGO e) $Ni(OH)_2$ f) $Ni(OH)_2$/rGO

The morphology of the reduced graphene oxide prepared was studied using SEM (Figure 3.4a). The layered features of the reduced graphene oxide were clearly visible in the SEM images of rGO indicating the retaining of the high degree of the exfoliation happened in the GO preparation even after the hydrothermal reduction. For $Ni(OH)_2$ produced without any graphene, the $Ni(OH)_2$ nano-platelets are observed in the SEM image (Figure 3.4b). In the SEM micrograph of the $Ni(OH)_2$ and reduced graphene oxide nanocomposite (Figure 3.4c) as well, the layered morphology is clearly evident. The detailed structural properties of rGO, $Ni(OH)_2$, $Ni(OH)_2$/rGO composite were examined by TEM (Figure 3.4 d, e and f).

3.3.2 Catalytic Activity Studies

In the present work, $Ni(OH)_2$/rGO catalysts were effectively prepared and was used in various applications such as dechlorination, nitrophenol reduction and specific capacitance measurements.

3.3.2.1 Catalytic Studies on Reductive Dechlorination of 1-Chloronaphthalene

Reductive dechlorination studies of 1-chloronaphthalene were undertaken with $Ni(OH)_2$/rGO hybrid catalyst whose performance was compared with that of the reduced graphene oxide alone as catalyst as well as bare $Ni(OH)_2$ catalyst and the results obtained were summarised in Table 3.1.

Table 3.1: Catalysts Used and Percentage of Products Formed in the Conversion of 1-Chloronaphthalene

Catalyst	1-chloronaphthalene Conversion (Wt %)	Selectivity (%)	
		Naphthalene	Tetralin
No catalyst	-	-	-
rGO	1.3	100	-
$Ni(OH)_2$	2.5	100	-
$Ni(OH)_2$ /rGO	100	-	100

All the reactions were performed with 0.3 g catalyst, 0.3 mmol 1-chloronaphthalene and 3h reaction time. Without catalyst no appreciable reaction was happening. With rGO catalyst 1.3% conversion to naphthalene was observed and with $Ni(OH)_2$ catalyst also the conversion showed only slight increase to 2.5%. In both these cases the more hydrogenated product tetralin was not observed. The

nanocomposite catalyst behaved totally differently from its individual components and favored the formation of tetralin. A 100% conversion and selectivity for tetralin was observed in three hours reaction time which demonstrates the high performance of the nanocatalyst. The uniform distribution of the nickel hydroxide nanoplatelets on the graphene sheets providing large interfacial contact favoring an efficient reductive dehalogenation process was probably the reason for this superior performance.

3.3.2.1.1 Effect of Catalyst Weight

When the catalyst weight loaded was 0.05 g, the sole product obtained was naphthalene and the conversion was also only 52.2%. Upon increasing the catalyst loading to 0.1 g, the formation of more hydrogenated product tetralin could be observed and the selectivity for tetralin increased and reached its maximum (100%) for 0.3 g catalyst loading. However further increase in catalyst weight resulted in a slight decrease in the performance, probably due to insufficient solid-liquid interfacial contact with higher catalyst amount. The results of catalyst weight optimization studies are provided in Table 3.2.

Table 3.2: Catalyst Weight Optimization Studies Using the Conversion of 1-Chloronaphthalene

Catalyst weight (g)	1-chloronaphthalene Conversion (Wt %)	Selectivity (%)	
		Naphthalene	Tetralin
0.05	52.2	100	-
0.1	99.6	67.4	32.2
0.2	100	17.8	82.2
0.3	100	-	100
0.4	99.9	18.9	81

3.3.2.1.2 Effect of Initial Reactant Concentration

Further, the effect of initial reactant amount was investigated by varying the initial amount of 1-chloronaphthalene and the results obtained were summarized in Table 3.3. Initial reactant amount optimization studies showed that for 0.1 and 0.3 mmol of 1-chloronathalene amounts, a 100% conversion and 100% selectivity to tetralin was observed. When the initial amount of 1-chloronaththalene was made to 0.5 mmol, even though a 100% dechlorination was achieved, tetralin yield was reduced to 70.6%.

Table 3.3: Optimization Studies Using the Conversion of 1-Chloronaphthaleneby Varying the Initial Reactant Amount

1-chloronaphthalene : Triethyl silane	1-chloronaphthalene Conversion (Wt %)	Selectivity (%)	
		Naphthalene (%)	Tetralin (%)
1:100	100	-	100
3:100	100	-	100
5:100	100	29.4	70.6

3.3.2.1.3 Effect of Reaction Time

Reaction time was varied from 1h to 3h keeping all other parameters constant in an attempt to find out the most suited reaction time required for the dechlorination process. 100% dechlorination was achieved within 1h and the major product formed was naphthalene (85.8%). Further increase in reaction time results in more hydrogenation which reduces the naphthalene yield and a

corresponding increase in the tetralin yield. With 3h of reaction time a 100% tetralin yield was obtained. The results obtained were presented in Table 3.4.

Table 3.4: Reaction Time Optimization Studies Using the Conversion of 1-Chloronaphthalene

Reaction time(h)	1-chloronaphthalene Conversion (Wt %)	Selectivity (%)	
		Naphthalene	Tetralin
1	100	85.8	14.2
2	100	21.7	78.3
3	100	-	100

3.3.2.2 Catalytic Studies on Reductive Dechlorination of Dichlorobenzene

A quantitative analysis of the products obtained by the dechlorination reactions of DCB was performed using Gas chromatography and the results obtained were summarised in Table 3.5. In this reaction also, compared to bare $Ni(OH)_2$, $Ni(OH)_2$/rGO was observed to be a highly efficient catalyst for the selective conversion of DCB into hydrocarbon product benzene. In this case we could observe that the reductive dechlorination was happening to some extend even without any catalyst, but does not result in complete dechlorination of DCB to benzene.

Table 3.5: Catalysts Used and Percentage of Products Formed in the Conversion of 1,4 -Dichlorobenzene (DCB)

Catalyst	Dichlorobenzene Conversion (Wt %)	Selectivity (%)		
		Chlorobenzene	Benzene	Other products
Ni(OH)$_2$ /rGO	100	5.4	94.6	-
Ni(OH)$_2$	95.11	12.18	62.63	20.3
No catalyst	47.25	23.45	1.3	22.5

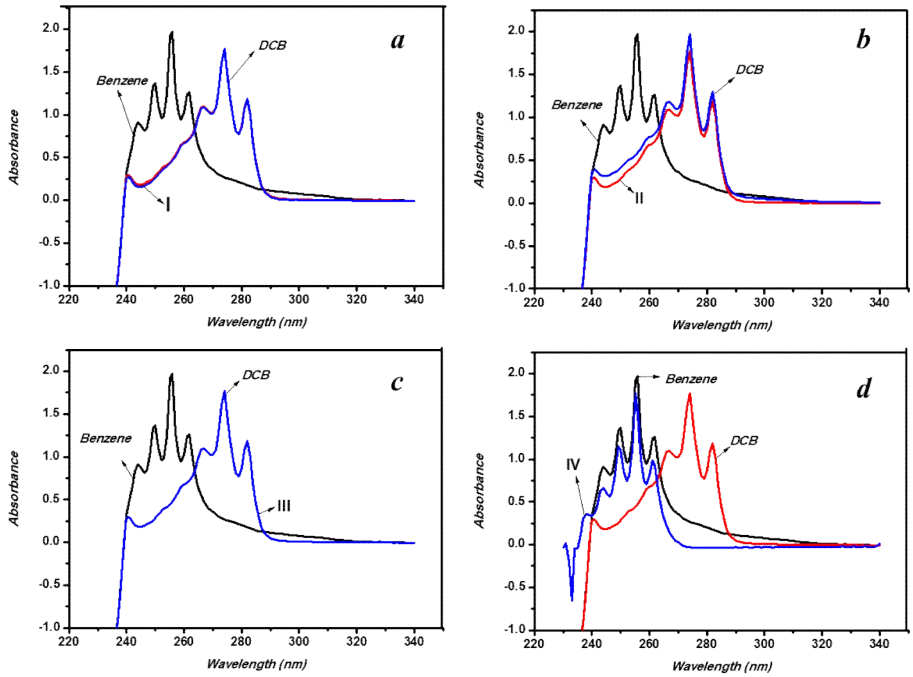

Figure 3.5: UV Absorption Spectra of Reaction Mixtures after the Separation of Catalysts. The Spectra I, II, III and IV Respectively Belongs to the Reaction Mixtures Where No Catalyst Was Used(I), Ni(OH)$_2$Was Used as Catalyst(II), rGO Was Used as Catalyst(III) and Ni(OH)$_2$/rGO Was Used as Catalyst(IV).

The formation of benzene is further confirmed by the UV absorption spectra recorded after carrying out the reaction and separation of catalyst (Figure 3.5.). It was observed that the characteristic benzenoid band resulting from the $\pi \rightarrow \pi^*$ transition in benzene was observed only for the reaction mixture for which the $Ni(OH)_2$/rGO catalyst was used(figure 3.5d). Since the benzene content in reaction mixtures where rGO and $Ni(OH)_2$ were used as catalyst were low, their corresponding absorption profiles showed more closeness to that of DCB (figure 3.5b & c). The fact that 94.6% conversion to benzene was achieved with the $Ni(OH)_2$/rGO nanocomposite catalyst makes it an excellent heterogeneous catalyst system suitable for a total effective dechlorination, especially for lower chlorinated aromatic hydrocarbons such as dichlorobenzenes.

3.3.2.3 Reduction of p-Nitrophenol

Reduction of p-nitrophenol was undertaken with $Ni(OH)_2$/rGO hybrid catalyst whose performance was compared with that of bare $Ni(OH)_2$ catalyst and the results obtained were summerised in figure 3.6. For bare $Ni(OH)_2$, the time taken for completing the reduction reaction of p-nitrophenol to p-aminophenol was 32 min. The reaction was slower and the apparent rate constant was calculated by monitoring the intensity reduction of the main peak at 400 nm and plotting ln (A/A_0) against time. The reaction started after an induction period and also towards the end of the reaction the rate constant again changed to a faster rate probably due to lesser competition for the active sites. Therefore, for k_{app} calculation, only the straight line portion from 8 min to 22 min was used and the value obtained was 0.071 min^{-1}.

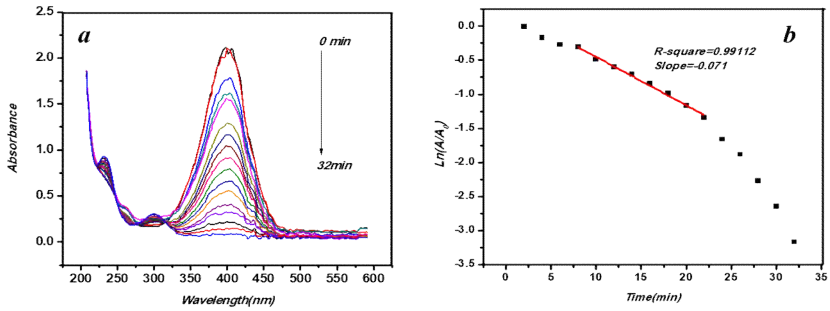

Figure 3.6: a) UV Absorption Spectra and b) The corresponding Plot of $\ln(A/A_0)$ against reaction time for the reduction reaction of p-Nitrophenol to p-Aminophenol using Bare $Ni(OH)_2$ as Catalyst.

The same reaction was completed within 14 min when the $Ni(OH)_2$/rGO nanocomposite was used as catalyst. From the UV spectra we could observe that the rate of conversion of p-nitrophenol to p-aminophenol was considerably enhanced when the nanocatalyst was employed. k_{app} value obtained was 0.20 min^{-1}. This reaction also demonstrated the excellent capability of the $Ni(OH)_2$/rGO nanocomposite to function as a high performing catalyst for reduction reactions.

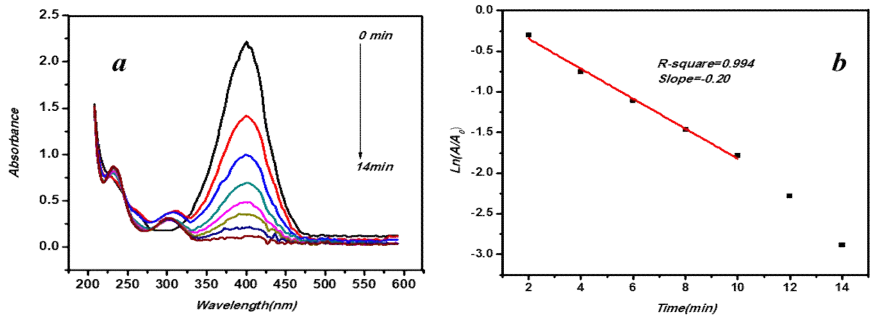

Figure 3.7: a) UV Absorption Spectra and b) The corresponding Plot of $\ln(A/A_0)$ against reaction time for the reduction reaction of p Nitrophenol to p-Aminophenol using $Ni(OH)_2$/rGO Nanocomposite as catalyst.

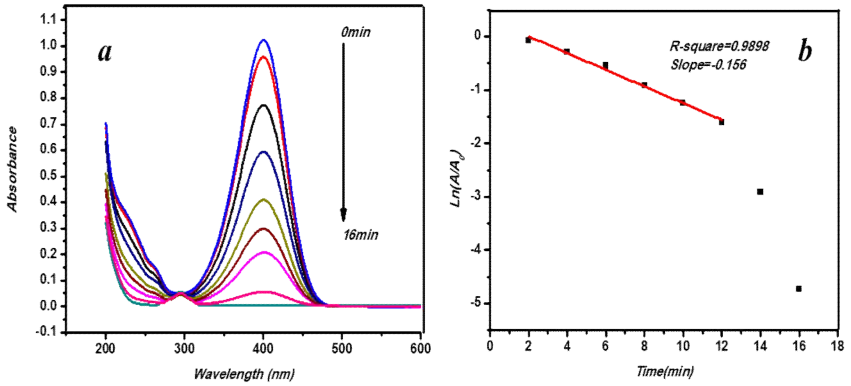

Figure 3.8: a) UV Absorption Spectra and b) The corresponding Plot of $\ln(A/A_0)$ against reaction time for the reduction reaction of p-Nitrophenol to p-Aminophenol using aged $Ni(OH)_2$/rGO nanocomposite (one year six months after its preparation)

$Ni(OH)_2$/rGO catalyst was found to be quite stable. One year six months after its preparation, we repeated the nitrophenol reduction reaction and the apparent rate constant was calculated. It was observed that the catalytic performance was good without much loss in activity (complete reduction was attained in 16 min, the value for a fresh catalyst being 14 min).

The rate constant calculations were performed and a comparison with the existing literature have been summarised in Table (3.6) which shows that the prepared $Ni(OH)_2$/rGO catalytic system, as a cost-effective catalyst free of noble metals, exhibited excellent prerformance in the 4-nitrophenol reduction catalytic studies, in camparison with many previous reports.

Table 3.6: Comparison of Catalytic Efficiency of $Ni(OH)_2$/rGO with Previously Reported Works of Reduction of 4-NP

Catalyst	4-NP	Rate Constant k(app)/min^{-1}	Reference
AgNP-PG-5K	0.12mM	0.33	61
AuPdNPs/GNs	0.1mM	0.792	62
RANEY* Ni	0.1mM	0.32	63
A CTAB		1.0	
B PEG-10000		1.3	
C Gelatin		1.8	
D CTAB + PEG-10000		2.7	
E CTAB + gelatin		2.4	
TAC-Ag-1.0	0.103mM	0.3114	64
TAC-Ag-1.4		0.099	
TAC-Ag-0.7		0.1668	
TSC-Ag-1.4		0.02184	
Ag-NP-Doped Carbon Spheres	0.05mM	0.1014	65
Pd-FG nanohybrids	0.1mM	0.141	66
$Ni(OH)_2$/rGO	0.5 mM	0.20	This work

The tremendous increase in the catalytic performance of $Ni(OH)_2$/rGO catalyst compared to $Ni(OH)_2$ alone demonstrated the significance of the role of rGO in the composite capable of facilitating the reactant adsorption and product diffusion processes exposing the catalytically active sites in a better way. The presence of intercalated anions and other gases in the interlayer spacing of bare nickel hydroxide catalyst as evident from the FTIR studies may be having a detrimental effect with regard to catalysis. Once the composite was formed with graphene, nickel hydroxide nano-platelets got exfoliated and uniformly got dispersed on the rGO sheets shedding out all the masking anions and gases in the interlayer spaces. In a recent report,

Jia et al. have described how catalytic performance of nickel hydroxide can be improved by increasing the interlayer spacing resulting in the escape of trapped anions and gases[55]. Another factor which might have contributed significantly to the high performance of the catalyst was the electron richness of graphene which can favour reduction reactions.

3.4 Conclusions

$Ni(OH)_2$/rGO nanocatalyst has been successfully synthesized through a facile, hydrothermal method. From the XPS, XRD, FTIR and SEM and TEM analysis, it can be concluded that $Ni(OH)_2$ platelets were exfoliated and uniformly dispersed on the rGO sheets which made the nanocomposite a far superior catalyst compared to bare nickel hydroxide. $Ni(OH)_2$/rGO nanocomposite showed excellent performance to the reductive dechlorination of dichlorobenzene to benzene and 1-chloronaphthalene to tetralin with 94.6% and 100 % conversion respectively in optimum reaction conditions. Because of the non-polar and volatile nature of the hydrocarbon products, their removal from the reaction medium can be considered as an easy step. The fact that precious metals or their compounds are not incorporated in to the catalytic system make the entire process more economical as well. Thus, we believe that the work presented here is worth pursuing with other polychlorinated aromatic hydrocarbons and the catalyst developed possesses the potential to become an industrially important one in the CVOC removal technology**.** For the reduction of p-nitrophenol to p-aminophenol, $Ni(OH)_2$/rGO nanocomposite performed excellently than bare $Ni(OH)_2$ with a time of only 14 min for complete reduction. Bare $Ni(OH)_2$ showed 32 min for the same reaction.

References

1. V. Singh, D. Joung, L. Zhai, S. Das and S. I. Khondaker and S. Seal, *Mater Sci Prog.,* 2011, **56**, 1178-1271.
2. X. Huang, X. Qi, F. Boey and H. Zhang, *Chem. Soc. Rev.,* 2012, **41**, 666-686.
3. X. Huang, Z. Yin, S. Wu, X. Qi, Q. He, Q. Zhang, Q. Yan, F. Boey and H. Zhang, *Small.,* 2011, **7**, 1876-1902.
4. M. J. Allen, V. C. Tung and R. B. Kaner, *Chem. Rev.,* 2010, **110**, 132-145.
5. K. S. Novoselov, A. K. Geim, S. V. Morozov, D. Jiang, Y. Zhang, S. V. Dubonos, I. V. Grigorieva and A. A. Firsov, *Science*., 2004, **306**, 666-669.
6. K. S. Novoselov, D. Jiang, F. Schedin, T. J. Booth, V. V. Khotkevich, S. V. Morozov and A. K. Geim, *PNAS.,* 2005, **102**, 10451-10453.
7. A. K. Geim and K. S. Novoselov, *Nat Mater.,* 2007, **6**, 183-191.
8. S. Stankovich, D. A. Dikin, R. D. Piner, K. A. Kohlhaasa, A. Kleinhammes, Y. Jia, Y. Wu, S. T. Nguyen and R. S. Ruoff, *Carbon.,* 2007, **45**, 1558-1565.
9. S. Pei and H. M. Cheng, *Carbon.,* 2012, **50**, 3210-3228.
10. K. Haubner, J. Morawski, P. Olk, L. M. Eng, C. Ziegler, B. Adolphi and E. Jaehne, *ChemPhysChem.,* 2010, **11**, 2131-2139.
11. K. Ojha, O. Anjaneyulu and A. K. Ganguli, *Curr. Sci.,* 2014, **107**, 397-418.
12. S. Bai, X. Shen, G. Zhu, M. Li, H. Xi and K. Chen, *ACS Appl. Mater. Interfaces.,* 2012, **4**, 2378-2386.
13. Z. Ji, X. Shen, G. Zhu, H. Zhou and A. Yuan, *J. Mater. Chem.,* 2012, **22**, 3471-3477.
14. J. M. Song , J. J. Ni, J. Zhang, D. Ling, H. L. Niu, C. J. Mao, S. Y. Zhang and Y. H. Shen, *J Nanopart Res.,* 2014, **16**, 2269-2274.

15. B. Garg, T. Bisht and Y. C. Ling, *Molecules.,* 2014, **19**, 14582-14614.

16. S. Chen, J. Duan, Y. Tang and S. Z. Qiao, *Chem. Eur. J.,* 2013, **19**, 7118-7124.

17. J. Zhu, S. Chen, H. Zhou and X. Wang, *Nano Res.,* 2012, **5**, 11-19.

18. S. R. Gómez, A. Boscá, L. Pérez, J. Pedrós, J. Martínez , A. Páez and F. Calle, *Diamond Relat. Mater.,* 2015, **57**, 63-67.

19. W. Liu, C. Ju, D. Jiang, L. Xu, H. Mao and K. Wang, *Electrochim. Acta.,* 2014, **143**, 135-142.

20. F. Zhang, D. Zhu, X. Chen, X. Xu, Z. Yang, C. Zou, K. Yang and S. Huang, *Phys. Chem. Chem. Phys.,* 2014, **16**, 4186-4192.

21. Z. Qian, T. Peng, L. Qu, J. Wang and P. Wang, *J. Mater. Chem. A.,* 2014, **2**, 4894-4898.

22. Y. Bai, W. Wang, R. Wang, J. Sun and L. Gao, *J. Mater. Chem. A.,* 2015, **3**, 12530-12538.

23. X. Meng, J. Zhu, H. Bi, Y. Fu, Q. Han and X. Wang, *J. Mater. Chem. A.,* 2015, **3**, 21682-21689.

24. X. Chen, X. Chen, F. Zhang, Z. Yang and S. Huang, *J. Power Sources.,* 2013, **243**, 555-561.

25. R. Xu, T. Xie, Y. Zhaoand Y. Li, *Nanotech.* 2007, **18**, 055602-055606.

26. L. L. Zhang, Z. Xiong, X. S. Zhao*, J. Power Sources.,* 2013, **222**, 326-332.

27. J. Ji, L. L. Zhang, H. Ji, Y. Li, X. Zhao, X. Bai, X. Fan, F. Zhang and R. S. Ruoff, *ACS Nano.,* 2013, **7**, 6237-6743.

28. M. F. Hossain, J. Yin and J. Y. Park, *Jpn. J. Appl. Phys.,* 2014, **53**, 08NC02-08NC02-5.

29. S. Yang, B. Deng, R. Ge, L. Zhang, H. Wang, Z. Zhang, W. Zhu and G. Wang, *Nanoscale Res Lett.,* 2014, **9**, 672-682.

30. C. H. Yeh and J. J. Ho, *Phys. Chem. Chem. Phys.,* 2015, **17**, 7555-7563.

31. T. N. P. Bosma, J. R. Meer, G. Schraa, M. E. Tros and A. J. B. Zehnder, *FEMS Microbiol. Ecol.,* 1988, **53**, 223-229.

32. W. H. Casey, *Science.,* 2002, **295**, 985-986.

33. A. C. Leri and S. C. B. Myneni, *Global Biogeochem. Cy.,* 2010, **24**, GB402 (1-8).

34. S. C. B. Myneni, *Science.,* 2002, **295**, 1039-1041.

35. Y. H. Xu, Q. Q. Cai, H. X. Ma, Y. He, H. Zhang and C. A. Ma, *Electrochim. Acta.,* 2013, **96**, 90-96.

36. S. Y. Baek, S. D. Choi, H. Park, J. H. Kang and Y. S. Chang, *Environ. Sci. Technol.,* 2010, **44***,* 3035-3040.

37. M. A. Keane, *Chem. Cat. Chem.,* 2011, **3**, 800-821.

38. A. Ghaffar and M. Tabata, *Green Chem. Lett. Rev.,* 2010, **3**, 179-190.

39. W. Wu, J. Xu and R. Ohnishi, *Appl. Catal. B*., 2005, **60**, 129-137.

40. L. M. Rossi, J. L. Fiorio, M. A. S. Garcia, C. P. Ferraz, *Dalton Trans.,* 2018, **47**, 5889-5915.

41. R. Baumgartner, G. K. Stieger, and K. McNeill, *Environ. Sci. Technol.,* 2013, **47**, 6545-6553.

42. X. Ma, S. Liu, Y. Liu, G. Gu and C. Xia, *Sci. Rep.,* 2016, **6**, 25068 (1-10). doi: 10. 1038/srep25068.

43. C. A. Ohlin, Z. Beni, G. Laurenczy, N. Ruiz and A. M. M. Bulto, *Appl. Organometal. Chem.,* 2007, **21**, 156-160.

44. R. Abazari, F. Heshmatpour and S. Balalaie, *ACS Catal*., 2013, **3**, 139-149.

45. H. Vijwani, A. Agrawal and S. M. Mukhopadhyay, *J. Nanotechnol*., 2012, **478381** (1-9). Doi:10. 1155/2012/478381.

46. F. Alonso, I. P. Beletskaya and M. Yus, *Chem. Rev.,* 2002, **102**, 4009-4091.

47. X. Xu, H. Zhou, P. He and D. Wang, *Chemosphere.,* 2005, **58**, 1135-1140.

48. V. E. Muradyan, V. S. Romanova, A. P. Moravsky, Z. N. Parners and Y. N. Novikov, *Russ. Chem. Bull*., 2000, **49**, 1017-1019.

49. Y. Du, H. Chen, R. Chen and N. Xu, *Appl. Catal., A.,* 2004, **277**, 259-264.

50. Z. Ji, X. Shen, G. Zhu, H. Zhou and A. Yuan, *J. Mater. Chem.,* 2012, **22**, 3471-3477.

51. T. O. Egbuchunam, G. Obi, F. E. Okieimen and S. Yetgin, *J. Chem. Chem. Eng.,* 2016, **10**, 325-335.

52. D. T. Villiams, B. Kennedy and G. L. Le Bel, *Chemosphere.,* 1993, **27**, 795-806.

53. T. Kunisue, B. J. Restrepo, D. R. Hilker, K. M. Aldous and K. Kannan, *Environ. Pollut.,* 2009, **157**, 910-915.

54. H. Park, J. H. Kang, S. Y. Baek and Y. S. Chang, *Environ. Pollut.,* 2010, **158**, 1420-1427.

55. D. Jia, H. Gao, W. Dong, S. Fan, R. Dang, and G. Wang, *ACS Appl. Mater. Interfaces.,* 2017, **24**, 20476-20483.

56. A. S. Adekunle, J. A. O. Oyekunle, O. S. Oluwafemi, A. O. Joshua, W. O. Makinde, A. O. Ogunfowokan, M. A. Eleruja and E. E. Ebenso, *Int. J. Electrochem. Sci*., 2014, **9**, 3008-3021.

57. G. Fu, Z. Hu, L. Xie, X. Jin, Y. Xie, Y. Wang, Z. Zhang, Y. Yang and H. Wu, *Int. J. Electrochem. Sci*., 2009, **4**, 1052-1062.

58. P. Jeevanadham and V. R. R. Pulimi, *Indian J. Chem*., 2012, **51**, 586-590.

59. H. Y. Wu, Y. L. Xie and Z. A. Hu, *Int. J. Electrochem. Sci*., 2013**, 8,** 1839-1848.

60. B. Li, M. Ai and Z. Xu, *Chem. Commun.,* 2010, **46**, 6267-6269.

61. B. Baruah, G. J. Gabriel, M. J. Akbashev and M. E. Booher, *Langmuir.*, 2013, **29**, 4225−4234.

62. X. Chen, Z. Cai, X. Chen and M. Oyama, *J. Mater. Chem.*, 2013,

63. Z. Jiang, J. Xie, D. Jiang, X. Wei and M. Chen, *CrystEngComm.*, 2013, **15**,560-569.

64. M. H. Rashid and T. K. Mandal, *J. Phys. Chem. C.,* 2007, **111**, 16750-16760.

65. S. Tang, S. Vongehr and X. Meng**,** *J. Phys. Chem. C.,* 2010**, 114**, 977–982.

66. Z. Wang, C. Xu, G. Gao and X. Li, *RSC Adv.,* 2014, **4**, 13644-13651.

Chapter 4

Zinc Oxide/Graphene Nanocomposites and Their Photocatalytic Applications

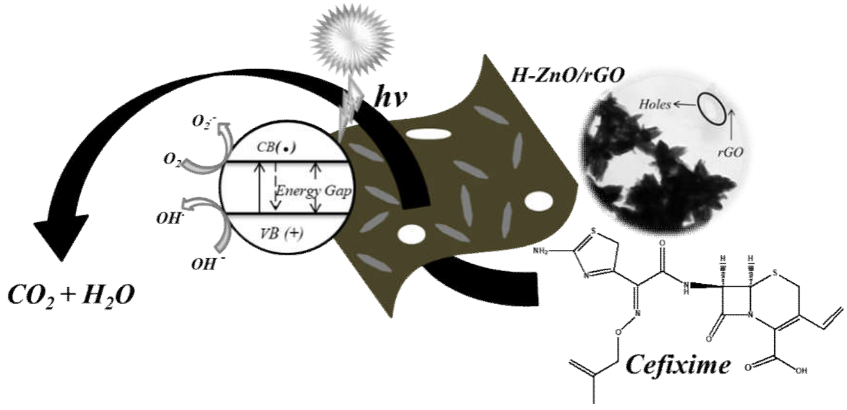

4.1 Introduction

As detailed in chapter 1, ZnO is an n-type semiconductor with unique structure and properties such as large band gap (3.37 eV)[1-3], high exciton binding energy of 60 meV [2], high sensitivity for ultraviolet (UV) light. Low fabrication cost is another attractive factor regarding ZnO, estimated to be almost 75% cheaper than titania[3]. It is widely used for many applications, especially, in the field of photoluminescence [4], light-emitting diodes [5], field-effect transistors [6,7], ultraviolet lasers [8], chemical sensors [9], solar cells [10,11], cathodoluminescence [12] and photocatalysis [13-15]. Even though ZnO can be considered as a promising photocatalyst suitable for many purposes[16], there are several issues that limit the utilization of pure ZnO for photocatalytic applications. The major challenge is the high recombination rate of photogenerated electron–hole pairs[17]. Therefore, for enhanced photocatalytic efficiency, it is essential to slow down the recombination of the charge carriers by various means[18].

Some of the strategies adapted by different research groups for improving the photocatalytic performance of ZnO are improving its structural design, noble metal loading, doping with carbon materials, ion doping, and the coupling with other semiconductors [1]. ZnO have been prepared by various methods to enhance the photocatalytic activity [19, 20]. For example, Li et al. have reported ZnO with different morphologies, including column-like, grenade-like, rod-like, spindle-like, flower-like and shuttle-like micro-/nanostructures, and the results showed that the spindle-like photocatalyst showed the maximum photocatalytic activity [20]. Doping of Eu^{3+}, Ce, Fe^{3+}, and Ag can

improve the photocatalytic performance of ZnO since these elements can act as electron trapping agents to curb electron hole recombination rate [21-25]. Among doped nanostructures, Ce/ZnO nanocomposite has been synthesized and studied for degradation of a variety of dyes, infrared emissivity, detoxification of cyanide, etc [26-32].

As we have already seen in chapter 1, carbonaceous materials of remarkable interest due to their unique electronic properties, adsorptive capacity and acidity. These materials include activated carbon, carbon nanotubes, fullerene and graphene [33]. As a new kind of fascinating two-dimensional carbon material made by single layer of carbon atoms, graphene is an excellent supporting and electron-transport material well suited as a co-catalyst in a photocatalytic system owing to its large surface area, high carrier mobility, superior electrical conductivity and mechanical properties [34-36]. Additionally, graphene can be easily produced from inexpensive natural graphite via a facile chemical oxidation-exfoliation-reduction procedure at a low cost through the intermediate product graphite oxide (GO) [37]. Now a days, graphene oxide (GO) is also receiving increasing attention among researchers. The presence of oxygen-containing functional groups in GO and reduced GO will make them excellent supporting materials to anchor catalytically active nanocrystals during the process of synthesis graphene based nanocatalysts [38].

It is expected that the combination of ZnO with graphene may be ideal choice to have superior photocatalytic performance [39-49]. Because of the conjugated structure of graphene which facilitates the

charge separation in the photocatalysis process, the hybridization of ZnO with graphene can substantially reduce the recombination of charge carriers and increase the photocatalytic performance [33, 50, 51]. In ZnO-graphene hybrid materials, ZnO get excited causing the transfer of the electrons from valence band to conduction band creating electron-hole pairs, which can migrate to the semiconductor surface and initiate redox reactions with water and oxygen, and then degrade organic molecules [52-58], as detailed in chapter 1.

Antibiotics are naturally occurring, semi-synthetic and synthetic compounds with antimicrobial activity that can be administered orally or by parenteral means or applied topically, used in human or used as a veterinary medicine to treat and prevent diseases, and also in use for other purposes such as growth promotion in food animals [59]. However, as a result of their overuse and misuse, antibiotics which can challenge microbial populations, must be considered as important pollutants as well [60]. In recent years, the ubiquitous application and release of these antibiotics to the surroundings is recognized as an emerging environmental threat which can lead to a situation called bacterial antibiotic resistance. The emergence of antibiotic resistant bacterial strains is a serious risk to humans and other animals [61-63]. In this scenario, safer methods of disposal of drugs are of a vital issue of concern today which compels for the development of better methods for the purpose. Photocatalysis, which can be termed as one of the advanced oxidation processes (AOPs), is an efficient and cost effective technique suitable for water and air purification [64].

After the first clinical use of penicillin, β-lactam antibiotics have undergone a remarkable evolution in the past 75 years. They are generally categorised as among the safest, most effective and most widely used antibiotic drugs in clinical practice. Structural additions to the basic 4, 5-β-lactam ring have led to the development of antibiotics such as penicillin V, ampicillin and amoxicillin. The cephalosporins, another naturally occurring class of β -lactams, came in to clinical use 20 years after the introduction of penicillin [65]. The basic difference in the chemical structure of cephalosporins and penicillins are the six-membered dihydrothiazine (cephem) ring system fused to the β-lactam ring [66]. Many cephalosporins which have offered broad-spectrum coverage and possess impressive safety profiles have been introduced in the past two decades. However, most of these agents require parenteral administration [67]. Only a few oral cephalosporins are currently available, owing to the difficulty associated with achieving sufficiently high absorption levels [65]. Cefixime is such an antibiotic which belongs to β-lactam family. It covers a wide range of diseases related to urinary tract infection, bronchitis, pneumonia, prostatitis, syphilis and infections of reproductive organs and so on. Its chemical formula can be written as (6R, 7R)-7[(Z)-2-(2- amino-4-thiazolyl)-2-(carboxymethoxyimino]-acet-amido)-8-oxo-3-vinyl-5-thia-1-azabicyclo(4,2,0) octa-2-ene-2 carboxylic acid. Its structure is showed in figure 4.1.

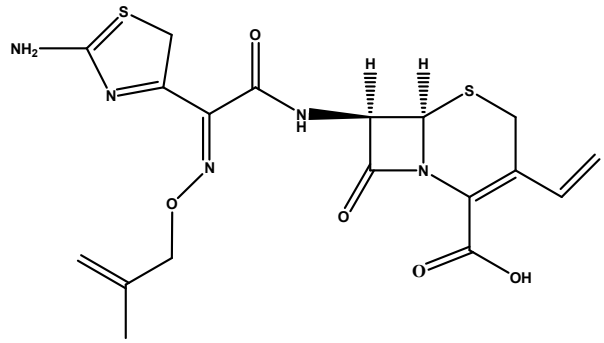

Figure 4.1: Structure of Cefixime

There are a considerable number of reports regarding removal of harmful compounds from air and water employing photocatalytic remediation methods [68-84]. In many of them, ZnO nanoparticles act as photocatalysts which includes a number of reports in which, the photocatalytic degradation is carried out using ZnO/graphene nanocomposites [75-84].

In the present study, we report the preparations and characterizations of ZnO/graphene nanocomposites via three different methods which can act as high performance photocatalysts for the oxidative degradation of cefixime antibiotic under sunlight irradiation. We have also studied the effect of various parameters such as catalyst loading, effect of irradiation time, initial antibiotic concentration, presence of H_2O_2 and comparison of High pressure mercury lamp irradiation and sunlight irradiation. The present study can be considered as a step towards photocatalytic waste water purification employing sunlight as an effective source of energy and also can be

considered as part of the world vide efforts to fight the battle against antibiotic resistant microbes.

4.2 Experimental Methods

The chemicals used for the preparation of different ZnO/graphene catalytic systems, their suppliers and the synthetic procedures adapted are given in detail in Chapter 2.

4.3 Results and discussion

We have employed ZnO/graphene nanocatalytic systems prepared by adapting three different routes for the photocatalytic degradation of Cefixime antibiotic under sunlight irradiation.

4.3.1 Catalyst Characterizations

ZnO/graphene nanocomposites prepared were characterized using FTIR spectroscopy, XRD, SEM, TEM, Raman Spectroscopy and UV-Visible Diffuse Reflectance Spectral measurements.

4.3.1.1 XRD Analysis

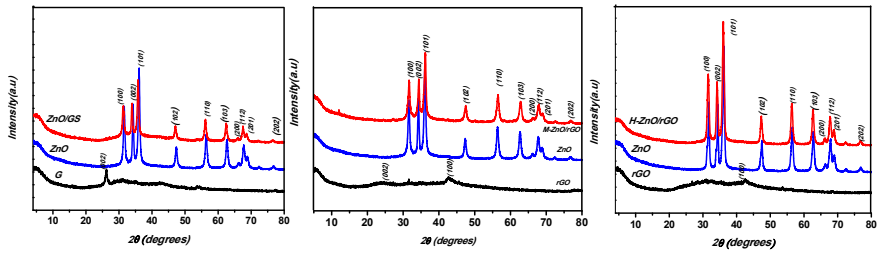

Fiqure 4.2: XRD Spectra for the Catalysts Prepared Via Different Methods

In the XRD pattern of the ZnO nanoparticles (Figure 4.2), the peaks at 2θ values of 31.4°, 33.9°, 35.9°, 47.1°, 56.1°, 62.5° and 67.6° correspond to (110), (002), (101), (102), (110), (103) and (112) crystalline planes of ZnO, respectively [1]. The main peaks in the XRD patterns of ZnO/G_S, M-ZnO/rGO and H-ZnO/rGO nanocomposites are shown in Figure 4.2. Since the diffraction peaks of the three nanocomposites showed the main peaks of ZnO almost in the same positions and the crystallinity of ZnO nanoparticles did not show any significant difference imply that they have no structural changes even after their deposition on the surface of graphene sheets, as observed in the XRD patterns of the nanocomposites. The reflection from the (002) planes of graphene could not be identified in the XRD patterns of the nanocomposites, probably due to the absence of stacking of graphene layers in them.

4.3.1.2 FTIR Spectral Analysis

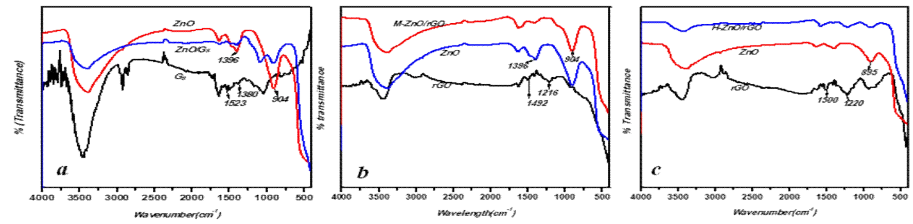

Fiqure 4.3: FTIR Spectra for the Catalysts Prepared Via Different Methods

The FTIR spectra for the G_S, ZnO_M and ZnO/G_S samples are presented in Figure. 4.3a. The vibrational absorption due to the C=C stretching at 1523 cm^{-1} and N-H bending vibrations were observed at 904 cm^{-1}.The peaks at 1396 cm^{-1} which corresponds to the vibrations of NO_3^- anions were getting systematically disappeared in the composite. The FTIR spectra for the G_M, ZnO_M and M-ZnO/rGO

samples prepared via microwave irradiation are presented in Figure. 4.3b. In the figure 4.3b, the peaks at 1492 cm^{-1} corresponds to the C=C stretching vibration, the peaks at 1216 cm^{-1} is due to the C-OH stretching vibration and the N-H bending vibration observed at 906 cm^{-1}. The FTIR spectra for the G_H, ZnO_H and H-ZnO/rGO samples prepared via hydrothermal method are presented in Figure 4.3c. Here, the C=C stretching skeletal vibrations of graphene sheets (peak at 1500 cm^{-1}), C-OH stretching vibration (at 1220 cm^{-1}) and the N-H bending vibration were also present at 895 cm^{-1}. The Zn-O stretching vibrations were observed below 500 cm^{-1} in all the nanocomposite samples. The FTIR results obtained were in tune with the observation that ZnO/graphene nanocomposites were formed.

4.3.1.3 SEM Analysis

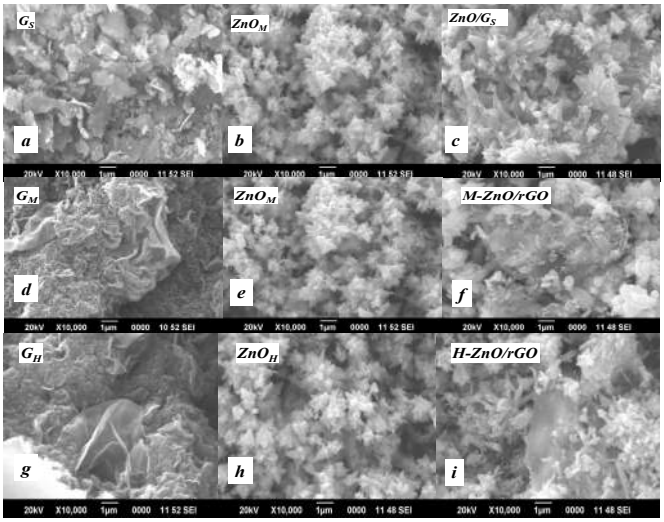

Fiqure 4.4: SEM Images of a) $G_{s,}$ b) ZnO and c)ZnO/G_sPrepared Via Liquid Exfoliation d) rGO Used in the Microwave Method e) ZnO_M and f) M-ZnO/rGO Prepared Via Mocrowave Irradiation g) rGO Used in the Hydrothermal Method h) ZnO_H and i) H-ZnO/rGO Prepared Via Hydrothermal Method

To investigate the surface morphology of ZnO/graphene nanocomposites prepared, SEM images were taken which are presented in Figure 4.4. The graphene prepared via solvent exfoliation method (figure 4.4a) was observed to be less exfoliated compared to the rGO samples (figure 4.4 d & g). From the SEM image of ZnO/G_s(Figure 4.4c), it was observed that ZnO particles had assembled to form microflower like structures, anchored on graphene sheets. The morphology of ZnO/rGO prepared via mocrowave irradiation (figure 4.4f) was also not much different from the previous one and the surface of wrinkled rGO nanosheets were found to be packed densely by ZnO nanoparticles, which displayed a good dispersion of ZnO over rGO nanosheets. Reduced graphene oxide samples had a wrinkled feature demonstrating a good degree of exfoliation as observed in the figure 4.4d and 4.4g. ZnO microflowers were anchored well on the edges and surface of the reduced graphene oxide sheets in the H-ZnO/rGO nanocomposites.

4.3.1.4 TEM Analysis

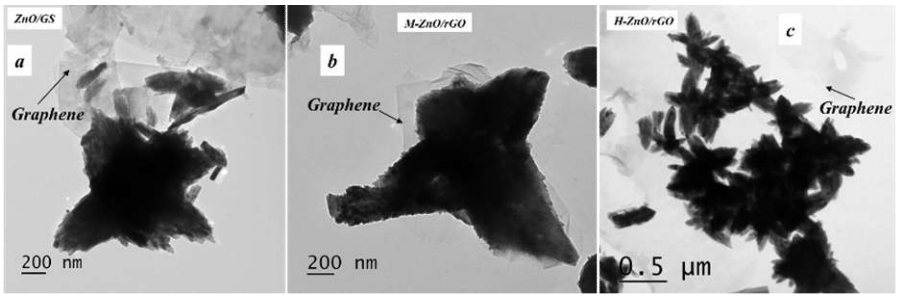

Fiqure 4.5: TEM Images of a) ZnO/G_S, b) M-ZnO/rGO and c) H-ZnO/rGO

Figure 4.5 (a,b,c) shows the TEM images of ZnO/graphene nanocomposites prepared via liquid phase exfoliation, microwave irradiation and hydrothermal route respectively. It is clear that from the figure 4.5a the ZnO nanoparticles were agglomerated and no individual particles were visible in the TEM image. In the figure 4.5b it was found that ZnO particles assemble on the graphene sheets in a relatively high density and the rGO edges appear to be wrinkled. In the figure 4.5c also (H-ZnO/rGO), the ZnO microflowers were found to be sticking on the surface of graphene sheets.

4.3.1.5 UV-Visible Diffuse Reflectance Spectral Measurements

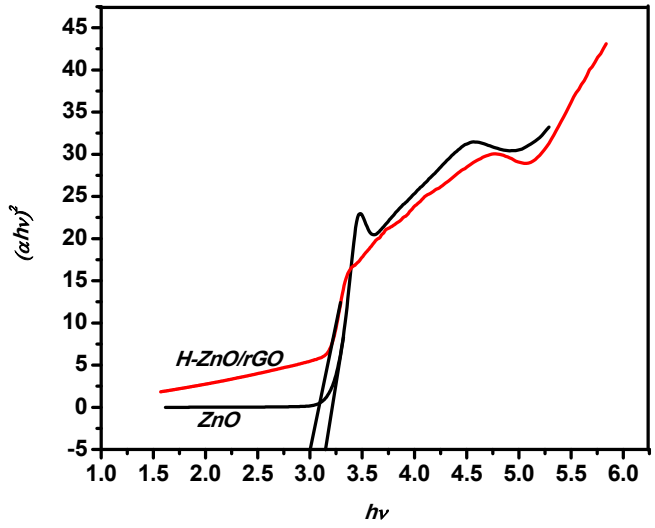

Fiqure 4.6: Kubelka-Munk Plots for Bare ZnO and H-ZnO/rGO Nanocomposite Photocatalysts

The UV-Visible reflectance spectra for the prepared H-ZnO/rGO nanocomposite and the bare ZnO photocatalysts were measured and it was found that the absorption edge showed a slight red shift when the spectrum of H-ZnO/rGO was compared with that of bare ZnO. The band gaps were determined from Kubelka-Munk plots obtained from UV-visible diffuse reflectance spectral measurements. Kubelka-Munk plots revealed a decrease in the band gap from 3.14 eV to 3.00 eV for H-ZnO/rGO compared to ZnO bringing the absorption to the visible region. This band gap modification demonstrates that the photocatalyst will be more sunlight active with efficient visible light harvesting. Since the nanocomposites ZnO/G_S, and M-ZnO/rGO did not show much promise in the photocatalytic degradation studies, their UV-Vis diffuse reflectance spectral analysis were not performed.

4.3.1.6 Raman Spectroscopic Analysis of Solvent Exfoliated Graphene

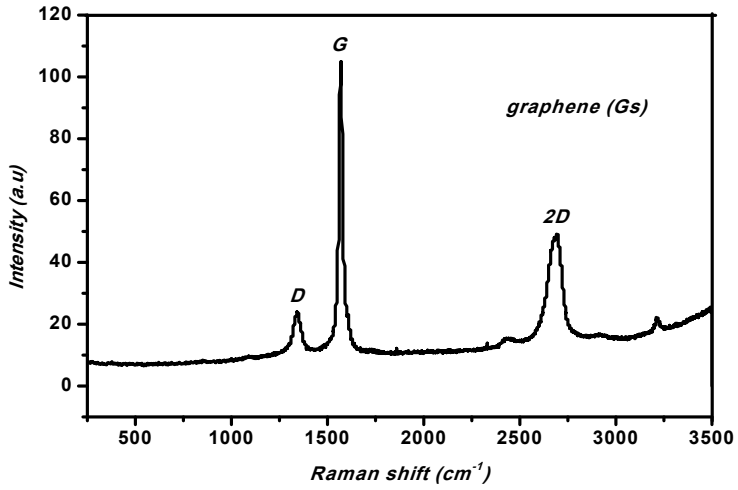

Fiqure 4.7: Raman Spectrum of solvent exfoliated Graphene

The Raman spectrum of the prepared solvent exfoliated graphene are presented in figure 4.7. Raman spectroscopy has considered as one of the most important techniques for characterizing graphene materials in a non-destructive way to provide information on structural features, density of defects and the number of graphene layers. Graphite and graphene materials are characterized by an intense band about 1570 cm^{-1} (termed as G band) as a result of in-plane vibrations of sp^2-bonded carbons. Another band termed as D band around 1350 cm^{-1} is generated by the out-of-plane vibrations of sp^2carbon atoms which will be active only in the presence of defects such as edges, sp^3 carbons, vacancies, etc. Yet another important band, designated as 2D band, is around 2690 cm^{-1} and is attributed to the second-order two phonon mode. This band is highly sensitive to the quality and number of graphene layers [85].

Raman spectra of the characteristic G band of the prepared solvent exfoliated graphene (G_s) was found at 1570 cm^{-1} and the D band was found at 1340 cm^{-1}. The I_D/I_G ratio was found to be 0.213 indicating low population of sp^3 hybridized carbon atoms in the prepared graphene, a direct indication of the quality of the graphene sheets produced. The I_{2D}/I_G value, indicative of the thickness, was found to be 1.12, indicating the fact that the prepared graphene sheets were of few layer ones.

4.3.2 Photocatalytic Activity Studies

In the present work, ZnO/Graphene catalysts were prepared and was used in the photocatalytic degradation of cefixime antibiotic and the procedure of the degradation employed was described in the section 2.6.3 in the Chapter 2. UV-Vis spectra were collected in every 30 minute interval after the sunlight exposure of 100 ml reaction mixture with 250mg/L cefixime and 0.05g catalysts and the results are presented here.

4.3.2.1 Effect of Preparation Methods

The photocatalytic activity of H-ZnO/rGO was found to be better than M-ZnO/rGO and ZnO/G_S towards the oxidative degradation of cefixime (Figure 4.8). These results demonstrated that the ZnO/rGO prepared via hydrothermal route was far superior in catalytic performance than the ones prepared via microwave irradiation and liquid phase exfoliation. Better surface area of the catalytic support as well as the enhanced interaction between the ZnO and the hydrothermally reduced graphene oxide through the residual surface functional groups might have contributed to the enhanced performance of this photocatalyst compared to the catalytic systems fabricated by other means. The results demonstrated that the synthetic methodology employed did play a role in determining the morphology and surface area of the catalyst and ultimately decided the photocatalytic performance of the semiconductor.

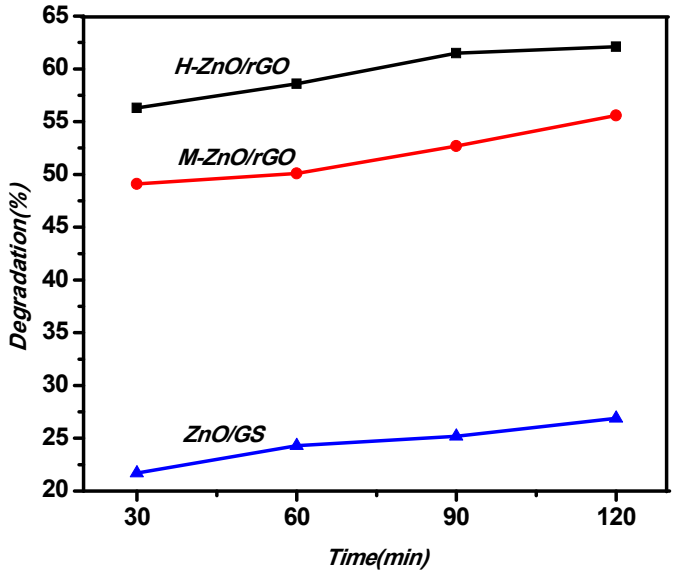

Figure 4.8: Performance of Photocatalysts Prepared by Means of Different Synthetic Strategies Towards the Oxidative Degradation of Cefixime under Sunlight Irradiation for 120 min.

4.3.2.2 Cefixime Degradation over ZnO and H-ZnO/rGO

The photocatalytic activity of the H-ZnO/rGO was observed to be far better than that of bare ZnO and the results obtained are summarised in Figure 4.9. As discussed earlier, this multifold enhancement in photocatalytic performance can be attributed to the greater carrier transport efficiency and specific surface area of the co-catalyst, reduced graphene oxide.

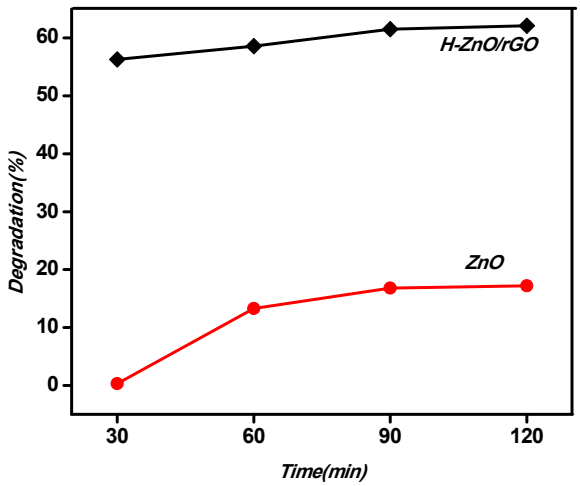

Fiqure 4.9: Performance of Different Photocatalysts Towards the Oxidative Degradation of Cefixime under Sunlight Irradiation for 120min.

4.3.2.3 Effect of Irradiation Time

The Figure 4.10 show that with increase in the irradiation time, there was an increase in the degradation efficiency especially in the initial minutes and there was no appreciable change after 120 min. Initially, cefixime was mineralised in a faster rate caused by a large number of free radicals produced in the initial minutes of the irradiation. However, when the reaction proceeds, the free radicals produced probably might have got consumed by the intermediates of the oxidative mineralisation process, so that they will be less available for the oxidation of the antibiotic molecules.

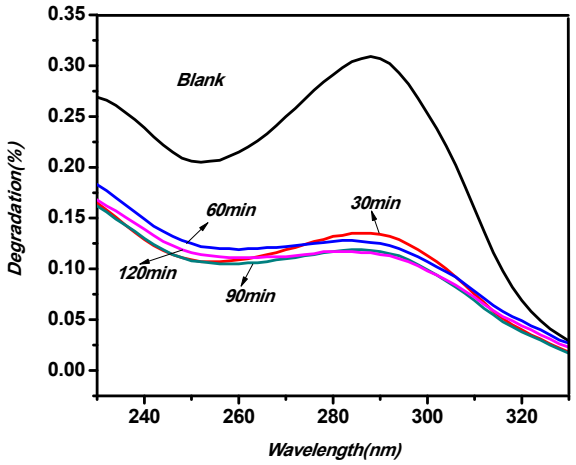

Fiqure 4.10: UV-Vis Spectra (λ_{max} = 287.5 nm) of the Reaction Mixtures after Catalyst Removal, Collected after the Sunlight Irradiation of 0,30,60, 90 and 120 Minutes of 100 ml Reaction Mixture with 250mg/L Cefixime and 0.05g H-ZnO/rGO Catalyst.

4.3.2.4 Effect of Catalyst Loading

When the catalyst weight was increased, a reduction in the photocatalytic degradation was observed which can be attributed to the possible reduction in the light intensity by the excess catalyst particles present by means of light absorption and scattering. The results obtained are summarised in Figure 4.11.

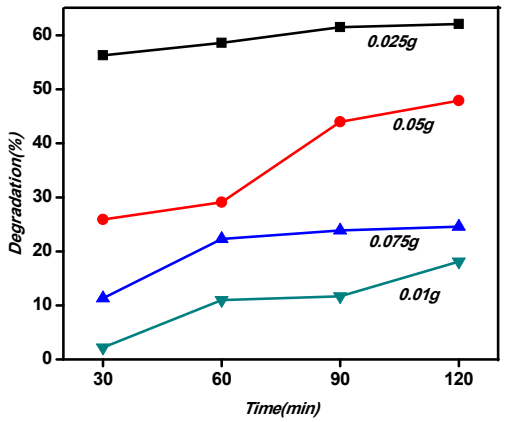

Fiqure 4.11: Optimization Studies of Catalyst Weight Carried Out under Irradiation with Sunlight

4.3.2.5 Effect of Initial Antibiotic Concentration

We have monitored the change of the photocatalytic degradation rate with different initial antibiotic concentrations by decreasing the initial cefixime concentration gradually from 250mg/L to 25mg/L employing 0.025g H-ZnO/rGO nanocatalyst and the results obtained are summarised in Figure 4.12.

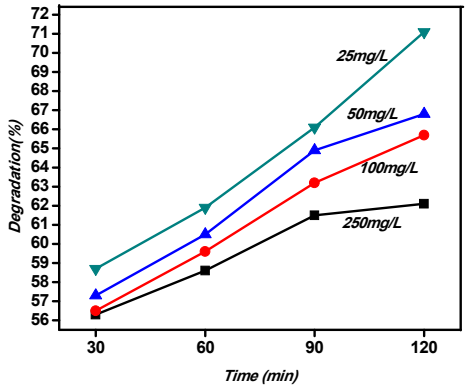

Fiqure 4.12: Effect of Initial Antibiotic Concentration

From Figure 4.12, we can observe that mineralisation process was comparatively easier when the initial concentration of the antibiotic was decreased and 71.1% degradation of the antibiotic was achieved in 120 minutes of time when the initial concentration was 25 mg/L of cefixime. Higher antibiotic concentrations are not expected in contaminated effluents.

4.3.2.6 Effect of H_2O_2 Addition

Addition of H_2O_2 in small amountsis considered beneficial for the photocatalytic degradation process since H_2O_2 is known to accelerate the oxidative degradation in two different ways. H_2O_2 can accept photo-generated electrons from the photocatalytic system to produce $OH^{\bullet}$ radicals. It can also react with the superoxide radical anions present in the reaction mixture to generate $OH^{\bullet}$ radicals. Thus, the degradation process get accelerated in the presence of H_2O_2 [86-88]. In order to explore the effect of H_2O_2 addition, the amount of H_2O_2 was varied gradually from 0 to 10 mg/L keeping all other parameters constant (250 mg/L cefixime concentration, 0.025 g H-ZnO/rGO nanocatalyst, 100 ml reaction mixture). The results obtained are shown in Figure 4.13. When 5 mg/L H_2O_2 was added, the degradation after 90 minutes of sunlight irradiation increased from 71.1% to 93.8%. However, when more concentrations of H_2O_2 present, it did not improve the degradation percentage, rather a slight decrease was observed. This can be attributed to the reaction of excess H_2O_2 with $OH^{\bullet}$ radicals which might have adversely affected the degradation process.

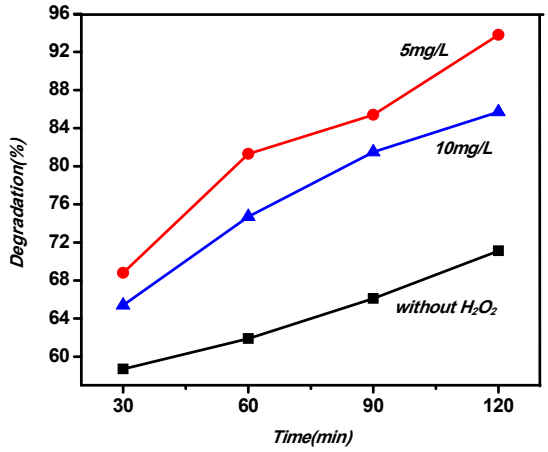

Fiqure 4.13: Effect of H_2O_2Concentration

4.3.2.7 Comparison of Degradation under 450 W High Pressure Mercury Lamp and Sunlight Irradiation

The photocatalytic activity of H-ZnO/rGO showed better performance under 450W high pressure mercury lamp than under sunlight irradiation. Under high pressure mercury lamp irradiation, the catalyst showed 88% degradation of antibiotic within the first 30 minutes itself. However, further irradiation did not result in any additional degradation. The results obtained are presented in figure 4.14. The better performance of the photocatalyst under broad band irradiation can be attributed to the higher percentage of UV radiations present in the high pressure mercury lamp spectrum.

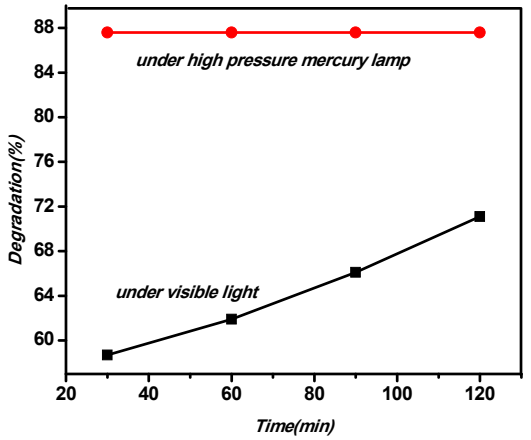

Fiqure 4.14: Degradation under 450 W High Pressure Mercury Lamp and Sunlight

4.4 Conclusions

In the present study, we demonstrated the practical applicability of photocatalytic degradation of antibiotics under exposure to sunlight, as an effective method towards the environmental cleaning up process, absolutely essential for curtailing the hazard of increasing antibiotic resistant bacterial strains. Bare ZnO catalyst was found to be not effective enough to perform the mineralization of the cefixime antibiotic under sunlight irradiation. H-ZnO/rGO nanocomposite showed better performance towards the oxidative degradation of cefixime with sunlight irradiation. A 71.1% mineralisation of the antibiotic in 25 mg/L concentration was observed within 120 minutes irradiation. The oxidative degradation rate of cefixime was found to be affected by various factors such as catalyst loading, initial antibiotic concentration, presence of H_2O_2 and so on. The H-ZnO/rGO showed better photocatalytic performance under 450W high pressure mercury lamp irradiation with 88% degradation.

References

1. S. A. Hosseini and S. Babaei, *J. Braz. Chem. Soc.*, 2017, **28**, 1-9. Doi:10.5935/0103-5053.20160176.

2. B. H. Cho, S. W. Ko, W-C. Oh and W. B. Ko, *Asian J. Chem., 2013, **25**, 5063-5067.*

3. C. Zhang, J. Zhang, Y. Su, M. Xu, Z. Yang and Y. Zhang, *Physica E Low Dimens Syst Nanostruct.,* 2014, **56**, 251–255.

4. Y. Li, G. W. Meng and L. D. Zhang, *Appl. Phys. Lett.,*2000, **76** , 2011-2013.

5. W. I. Park, J. S. Kim, G. C. Yi and H. J. Lee, *Adv. Mater.,* 2005, **17**, 1393–1397.

6. Z. Y. Fan, D. W. Wang, P. C. Chang, W. Y. Tseng and J. G. Lu, *Appl. Phys. Lett.,* 2004, **85**, 5923-5925.

7. W. I. Park, J. S. Kim, G.-C. Yi, M. H. Bae and H. J. Lee, *Appl.Phys. Lett.,* 2004, **85**, 5052–5054.

8. J. H. Choy, E. S. Jang, J. H. Won, J. H. Chung, D. J. Jang and Y. W. Kim, *Adv. Mater.*, 2003, **15**, 1911–1914.

9. L. Liao, H. B. Lu, J. C. Li, H. He, D. F. Wang, D. J. Fu, C. Liu and W. F. Zhang, *J. Phys. Chem. C.,* 2007, **111**, 1900–1903.

10. J. Chen, C. Li, G. Eda, Y. Zhang, W. Lei, M. Chhowalla, W. I. Milneand W.-Q. Deng, *Chem. Commun.,* 2011, **47**, 6084–6086.

11. J. B. Baxter, A. M. Walker, K. V. Ommering and E. S. Aydil, *Nanotechnol.*, 2006, **17,** S304-S312.

12. H. Zhang, D. Yang, X. Ma, N. Du, J. Wu and D. Que, *J. Phys.Chem. B.*, 2006, **110**, 827–830.

13. T. J. Kuo, C. N. Lin, C. L. Kuo and M. H. Huang, *Chem.Mater.,* 2007, **19**, 5143-5147.

14. D. Chen, H. Zhang, J. Z. Zhang and J. Li, *J. Phys.Chem. C.*, 2008, **112**, 8850-8855.

15. S. Cho, S. Kim, J.-W. Jang, S.-H. Jung, E. Oh, B. R. Lee and K.-H. Lee, *J. Phys. Chem.C.*, 2009, **113**, 10452-10458.

16. S. Gayathri, P. Jayabal, M. Kottaisamy and V. Ramakrishnan, *J. Appl. Phys.,* 2014, **115**, 173504 (1-7).

17. Z. Chen, N. Zhang and Y. -J. Xu, *CrystEngComm.,* 2013, **15**, 3022-3030.

18. W. Zhang, J. Zhao and X. Zou, *Korean Chem. Eng. Res.,* 2016, **54**, 127-134.

19. S. P. Chaudhari, A. B. Bodade and G. N. Chaudhari, *Korean J. Chem. Eng.,* 2013, **30**, 2001-2006.

20. Q. Li, H. Li, R. Wang, G. Li, H. Yang and R. Chen, *J. Alloys Comp.,* 2013, **567**, 1-9.

21. Y. Q. Zong, Z. Li, X. M. Wang, J. T. Ma and Y. Men, *Ceram. Int.*, 2014, **40**, 10375-10382.

22. C. J. Chang, C. Y. Lin and M. H. Hsu, *J. Taiwan. Inst. Chem. E.,* 2014, **45**, 1954-1963.

23. M. M. Ba-Abbad, A. A. H. Kadhum, A. B.Mohamad, M. S. Takriff and K. Sopian, *Chemosphere.,* 2013, **91**, 1604-1611.

24. X. L. Zhang, J. L. Zhao, S. G. Wang, H. T. Dai and X. W. Sun, *Int. J. Hydrogen. Energ.,* 2014, **39**, 8238-8245.

25. F. Peng, H. C. Zhu, H. J. Wang and H. Yu, *Korean J. Chem. Eng.,* 2007, **24**, 1022-1026.

26. A. George, S. K. Sharma, S. Chawla, M. M. Malik and M. S. Qureshi, *J. Alloys. Compd.,* 2011, **509**, 5942- 5946.

27. C. Ge, C. Xie and S. Cai, *Mater. Sci. Eng. B.,* 2007, **137**, 53-58.

28. T. Y. Ma, Z. Y. Yuan and J. L. Cao, *Eur. J. Inorg. Chem.,* 2010, **5**, 716-724.

29. M. Faisal, S. B. Khan, M. M. Rahman, A. Jamal, K. Akhtar and M. M. Abdullah, *J. Mater. Sci. Technol.,* 2011, **29**, 594-600.

30. F. L. Du, N. Wang, D. M. Zhang and Y. Z. Shen, *J. Rare Earths.,* 2010, **28**, 391-395.

31. C. Karunakaran, P. Gomathisankar and G. Manikandan, *Mater. Chem. Phys.,* 2010, **123**, 585-594.

32. L. -A. Ying, J. Liu, L. Mo, H. Lou and X. Zheng, *Int. J. Hydrogen Energy.,* 2012, **37**, 1002-1006.

33. M. Ahmad, E. Ahmed, Z. L. Hong, J. F. Xu, N. R. Khalid, A. Elhissi and W. Ahmed, *Appl. Surf. Sci.,* 2013, **274**, 273-281.

34. T. N. Lambert, C. A. Chavez, B. H. Sanchez, P. Lu, N. S. Bell, A. Ambrosini, T. Friedman, T. J. Boyle, D. R. Wheeler and D. L. Huber, *J. Phys. Chem. C*., 2009, **113**, 19812-19823.

35. G. Williams, B. Seger and P. V. Kamat, *ACS Nano.,* 2008, **2**,1487-1491.

36. H. Zhang, X. Lv, Y. Li, Y. Wang and J. Li, *ACS Nano*., 2010, **4**, 380-386.

37. L. Aia, C. Zhang and Z. Chena, *J. Hazard. Mater,* 2011, **192**, 1515-1524.

38. B. Li, T. Liu, Y. Wang and Z. Wang, *J. Colloid Interface Sci.,*2012, **377**, 114 -121.

39. S. Bai, X. Shen, X. Zhong, Y. Liu, G. Zhu, X. Xu and K. Chen, *Carbon.,*2012, **50**, 2337-2346.

40. J. T. Zhang, Z. G. Xiong and X. S. Zhao, *J. Mater. Chem.,* 2011, **21**, 3634-3640.

41. X. Liu, L. Pan, T. Lv, T. Lu, G. Zhu, Z. Suna and C. Sun, *Catal. Sci. Technol.,* 2011, **1**, 1189-1193.

42. T. Kavitha, A. I. Gopalan, K. –P. Lee, S. –Y. Park, *Carbon.,* 2012, **50**, 2994-3000.

43. H. Sun, S. Liu, S. Liu and S. Wang, *Appl. Catal. B: Environ.*, 2014, **146,** 162-168.

44. C. Han , Z. Chen , N. Zhang , J. C. Colmenares and Y. –J. Xu, *Adv. Funct. Mater.,* 2014, **25**, 221-229.

45. P. Roy, A. P. Periasamy, C.-T. Liang and H. -T. Chang, *Environ. Sci. Technol.*, 2013, **47**, 6688-6695.

46. O. Akhavan, *Carbon.,* 2011, **49,** 11-18.

47. Q. –P. Luo, X. –Y. Yu, B. –X. Lei, H. –Y. Chen, D. –B. Kuang and C. –Y. Su, *J. Phys. Chem. C.*, 2012, **116**, 8111-8117.

48. X. Bai, L. Wang, R. Zong, Y. Lv, Y. Sun and Y. Zhu, *Langmuir.*, 2013, **29**, 3097-3105.

49. O. Akhavan, *ACS Nano*., 2010, **4**, 4174- 4180.

50. B. J. Li and H. Q. Cao, *J. Mater. Chem.*, 2011, **21**, 3346-3349.

51. T. G. Xu, L. W. Zhang, H. Y. Cheng and Y. F. Zhu, *Appl. Catal. B: Environ.*, 2011, **101,** 382-387.

52. C. Z. Li, J. Y. Zhang, J. A. Yang, T. M. Wang, X. Lv and Z. L. Tang, *Appl. Catal. A: Gen.,* 2011, **402**, 80-86.

53. T. A. Saleh, M. A. Gondal, Q. A. Drmosh, Z. H. Yamani and A. Al-yamani, *Chem. Eng. J.,* 2011, **166**, 407-412.

54. Y. Yang, L. Ren, C. Zhang, S. Huang and T. Liu, *ACS Appl. Mater. Interface.,* 2011, **3**, 2779-2785.

55. S. Chakrabarti, B. Chaudhuri, S. Bhattacharjee, A.K. Ray and B.K. Dutta, *Chem. Eng. J.,* 2009, **153**, 86-93.

56. N. P. Herring, S. H. Almahoudi, C. R. Olson and M. S. El-Shall, *J Nanopart Res*., 2012, **14**, 1277-1289.

57. Y. Bu, Z. Chen, W. Li and B. Hou, *ACS Appl. Mater. Interfaces.*, 2013, **5**, 12361-12368.

58. H. Moussa, E. Girot, K. Mozet, H. Alem, G. Medjahdi and R. Schneider, *Appl. Catal. B: Environ.,*2016, **185**, 11-21.

59. I. Phillips, M. Casewell, T. Cox, B. D. Groot, C. Friis, R. Jones, C. Nightingale, R. Preston and J. Waddell, *J Antimicrob Chemother.*, 2004, **53**, 28-52.

60. J. L. Martinez, *Environ Pollut.,* 2009, **157**, 2893-2902.

61. C. H. Huang, J. E. Renew, K. L. Smeby, K. Pinkerston and D. L. Sedlak, *Water Resour Update.,* 2001, **120**, 30-40.

62. N. Tamehiro, T. Hosaka,J. Xu, H. Hu, N. Otakeand K. Ochi, *Appl Environ Microbiol.,* 2003, **69**, 6412-6417.

63. P. T. P. Hoa, S. Managaki, N. Nakada, H. Takada, A. Shimizu, D. H. Anh, P. H. Viet and S. Suzuki, *Sci Total Environ.,* 2011, **409**, 2894-2901.

64. P. Jantawasu, T. Sreethawong and S. Chavadej, *Chem. Eng. J.,* 2009, **155**, 223-233.

65. R. D. G. Cooper, *Am J Med.,* 1992, **92**, S2-S6.

66. E. P. Abraham, *Drugs.,* 1987, **34 (Suppl 2)**, 1-14.

67. H. C. Neu, *J Clin Pharrnacol.,* 1990, **30**, 396-403.

68. A. R. Khataee, M. Fathinia, S. Aber and M. Zarei, *J. Hazard. Mater.*, 2010, **181**, 886-897.

69. A. H. Abdullah, H. Jia, M. Moey and N. A. Yusof, *J. Environ. Sci.*, 2012, **24**, 1694-1701.

70. S. Ray, J. A. Lalman and N. Biswas, *Chem. Eng. J.*, 2009, **150**, 15-24.

71. L. P. Rodriguez, S. M. Cuevas, I. Oller, A. Agüera, G. L. Puma and S. Malato, *J. Hazard. Mater.,* 2012, **131,** 211-212.

72. K. Baransi, Y. Dubowski and I. Sabbah, *Water Res.*, 2012, **46**, 789-798.

73. D. Vildozo, C. Ferronato, M. Sleiman and J. M. Chovelon, *Appl. Catal. B. Environ.*, 2010, **94**, 303-310.

74. W. Zhang, Q. Zhang and F. Dong, *Ind. Eng. Chem. Res.,* 2013, **52**, 6740-6746.

75. S. K. Asl, S. K. Sadrnezhaad, M. K. Rad and D. Uner, *Turk. J. Chem.*, 2012, **36**, 121-135.

76. K. Hayat, M.A. Gondal, M. M. Khaled, S. Ahmed, A. M. Shemsid, *Appl Catal A Gen.,* 2011, **393**, 122-129.

77. J. Wang, T. Tsuzuki, B. Tang, X. Hou, L. Sun and X. Wang, *ACS Appl. Mater. Interfaces.,* 2012, **4**, 3084−3090.

78. N. Raghavan, S. Thangavel, G. Venugopal, *Mater Sci Semicond Process.,* 2015, **30**, 321–329.

79. M. Azarang, A. Shuhaimi, R. Yousefi, A. M. Golsheikh and M. Sookhakian, *Ceram. Int.,* 2014, **40**, 10217-10221.

80. T. Lv, L. Pan, X. Liu, T. Lu, G. Zhu and Z. Sun, *J. Alloys Compd.,* 2011, **509**, 10086-10091.

81. X. Li, Q. Wang, Y. Zhao, W. Wu, J. Chen and H. Meng, *J Colloid Interface Sci.,* 2013, **411**, 69-75.

82. J. Wu, X. Shen, L. Jiang, K. Wang and K. Chen, *Appl. Surf. Sci.,* 2010, **256,** 2826-2830.

83. L. Sun, R. Shao, L. Tang and Z. Chen, *J Alloys Compd.,* 2013, **564**, 55-62.

84. J. Qin, X. Zhang, Y. Xue, N. Kittiwattanothai, P. Kongsittikul, N. Rodthongkum, S. Limpanart, M. Ma and R. Liu, *Appl. Surf. Sci.,*2014, **321**, 226-232.

85. A. Ambrosi, C. K. Chua, A. Bonanni and M. Pumera, *Chem. Rev.*, 2014, **114**, 7150−7188.

86. D. F. Ollis, E. Pelizzetti and N. Serpone, *Environ. Sci. Technol.*, 1991, **25**, 1523-1529.

87. Z. Yujing and F. Ramin, *Top. Catal.*, 2006, **37**, 2-4.

88. H. T. Dyi., C. J. Lain., and H. H. Hsin., *Int. J. Photoenergy.,* 2012, Doi:10.1155/2012/328526.

Chapter 5

Preparation of TiO_2/Holey Graphene Framework (TiO_2/HGF) Nanocomposites and Their Application as Photocatalysts in Water Splitting Reaction

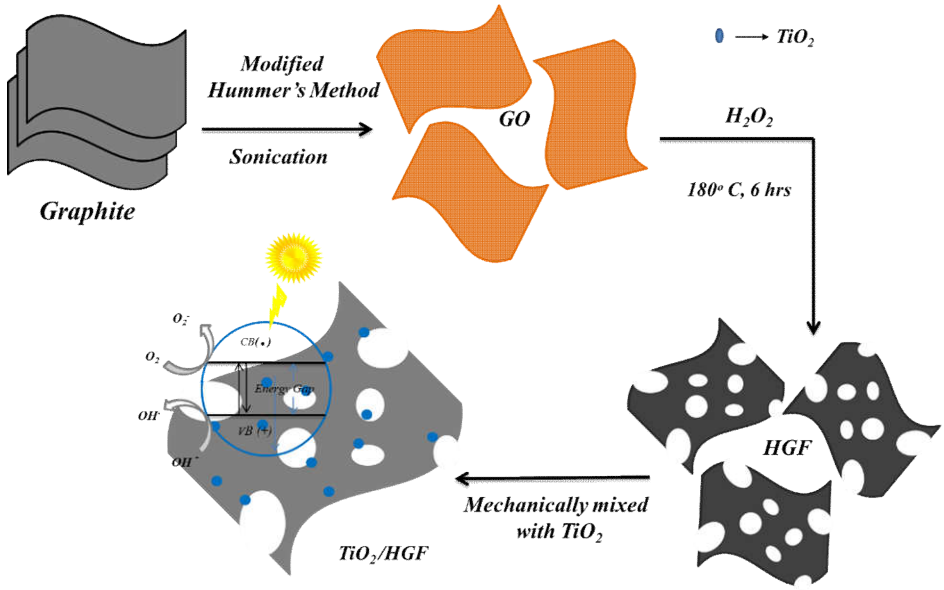

5.1 Introduction

Fossil fuels serve the energy demands of human beings for the past few centuries. However, they pose several challenges in recent years since they are non-renewable, also causing many environmental problems and are not able to remain abundant for the next generations [1]. Hydrogen fuel has been considered as an ideal solution to counter the depletion and environmental problems of fossil fuels due to various reasons such as (i) it is a clean energy source (ii) hydrogen is easier to obtain than gasoline; (iii) hydrogen produces more heat (122 MJ/kg) than gasoline (40 MJ/kg); (iv) the only product after combustion of hydrogen with O_2 is hundred percent environmentally benign material, water [2]. Generating hydrogen by utilizing the ultimate natural and free energy source such as sunlight, with the help of a photocatalyst to decompose or split water into hydrogen and oxygen is considered as a clean technology [3]. Among all semiconductor materials developed for photocatalytic applications, TiO_2 is one of the most widely used photocatalysts since it is chemically stable, environmentally-friendly, abundant and cost efficient [4]. However, TiO_2 being a wide band gap semiconductor (3.2 eV) which result in its photo-response only to UV light hindering its effective usage as a photocatalyst for hydrogen production via water splitting under solar irradiation[1]. To efficiently utilize solar energy, a large bulk of recent research has been focused on expanding the response of titania to visible region of light as well via narrowing the band gap and improving the separation efficiency of photogenerated electron-hole pairs [5-10]. Addition of sacrificial reagents and photo-sensitizer [11-13],

noble metal loading [14-16], transition metal ion doping [17,18], non-metal element doping [19,20] and coupling with secondary semiconductors [21,22], etc are some of the efforts which have been made to improve the performance of TiO_2 based photocatalysts.

Combining TiO_2 with graphene is currently considered as one of the most promising strategies in developing high performance photocatalytic systems [23]. The conjugated structure of graphene nanosheets and functional groups at their edges such as carboxyl, carbonyl etc. can enhance their interaction with the surface hydroxyl groups of TiO_2 [24]. These strong interactions are beneficial for the fast transferring of photogenerated electrons in the conduction band of TiO_2 to the graphene network, which result in an efficient electron - hole separation [24].

Holey graphene sheets have displayed excellent properties in different areas such as Li ion battery, supercapacitors, separation membranes, and so on [25-29]. As a result of the introduction of in-plane holes on the graphene sheets, the holey graphene framework (HGF) possess some unique properties. Especially, their penetrability is outstanding which is beneficial for adsorption of reactants by the composites enhancing the interactions between reactants [30]. In spite of the increased developments in the various applications of holey graphene framework, its use as part of photocatalytic systems is a novel idea and never been tried before.

In the present study, we present the preparation and characterization of a high performance TiO_2/ holey graphene photocatalyst and its effective use as a co-catalyst in the photocatalytic

water splitting reaction under the irradiation with 450W high pressure mercury lamp. For the photocatalytic water splitting reaction, we have studied the effect of various parameters such as catalyst weight, HGF loading in the catalyst and concentrations of the sacrificial agent, methanol, etc. The present study can be considered as an effective method for the production of hydrogen by water splitting reaction.

5.2 Experimental Methods

The chemicals used for the preparation of TiO_2/HGF catalysts, their suppliers and the synthetic procedure adapted have been provided in Chapter 2.

5.3 Results and Discussion

We used TiO_2/HGF nanocatalyst for the application of photocatalytic water splitting under 450W high pressure mercury lamp irradiation.

5.3.1 Catalyst Characterizations

The prepared TiO_2/HGF nanocomposite catalysts were characterized using FTIR spectroscopy, XRD, SEM, TEM and UV-Visible Diffuse Reflectance Spectral measurements and PL spectroscopic analysis.The products of the catalytic reactions were monitored using Gas Chromatography.

5.3.1.1 XRD Analysis

The XRD pattern obtained for the GO, HGF, TiO_2/HGF2, TiO_2/HGF5 and TiO_2/HGF10 nanocomposite samples are presented in Figure 5.1.

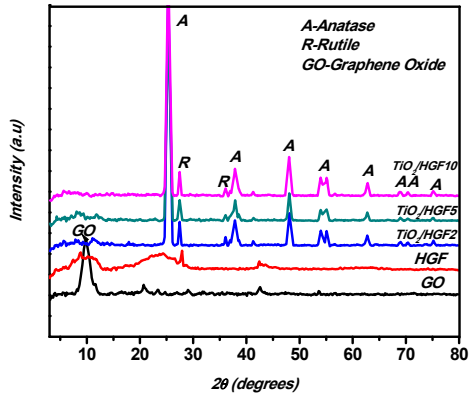

Figure 5.1: XRD Pattern for the GO, HGF, TiO_2/HGF2, TiO_2/HGF5 and TiO_2/HGF10

The XRD pattern of TiO_2/HGF nanocomposite exhibited diffraction peaks at 2θ values of 25.2°, 27.4°, 36.0°, 37.8°, 41.2°, 48.0°, 53.9°, 55.0°, 62.8°, 68.8°, 70.2° and 75.0° (figure 5.1). These main diffraction peaks indicated that the presence of anatase and rutile phases of TiO_2 and graphene in the composites. The peaks with 2θ values 25.2°, 37.8°, 48.0°, 53.9°, 55.0°, 62.8°, 68.8°, 70.2° and 75.0° can be indexed to (101), (004), (200), (105), (211), (204), (116), (220), and (215) planes of anatase. Similarly, the peaks at 27.4°, 36.0°, 41.2° belongs to (110), (101) and (111) planes of rutile phase of TiO_2 [31]. The GO peak centred on 10° corresponding to the (001) diffraction plane in the HGF suggest that the reduction of GO was not complete during the formation of holey graphene via the hydrothermal method. A new peak around 26° appeared in HGF corresponding to the (002) plane. The broadness of this peak indicated the loss of long-range ordering of

stacked carbon layers. This peak indicate that GO has been thermally reduced to RGO to some extent. In TiO_2/HGF nanocomposites all the reflections of p25 titania in which anatase as the major component (80%) and a small percentage (20%) of rutile was also present. Since the calcination temperature applied in the preparation was only 250 °C, the anatase to rutile ratio in p25 was maintained as such in the nanocomposites.

5.3.1.2 FTIR Spectral Analysis

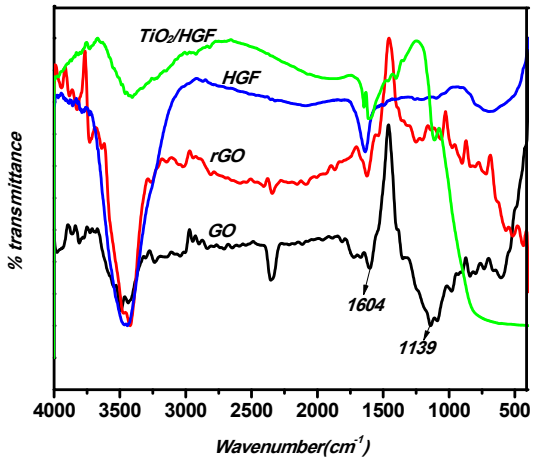

Figure 5.2: FTIR Spectra for the GO, rGO, HGF, TiO_2/HGF5

The FTIR spectra for the GO, rGO, HGF and the TiO_2/HGF5 samples are presented in Figure. 5.2. The peak at 1139 cm^{-1} can be assigned to C–OH stretching vibrations of GO which was observed to be getting systematically disappeared after the hydrothermal reduction process in the FTIR spectra of rGO, HGF and TiO_2/HGF. The broad

peak (2900 cm^{-1} to 3500 cm^{-1}) in the spectra of GO, HGF and TiO_2/HGF nanocomposite might be attributed to the O–H stretching vibration of the C–OH groups and water. The broad absorption due to the Ti-O stretching around 500 cm^{-1} was also observed in the FTIR spectrum of the TiO_2/HGF nanocomposite.

5.3.1.3 SEM Analysis

The morphologies of the prepared graphene oxide, holey graphene framework and the TiO_2/HGF nanocomposite were characterized using scanning electron microscopic analysis. In the SEM image of GO, sheets of exfoliated large area graphene oxide with lots of wringles were observed. The morphology was totally different for the holey graphene framework. Large macropores were observed in this case which makes it a good candidate for applications as catalyst support. TiO_2 with 5% HGF nanocomposite showed more of granular morphology, more or less retaining the morphology of the commercial p25 TiO_2 used. The obtained SEM images are shown in figure 5.3.

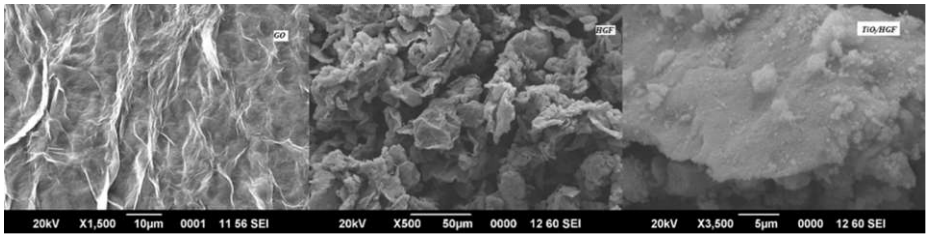

Figure 5.3: SEM Images of GO, HGF and TiO_2/HGF (TiO_2/HGF5)

5.3.1.4 TEM Analysis

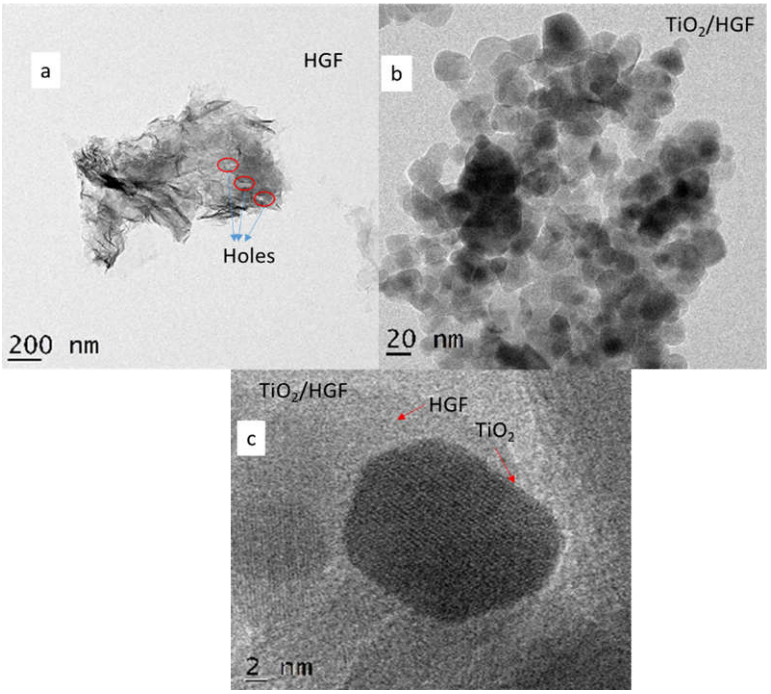

Figure 5.4: TEM Images of a) HGF and b) TiO_2/HGF and c) HRTEM Image of TiO_2/HGF

In the figure 5.4, the TEM images of HGF and TiO_2/HGF obtained are presented. Wrinkled graphene sheets with holes in the basal plane created due to the H_2O_2 etching could be observed in the TEM images and the obtained images are present in figure 5.4a. In figure 5.4b, the TEM image of TiO_2/HGF nanocomposite is presented. The titania nanoparticles were uniformly distributed over the HGF support. In the HRTEM image (figure 5.4c), the well-defined

crystalline nature of the TiO_2 nanoparticle could be observed with ordered lattice fringes.

5.3.1.5 UV-Visible Diffuse Reflectance Spectral Measurements

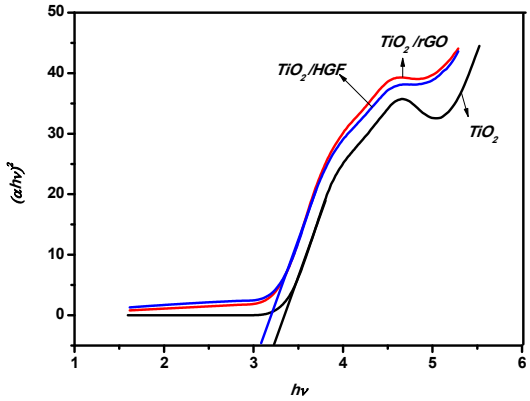

Figure 5.5: Kubelka-Munk Plots for Bare p25 TiO_2, TiO_2/rGO and TiO_2/HGF Nanocomposite Photocatalysts

The UV-Visible reflectance spectra for the prepared TiO_2/rGO, TiO_2/HGF nanocomposites and the bare Degussa p25 titania photocatalysts are provided in the figure 5.5. The spectra of both TiO_2/rGO and TiO_2/HGF nanocomposites showed slight red shifts when compared with that of bare TiO_2. The band gaps were determined from Kubelka-Munk plots obtained from UV-visible diffuse reflectance spectral measurements. From the Kubelka-Munk plots it was observed that a decrease in the band gap from 3.24 eV to 3.08eV for both TiO_2/HGF and TiO_2/rGO compared to p25 titania bringing the absorption edge to the visible region. This may be probably as a result of the presence of black coloured graphene sheets.

The formation of certain defect sites probably by carbon doping of titania is another possibility (Figure 5.5.). Band gap modification might have made the photocatalysts more visible light active.

5.3.1.6 Photoluminescence Studies

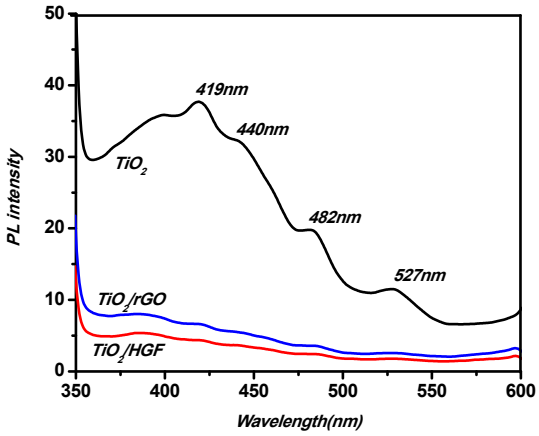

Figure 5.6: Photoluminescence Spectra for Bare p25 TiO_2, TiO_2/rGO and TiO_2/HGF Nanocomposite Photocatalysts Obtained with 320 nm Excitation.

A broad emission in the spectral range from 350 to 550 nm was observed in the photoluminescence spectra (presented in Figure 5.6) for commercial p25 titania, as well as the presence of well resolved shoulders at 419, 447, 482, and 527 nm caused by the radiative recombination of photoexcited electrons and holes [32,33]. A substantial decrease in the emission intensity was observed for TiO_2/rGO and TiO_2/HGF nanocomposites compared to bare titania, which could be attributed to the excited electron transfer from titania to graphene sheets, effectively preventing the recombination process of charge

carriers. The PL emission quenching due to the transfer of electrons to graphene network was found to be more in TiO_2/HGF nanocomposite as indicated by the intensity reduction in the PL spectra. A better linkage between the holey graphene and TiO_2 may be probably the reason behind this effective prevention of electron-hole recombinations.

5.3.2 Photocatalytic Water Splitting Studies

A series of photocatalytic water splitting experiments were carried out with the prepared catalytic systems and commercial p25 titania.The procedure of the hydrogen evolution by water splitting reaction is described in the section 2.6.4 in the Chapter 2. It was monitored by recording the gas chromatogram for every one hour interval. The experiment was continued for a total of 5 hours.

5.3.2.1 Performance of Different Photocatalysts

The plots showing the rate of hydrogen production by photocatalytic water splitting with irradiation time when different photocatalysts employed are provided in figure 5.7. Both TiO_2/HGF and TiO_2/rGO nanocomposites were found to be more powerful photocatalysts than p25 titania. A maximum of 2.3 mmol/g/h of hydrogen production was observed in the case of TiO_2/HGF. This enhanced photocatalytic activity could be attributed to the uniform distribution of TiO_2 on holey graphene sheets, large surface area and unique properties of holey graphene framework. It was observed that the hydrogen production rate kept on decreasing for the entire 5 hour period observed. That is, more hydrogen production was observed in

the first hour in this case. On the other hand, in the case of TiO_2/rGO nanocomposite, the hydrogen production rate increased slightly after the first hour. A maximum of 0.871 mmol/g/h of hydrogen production was observed in the second hour. TiO_2/rGO nanocomposite also showed better photocatalytic performance than commercial p25 titania calcined at 250°C. However, the performance was far inferior to the TiO_2/HGF system, probably because the binding of graphene and titania was less efficient compared to TiO_2/HGF nanocomposite. With the p25 titania catalyst without graphene, the evolution of hydrogen was very less in the first three hours. The hydrogen production gradually picked up in the fourth hour and a maximum of 0.630 mmol/g/h was observed. In the fifth hour, the hydrogen production rate was again reduced slightly. In the absence of graphene, electron hole recombinations must have taken place much more effectively which might have reduced the hydrogen production rate substantially. This argument was also supported by the PL measurements as well.

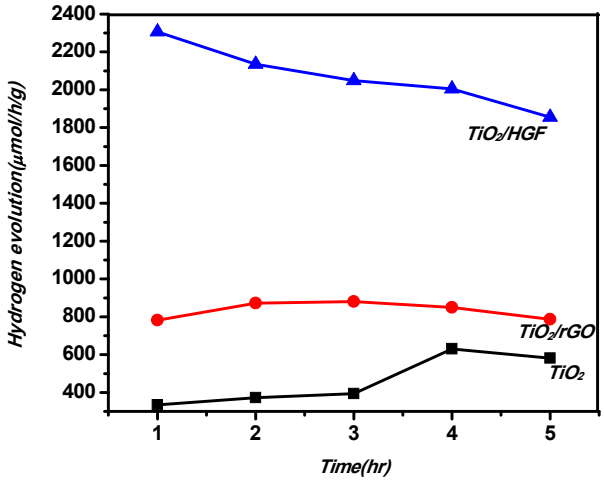

Figure 5.7: Performance of Different Photocatalysts Towards Water Splitting

5.3.2.2 Effect of Catalyst Weight

The effect of catalyst weight on the hydrogen production was studied by varying the catalyst weight alone keeping all the other parameters of the reaction constant. Three different amounts of the catalyst TiO_2/HGF nanocomposite with % HGF (0.2 g, 0.25 g and 0.3 g) with 10 ml methanol as sacrificial agent and 40 ml water was taken for the hydrogen production experiment. The hydrogen production rate was observed to increase with an increase in the amount of the catalyst from 0.2 g to 0.25 g under broad band irradiation with high pressure mercury lamp. A further increase in catalyst weight to 0.3 g resulted in a substantial decrease in hydrogen production rate. The production was maximum when the catalyst weight was 0.25 g. The results obtained are summarized in figure 5.8.

The hydrogen production rate was supposed to increase with amount of catalyst owing to the presence of more photo-excitation centers. However, with more loading, the dispersed catalyst particles made the dispersion opaque and the light intensity got reduced in water mainly because of the light absorption and scattering caused by the suspended catalyst particles, as described by Beer–Lambert Law, ultimately affected the photocatalytic process adversely.

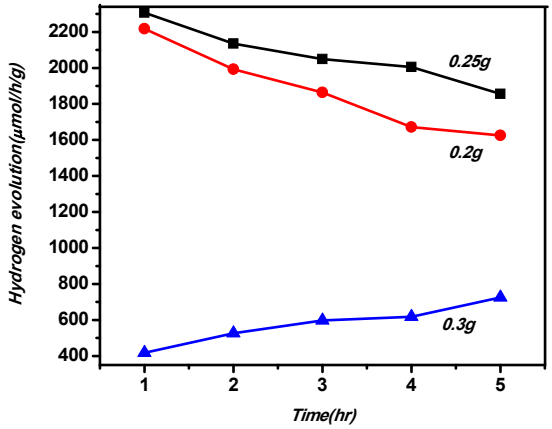

Figure 5.8: Effect of Catalyst Weight on Hydrogen Evolution Using TiO_2/HGF5 Catalyst

5.3.2.3 Effect of Graphene Loading in the Photocatalysts

The photocatalytic water splitting reactions were carried out with different nanocomposite catalytic systems which differ in holey graphene loading and the results obtained are presented in the figure 5.9. TiO_2/HGF (5%) was observed to be the photocatalyst which showed the best performance than TiO_2/HGF (2%) and TiO_2/HGF

(10%). Even though the presence of holey graphene framework was found to be beneficial by many ways for photocatalytic activity, excess HGF can mask the TiO_2 nanoparticle surfaces, which will ultimately reduce the performance of the photocatalytic system.

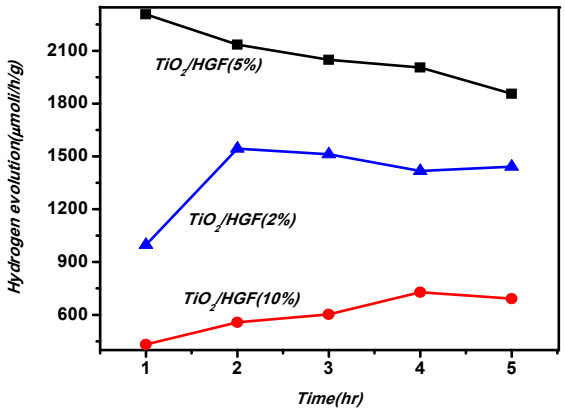

Figure 5.9: Effect of Graphene Loading in the Photocatalysts

5.3.2.4 Effect of Amount of Sacrificial Agent

Sacrificial agents act as electron donors due to their ability to react with photogenerated holes. Photocatalytic reactions were carried out with TiO_2/HGF taking 0.25 g catalyst weight varying the water methanol ratios and the results obtained are provided in the figure 5.10. The hydrogen production rate was the best when the methanol: water ratio was maintained as 1:4. Further increasing of methanol: water ratio decreased the hydrogen production rate as shown in the figure 5.10. When the initial concentration of the sacrificial reagent used was excess, the hydrogen production rate was found to be lowered probably

due to the surface blocking of the catalyst by the molecules of sacrificial agent. 10 ml methanol and 40 ml water mixture gave the best results.

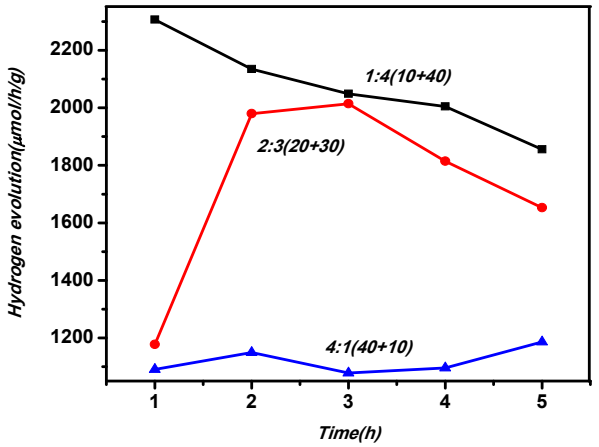

Figure 5.10: Effect of Amount of Sacrificial Agents on Hydrogen Evolution

5.4 Conclusions

In the present study, we have developed efficient photocatalysts capable of generating hydrogen under 450 W high pressure mercury lamp irradiation via photocatalytic water splitting reaction. The photocatalytic water splitting was studied by varying various parameters of the reaction such as catalyst weight, HGF loading in the catalyst and concentration of the sacrificial agent, etc. With holey graphene titania nanocomposite, we could achieve a maximum of 2.306 mmol/g/h of hydrogen production rate which was definitely a promising value. The present study demonstrated that HGF can be a suitable co-catalyst in the titania based photocatalytic systems, especially for the photocatalytic water splitting reaction.

References

1. L. Shou-Heng and S. Han-Ren, *Appl. Energy.*, 2012, **100**, 148-154.

2. H. Chao-Wei, L. Chi-Hung, J. CS Wua, L. Yu-Chang, C. Chun-Ling, W. Chih-Hung, A. Masakazu, M. Masaya and T. Masato, *Int. J. Hydrogen. Energy.*, 2010, **35**, 12005-12010.

3. A. Fujishima and K. Honda, *Nature.*, 1972, **238**, 37- 44.

4. M. Anpo, S. Dohshi, M. Kitano, Y. Hu, M. Takeuchi and M. Matsuoka, *Ann. Revi. Mater. Res.*, 2005, **35**, 1-27.

5. A. Belhadi, S. Boumaza and M. Trari, *Appl. Energy.*, 2011, **88**, 4490-4495.

6. A. Kudo and Y. Miseki, *Chem. Soc. Rev.*, 2009, **38**, 253-278.

7. S. P. Xu and D. D. Sun, *Int. J. Hydrogen. Energy.,* 2009, **34**, 6096-6104.

8. G. S. Shao, F. Y. Wang, T. Z. Ren, Y. Liu and Z. Y. Yuan, *Appl. Catal. B. Environ.*, 2009, **92**, 61-67.

9. T. Sreethawong, S. Laehsalee and S. Chavadej, *Int. J. Hydrogen. Energy.*, 2008, **33**, 5947-5957.

10. A. Z. Jurek, E. Kowalska, J. W. Sobczak, W. Lisowski, B. Ohtani and A. Zaleska, *Appl. Catal. B. Environ.,* 2011, **101**, 504-514.

11. Y. Q. Wu and G. X. Lu, *Catal. Lett. A.*, 2009, **133**, 97-105.

12. V. Gombac, L. Sordelli, T. Montini, J. J. Delgado, A. Adamski, G. Adami, M. Cargnello, S.Bernal and P. Fornasiero, *J. Phys. Chem.*, 2010, **114**, 3916-3925.

13. D. Chatterjee, *Catal. Commun.*, 2010, **11**, 336-339.

14. L. Kannekanti and K. R. Jakkidi, *Int. J. Hydrogen. Energy.*, 2010, **35**, 3991-4001.

15. Y. Y. Wen, H. M. Ding and Y. K. Shan, *Nanoscale.*, 2011, **3**, 4411-4417.

16. B. Neppolian, A. Bruno, C. L. Bianchi and M. Ashokkumar, *Ultrason.Sonochem.,* 2012, 19, 9-15.

17. M. Gratzel and R. F. Howe, *J. Phys. Chem.*, 1990, **94**, 2566-2572.

18. Y. Choi, A. Termin and M. R. Hoffmann, *J. Phys. Chem.*, 1994, **98**, 13669-13679.

19. K. X. Song and J. H. Zhou, *J. Am. Ceram. Soc.*, 2008, **91**, 1369-1371.

20. X. Y. Zhang and Y. J. Sun, *Int. J. Hydrogen. Energy.*, 2012, **37**, 811-815.

21. H. Wang, L. Zhang, Z. Chen, J. Hu, S. Li, Z. Wang, J. Liu and X. Wang, *Chem. Soc. Rev.***,** 2014, **43**, 5234-5244.

22. S. Thammanoon and Y. Susumu, *Mater. Res. Bull.*, 2012, **47**, 1385-1395.

23. Y. Zhang, Z. –R. Tang, X. Fu and Y. –J. Xu, *ACS Nano.*, 2010, **4**, 7303–7314.

24. Q. J. Xiang, J. G. Yu and M. Jaroniec, *Nanoscale.*, 2011, **3**, 3670-3678.

25. S. Yang, X. Feng and K. Müllen, *Adv. Mater.*, 2011, **23**, 3575-3579.

26. M. L. Gethers, J. C. Thomas, S. Jiang, N. O. Weiss, X. Duan, W. A. Goddard and P. S. Weiss, *ACS Nano.*, 2015, **9**, 10909-10915.

27. X. H. Lv, W. Lv, W. Wei, X. Y. Zheng, C. Zhang, L. J. Zhi and Q. H. Yang, *Chem. Commun.*, 2015, **51**, 3911-3914.

28. H. Wang, X. L. Zheng, H. N. Chen, K. Y. Yan, Z. L. Zhu and S. H. Yang, *Chem. Commun.*, 2014, **50**, 7517-7520.

29. Z. Q. Jiang, Z. J. Jiang, X. N. Tian and W. H. Chen, *J. Mater. Chem. A*, 2014, **2**, 441-450.

30. C. Xu, X. He, C. Wang, X. Chen, R. Yuan and W. Dai*, RSC Adv.*, 2016, DOI: 10.1039/C6RA17603H.

31. N. K. Muhammad and B. Javaid, *Sci. Res.*, 2011, **2**, 962-965.

32. Y. Shweta and J. Gautam, *J. Chin. Chem. Soc.,* 2017, **64**, 103-116.

33. Y. Shweta, S MeenaKumari, K. V. Devendra and J. Gautam, *Adv. Nano. Energy.*, 2017, **1**, 73-89.

Chapter 6

TiO_2/Nitrogen Doped Holey Graphene (TiO_2/NHG) Nanocomposite and Its Photocatalytic Applications

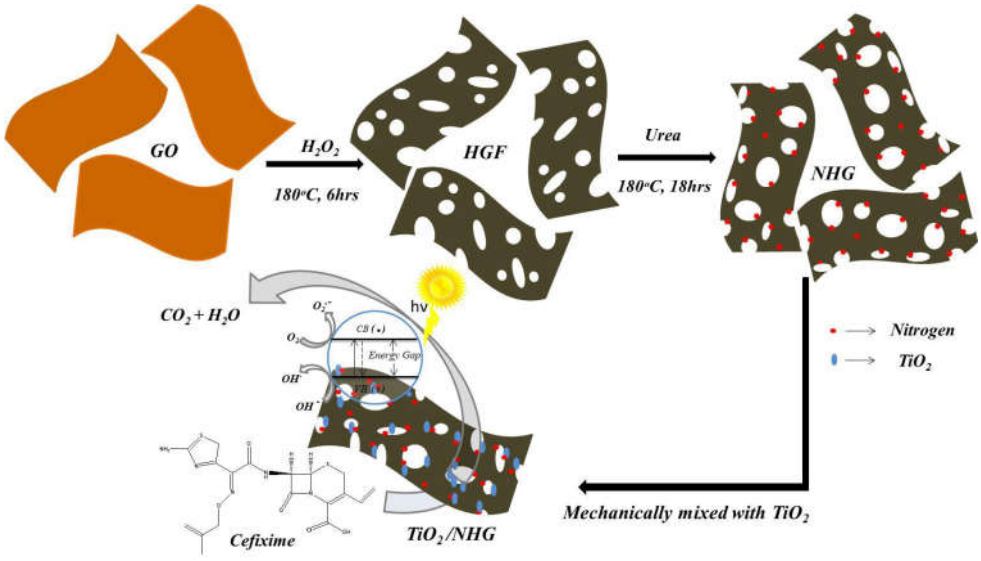

6.1 Introduction

Heterogeneous photocatalysis using titania-based catalytic systems have been considered as an environmentally friendly technology for pollutant removal [1-15]. As described in the previous chapter, the popularity of titania as a heterogeneous photocatalyst can be attributed to its chemical stability, non-toxic nature, abundance, and cost effectiveness. There are two important factors which can adversely affect the performance of titania as a photocatalyst, harvesting sunlight. The first is the rapid recombination of photogenerated electrons and holes before reaching the surface. Secondly, because of the comparatively high band gap, titania absorb mainly in the UV region leaving the abundant, visible portion of sunlight. Many researchers have addressed the recombination problem by employing various dopants which act as a sink for the photogenerated electron, thus reducing the recombination rates of electrons and holes. Incorporation of noble metal nanoparticles and doping with carbon nanomaterials such as graphene and carbon nanotubes have been shown to significantly reduce the recombination of charge carriers and enhance the photocatalytic activity, in comparison with bare titania [16]. Graphene possesses many advantages including better conductivity and high surface area and this can be increased even further by the use of the holey graphene network [17-21]. In recent years, there is an increasing interest in these highly porous holey graphene networks and the catalytic systems in which the catalytically active materials are dispersed on the surfaces of the holey graphene networks [17]. Their superior performance has been attributed to their enormous surface area [17-21]. Nitrogen doping of holey graphene further improves its catalytic properties [22, 23]. Moreover, doping with

nitrogen also modifies the band gap of titania, extending its optical absorption into the visible region making it better suited for harvesting solar energy [13].

As we have seen in chapter 4, antibiotic contamination of the water bodies as a result of their uncontrolled use and abuse poses a serious environmental threat. Their presence can result in the development of antibiotic resistant microbes, posing a serious hazard for the entire humanity in the coming years [24-30]. The high consumption rates of antibiotics and their continuous release into the environment will eventually result in the proliferation of bacterial strains that are resistant to a wide spectrum of antibiotics. Even if present in low concentrations, they cause a concern because most of the antibiotics have low biodegradability and are difficult to be removed by conventional methods for waste water treatment [31]. Thus, there is an urgent need to develop efficient methods for their mineralization from various effluents [32, 33]. The present work is aimed in this direction.

Cefixime is a third generation antibiotic that comes under the category of extended spectrum cephalosporins (ESCs) [34, 35]. Its chemical formula can be written as (6R, 7R)-7[(Z)-2-(2-amino-4-thiazolyl)-2-(carboxymethoxyimino]-acet-amido)-8-oxo-3-vinyl-5-thia-1- azabicyclo (4, 2, 0) octa-2-ene-2 carboxylic acid. Cephalosporin drugs act in a way similar to that of penicillin, inhibiting the enzymes that are required for the synthesis of the cell wall of bacteria in combination with the penicillin binding proteins (PBPs). Cefixime is an antibiotic effectively used against infections caused by a wide spectrum of bacteria including Pseudomonas aeruginosae, Neisseria gonorrhoeae, Streptococcus aureus,

Streptococcus pneumoniae, etc. In particular, ESCs are considered as the only single antibiotic that is effective in the treatment of the sexually transmitted disease gonorrhoea and is currently in use in most of the countries. In fact, a recent press release of the World Health Organization reveals that the resistance to cefixime has been reported in more than 50 countries now [36]. This poses a serious concern in the sphere of public health [29, 30].

In order to remove antibiotics from the wastewater, a number of processes are currently in use, including different advanced oxidation processes, ion exchange, adsorption onto activated carbon, reverse osmosis [32,33,1-15] etc. Compared to other processes, advanced oxidation processes used in the treatment of pharmaceutical waste water are more preferred, because a complete oxidative degradation of the pollutants can be achieved by these methods whereas in some of the other methods, the pollutants are merely being transferred from one phase to another and their total removal does not happen. Advanced oxidation methods include chemical oxidation using ozone, synergic oxidation with O_3 and H_2O_2, as well as photocatalytic degradation, assisted by various semiconductor catalysts [37-40]. For example, Visalakshi et al. reported the photocatalytic degradation of cefixime using nano-crystalline ZnO under UV light irradiation [41]. In a similar study, Pourtaheri et al. used NiO/nanoclinoptilolite (NiO/NCP) catalyst under mercury-lamp irradiation for the photocatalytic degradation of cefixime; with a maximum of 70% degradation in 300 minutes at pH 5 [42]. Shooshtari et al. have employed a hydrothermally prepared ZnO/Fe_2O_3 nanocomposite as photocatalyst for advanced oxidation of cefixime, with the simultaneous use of UV and Visible lamps and

reported 99.1% degradation in 127 minutes [43]. In another semiconductor based oxidative removal of cefixime, Almasi et al. achieved 83.3% degradation in a UV/WO_3 process with a catalyst dose of 200 mg/L in an irradiation time of 100 minutes at a cefixime concentration of 40 mg/L [44].

The photocatalytic hydrogen production via water splitting reaction is an environmentally friendly process, where hydrogen is produced from two abundantly renewable sources, i.e. water and solar energy, with the aid of photocatalysts [45-55]. In the previous chapter the preparation of TiO_2/HGF nanocomposites and their application as photocatalysts for the water-splitting reaction has been presented in detail. Here, the same reaction has been studied again by modifying the photocatalytic system by the nitrogen doping of the holey graphene framework employed as the co-catalyst.

In the present chapter, we present the preparation and characterization of a high performance TiO_2/nitrogen-doped holey graphene hybrid photocatalyst (designated as TiO_2/NHG) and its effective use in the oxidative degradation of cefixime in sunlight as well as the photocatalytic water splitting reaction under 450W high pressure mercury lamp. For the photocatalytic degradation of antibiotic reaction, we studied the effect of various parameters such as catalyst loading, initial antibiotic concentration, presence of H_2O_2 and recyclability of the nanocatalyst. For the water splitting reaction, we have also studied the various parameters such as catalyst weight, NHG loading in the catalyst and concentration of the sacrificial agent, methanol, etc.The antibiotic mineralisation study can be considered as a step towards photocatalytic waste water purification employing

sunlight as an effective source of energy in the battle against antibiotic resistant microbes. However, the study of generation of hydrogen by water splitting reaction under broad band irradiation, the nitrogen doping of the co-catalyst, holey graphene framework, is found to be not so beneficial. Nevertheless, from our antibiotic degradation studies, it is established that the present photocatalytic system is highly efficient in solar energy harvesting and performs better compared to TiO_2/HGF photocatalyst under solar irradiation.

6.2 Experimental Methods

The chemicals used for the preparation of TiO_2/NHG catalyst, their suppliers and the synthesis process are mentioned in the Chapter 2.

6.3 Results and Discussion

We used TiO_2/NHG nanocatalyst for the applications of photocatalytic degradation of Cefixime antibiotic in the presence of sunlight and photocatalytic water splitting under 450W high pressure mercury lamp.

6.3.1 Catalyst Characterizations

In order to examine the effect of dispersion of titania on nitrogen doped holey graphene surface, the prepared catalysts were characterized using FTIR spectroscopy, XRD, SEM, TEM, CHNS analysis, UV-Visible Diffuse Reflectance Spectral Measurements and PL spectroscopic analysis.The products of the catalytic reactions were

confirmed using Ultraviolet-Visible Absorption Spectroscopy and Total organic carbon (TOC) analysis.

6.3.1.1 XRD Analysis

The XRD patterns obtained for the GO, RGO, HGF, NHG and TiO_2/NHG nanocomposite samples are presented in Figure 6.1.

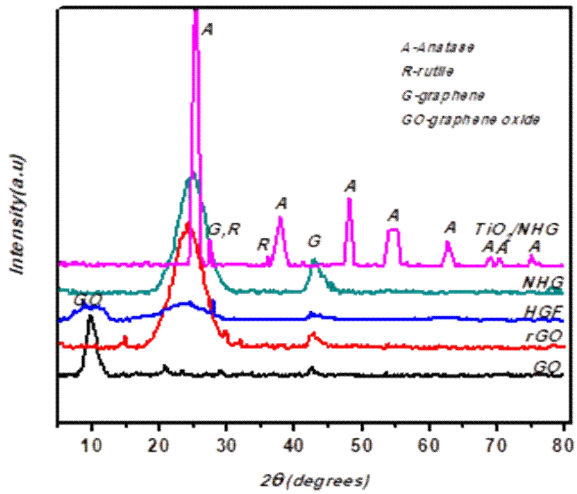

Figure 6.1: XRD Pattern for the GO, rGO, HGF, NHG and TiO_2/NHG.

The XRD of TiO_2/NHG exhibited diffraction peaks at 2θ values of 25.2°, 27.4°, 36.0°, 37.8°, 41.2°, 48.0°, 53.9°, 55.0°, 62.8°, 68.8°, 70.2° and 75.0° which could be readily indexed to the mixture of anatase and rutile phases of TiO2 and graphene. The peaks position of 25.2°(101), 37.8°(004), 48.0°(200), 53.9°(105), 55.0°(211), 62.8°(204),68.8° (116), 70.2° (220), 75.0° (215) corresponds to anatase and the ones at 27.4°(110), 36.0°(101), 41.2° (111), for rutile phase of TiO_2 [56]. The characteristic peak for the GO, which was centered around

10°, corresponding to the (001) diffraction plane, did not disappear completely after the hydrothermal reduction and the holey graphene framework formation indicating that reduction of GO in the hydrothermal conditions was not complete. However, the characteristic graphite peak centered around 26° in the corresponding to the (002) plane of graphene also appeared in HGF and NHG, indicating the reduction of oxygen moieties in GO to some extent. The presence of oxygen containing moieties still remaining at the edges of holey graphene sheets did not allow the d- spacing to become lower. Sharper peaks were observed for the NHG sample revealing better crystallinity. The TiO_2/NHG nanocomposite showed all the reflections of p25 titania (80% anatase and 20% rutile) and here also the calcination temperature was only 250°C, not sufficient enough to cause the anatase to rutile transition, the anatase to rutile ratio in the nanocomposite was more or less the same of that of p25 titania.

6.3.1.2 FTIR Spectral Analysis

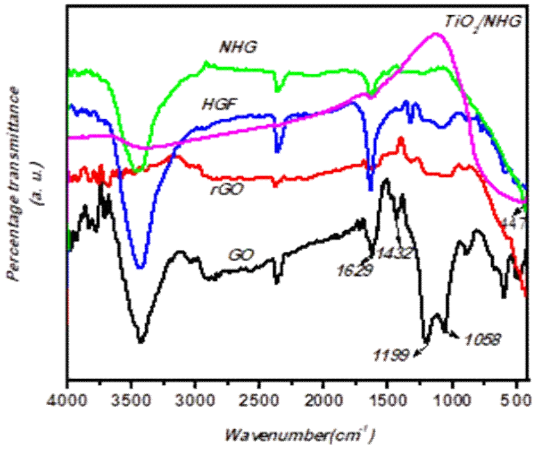

Figure 6.2: FTIR Spectra for the GO, rGO, HGF, NHG and the TiO_2/NHG Samples

The FTIR spectra for the GO, rGO, HGF, NHG and the TiO_2/NHG samples are presented in Figure. 6.2. The peaks corresponding to different oxygen functionalities were present in the spectrum of GO such as C-OH stretch at 1199 cm^{-1}, and C-O-C stretch at 1058 cm^{-1}. However, after the hydrothermal reduction, these peaks of oxygen functionalities in the FTIR spectra of rGO, HGF and NHG process got gradually disappeared or diminished in intensity. The Ti-O stretch was observed at 447 cm^{-1} in the FTIR spectrum of TiO_2/NHG nanocomposite.

6.3.1.3 SEM Analysis

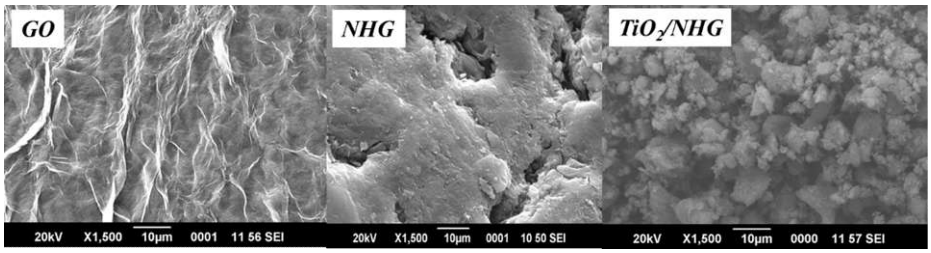

Figure 6.3: SEM Images of GO, NHG and TiO_2/NHG

The morphological studies of the samples were carried out using scanning electron microscopy. The Graphene oxide sample exhibited more layered morphology as observed from the SEM image (as already discussed in the previous chapter). The SEM images of the NHG (figure 6.3) revealed the presence of large macro-pores, which were absent in the parent GO, probably created as a result of the H_2O_2 etching. TiO_2/NHG catalyst showed more granular morphology. The change from the layered morphology to more rough granular

morphology indicated successful incorporation of titania nanoparticles on the nitrogen doped holey graphene sheets.

6.3.1.4 TEM analysis

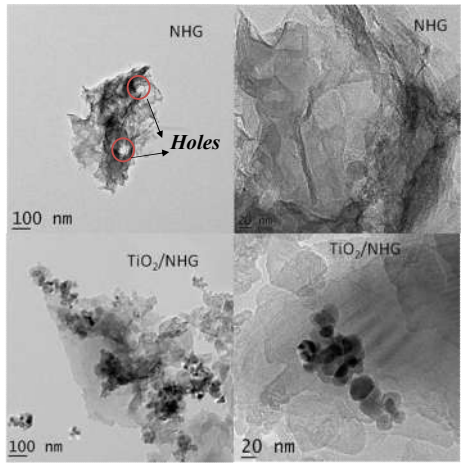

Figure 6.4: TEM Images of NHG, TiO_2/NHG and HRTEM Image of the TiO_2Particles on NHG

The TEM image of the NHG as shown in Figure 6.4 revealed the presence of many in plane holes with irregular shapes in the graphene sheet (shown in the circles in figure 6.4a.). The formation of these holes can be attributed to the oxidative etching process happened in the hydrothermal treatment due to the presence of dilute H_2O_2, resulting in partial detachment and removal of carbon atoms from the graphene sheet and eventually producing the holey structure. The TEM image of the TiO_2/NHG nanocomposite showed that the titania nanoparticles were loaded on the holey graphene sheets and they were dispersed well on the surface.

6.3.1.5 UV-Visible Diffuse Reflectance Spectral Measurements

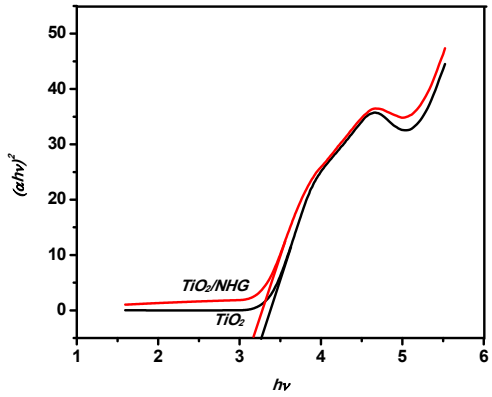

Figure 6.5: Kubelka-Munk Plots for Bare p25 TiO_2 and TiO_2/NHG Nanocomposite Photocatalysts

The UV-Visible reflectance spectra for the prepared TiO_2/NHG nanocomposite and the bare Degussa p25 titania photocatalysts were measured and it was found that the absorption edge showed a slight red shift when the spectrum of TiO_2/NHG was compared with that of bare TiO_2. The band gaps were determined from Kubelka-Munk plots (figure 6.5) obtained from UV-visible diffuse reflectance spectral measurements. Kubelka-Munk plots revealed a decrease in the band gap from 3.2 eV to 3.17eV for TiO_2/NHG compared to p25 bringing the absorption to the visible region. Probably as a result of nitrogen doping in the holey graphene sheets. Band gap modification made the photocatalyst more sunlight active.

6.3.1.6 Photoluminescence Studies

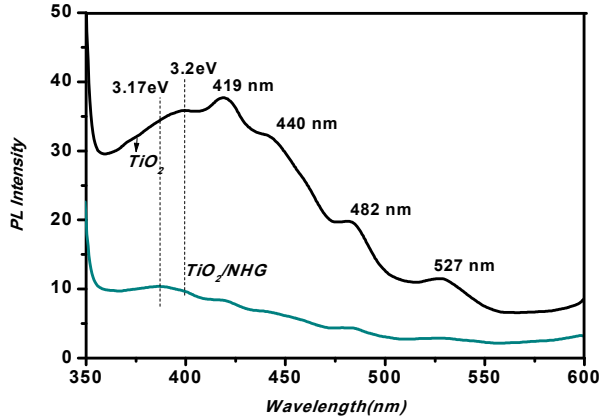

Figure 6.6: Photoluminescence Spectra for Bare p25 TiO_2 and TiO_2/NHG Nanocomposite Photocatalysts Obtained with 320 nm Excitation.

In the photoluminescence spectra (presented in Figure 6.6), for p25 titania, as already discussed in the previous chapter, a broad emission in the spectral range from 350 to 550 nm was observed with well resolved shoulders at 419, 447, 482, and 527 nm which can be attributed to the recombination of photoexcited electrons and holes causing emission of radiations [57, 58]. The emission intensity was substantially decreased for TiO_2/NHG caused by the excited electron transfer from the titania to graphene sheets, which effectively prevented the recombination of electrons and holes.

6.3.1.7 CHNS Analysis

Table 6.1: Elemental % from CHNSAnalysis of NHG

Catalyst	N%	C%	H%
Nitrogen doped holey graphene (4.48mg)	**16.34**	**59.63**	**1.73**

The results of elemental analysis of the NHG nanocomposite obtained are given in Table 6.1 which revealed that 16.34% of nitrogen was present in NHG which confirmed the effective nitrogen-doping of the holey graphene framework by the hydrothermal treatment with urea.

6.3.1.8 XPS Analysis

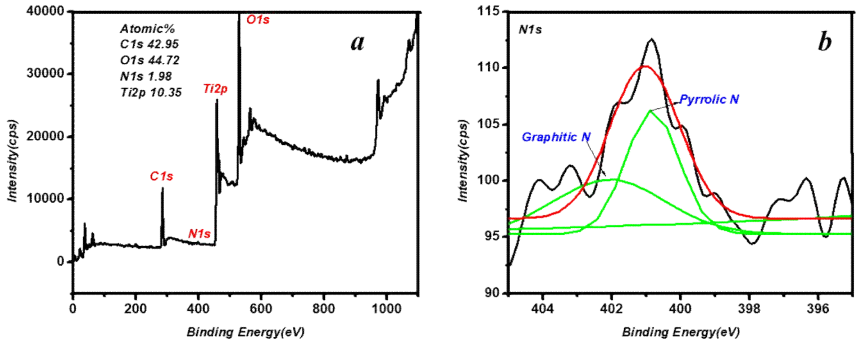

Figure 6.7: (a) XPS Survey Spectrum of TiO_2/NHG Nanocomposite; (b) Deconvoluted Spectra of the N1s Region.

The elemental composition of the TiO_2/NHG nanocomposite was also investigated using X-ray photoelectron spectroscopy (XPS) and the results were presented in Figure 6.7. The survey spectrum (0-1100 eV) of TiO_2/NHG showed mainly peaks corresponding to carbon (C 1s), oxygen (O 1s), Nitrogen (N1s) and Titanium (Ti 2p) having atomic concentrations 42.96%, 44.72%, 1.98% and 10.35% respectively (Figure 6.7a). The de-convoluted spectrum of the N1s region (Figure 6.7b.) showed that the Nitrogen was mainly of graphitic (56%) and pyrrolic (44%) type. The higher electronegativity of graphitic N atoms compared to the adjacent C nuclei reduces the electron density on the adjacent carbon atoms, which causes electrons

transfer from the adjacent C to N atoms, and the nitrogen can back donate its lone pair of electrons to the adjacent C pz orbitals. Thus, the graphitic N atoms in general improve the conductivity of the graphene[59]. On the other hand, the pyrrolic N is basically p-doping. However, pyrrolic N at the edges of graphene are capable of acting as the catalytic-reaction activation centers which again enhance the catalytic performance.

6.3.2 Photocatalytic Studies

6.3.2.1 Photocatalytic Degradation of Cefixime Antibiotic

UV-Vis spectra were collected in every 15 minute interval after the sunlight exposure of 100 ml reaction mixture with 250 mg/L cefixime and 0.05 g TiO_2/NHG catalyst and the results are presented in Figure 6.8.

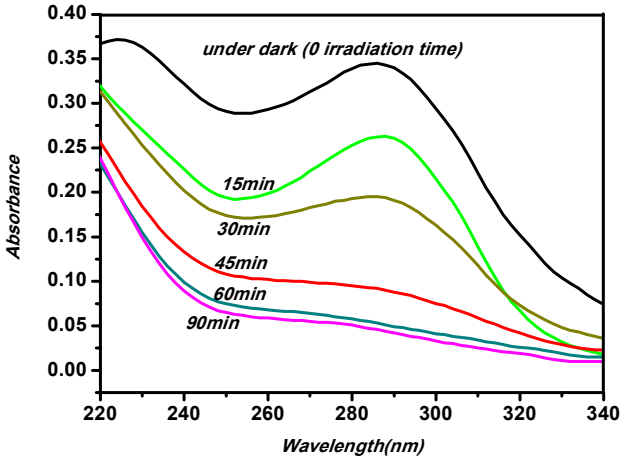

Figure 6.8: UV-Vis Spectra (λ_{max} = 287.5 nm) of the Reaction Mixtures after Catalyst Removal, Collected after the Sunlight Irradiation of 0, 15, 30, 45, 60 and 90 Minutes of 100 ml Reaction Mixture with 250mg/L Cefixime and 0.05g TiO_2 /NHG Catalyst

The results showed that with increase in the irradiation time of the antibiotic with the catalyst and sunlight exposure, there was an increase in the degradation efficiency. As observed from the figure 6.8, half of the degradation happened in the initial 30 minutes and thereafter removal process slowed down. A probable explanation for this was as follows. Initially, cefixime was oxidized in a faster rate because of the presence of large number of free radicals produced in the beginning. However, as the reaction proceeded further, the intermediates produced increasingly got consumed the free radicals, so that they will be less available for the oxidation process [60].

In order to quantitatively monitor the mineralization process of cefixime, we performed the total organic carbon (TOC) measurements and the results obtained are summarized in Figure 6.9. The % reduction in TOC values differed from the % reduction obtained from the absorbance values of cefixime that were observed at 30 minutes and 60 minutes irradiation time. This implies the formation of transient organic intermediates during the mineralisation process. However, with after irradiation for 90 minutes, the % degradation obtained from the UV spectra was very close to the % decrease in TOC, indicating the complete mineralisation of the antibiotic.

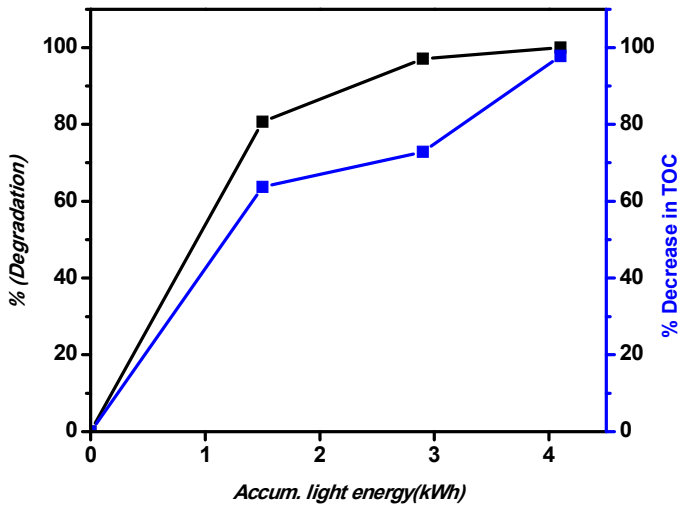

Figure 6.9: Plots of % Degradation Obtained from the Absorbance Measurements and %Decrease in TOC Against Accumulated Light Energy.

6.3.2.1.1 Comparison of Performance of Different Catalysts

The photocatalytic activity of the TiO_2 /NHG was observed to be better than that of bare p25 TiO_2, TiO_2/rGO, and TiO_2/HGF towards the oxidative degradation of cefixime (Figure 6.10). These results demonstrated that the morphology and surface area of the catalyst support as well as heteroatom doping capable of band gap modification such as that of nitrogen were among the important factors which determined the photocatalytic performance of a semiconductor.

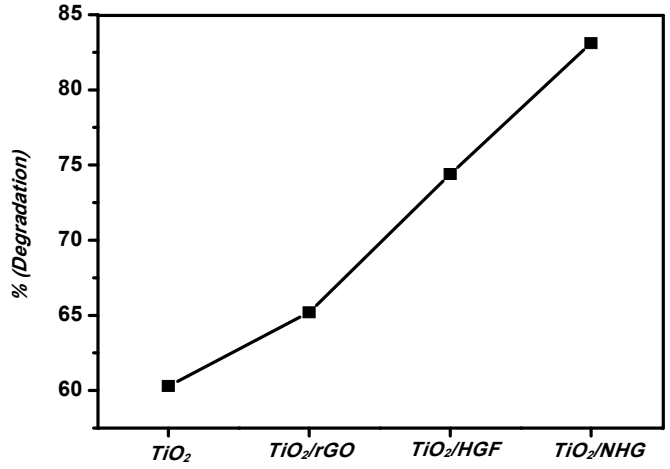

Figure 6.10: Performance of Different Photocatalysts Towards the Oxidative Degradation of Cefixime under Sunlight Irradiation for One Hour (Cumulated Light Energy = 2.26 kWh).

Detailed calculation of cumulated light energy was described in the section 2.6.3.1in Chapter 2. The details of optimisation studies of various operational parameters of this reaction were as follows.

6.3.2.1.2 Effect of Catalyst Loading

When the catalyst weight was increased from 0.025g to 0.05g, the photocatalytic degradation was found to get accelerated. The rate of photocatalytic degradation was supposed to increase with amount of catalyst because of the creation of more photo-excitation centres. However, with further increase in the amount of catalyst, a reduction in the light intensity in water by light absorption and scattering by the catalyst particles was resulted. This overall intensity reduction

adversely affected the photocatalytic process. The results obtained are summarised in Figure 6.11.

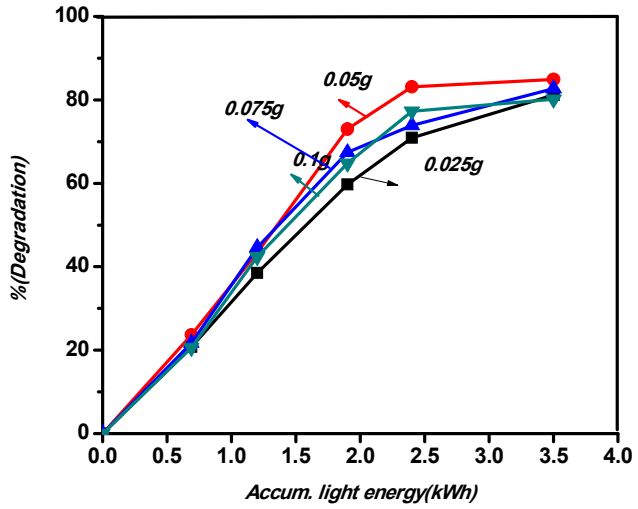

Figure 6.11: Optimization Studies of Catalyst Weight Carried Out under Irradiation with Sunlight

6.3.2.1.3 Effect of Initial Antibiotic Concentration

How the photocatalytic degradation rate changed with initial antibiotic concentration was an important aspect of the present work. The initial cefixime concentration was decreased gradually from 250 mg/L to 25 mg/L employing 0.05g TiO_2 /NHG nanocatalyst and the results obtained are summarised in Figure 6.12.

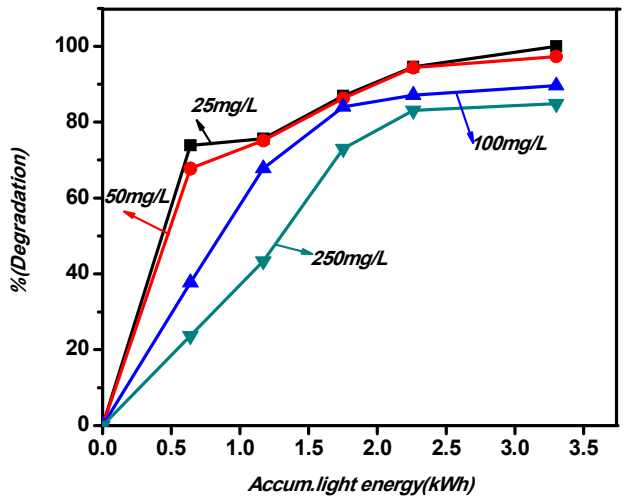

Figure 6.12: Effect of Initial Antibiotic Concentration

From Figure 6.12, we can see that degradation was comparatively easier with a decrease in the initial concentration of the antibiotic and its complete mineralization happened in 90 minutes of time when the initial concentration was decreased to 25 mg/L of cefixime. This can be considered as an important achievement as far as the antibiotic contaminated waste water treatment was concerned, because in effluents antibiotic concentrations were not expected to be generally high. In a photocatalytic degradation process, the production of active free radicals causing the degradation will be in a steady rate as long as the catalyst concentration and irradiation intensity does not vary. When the number of the organic molecules to be degraded was high initially, there would be an increased conception of these free radicals in the beginning itself which adversely affected their further degradation, as observed here.

6.3.2.1.4 Effect of H_2O_2 Addition

In general, addition of H_2O_2 was known to increase the rate of photocatalytic degradation process. The presence of H_2O_2 can accelerate the oxidative degradation in two different ways. It can accept photo-generated electrons from the catalyst and produce $OH^{\bullet}$ radicals. Additionally it can react with the superoxide radical anions to produce $OH^{\bullet}$ radicals. Both these factors were expected to accelerate the degradation process [60-62]. In order to find out an optimum value of the H_2O_2 initial concentration, the amount of H_2O_2 was varied gradually from 0 to 15 mg/L keeping all other parameters constant (250 mg/L cefixime concentration, 0.05 g TiO_2/NHG nanocatalyst, 100 ml reaction mixture). The results obtained are shown in Figure 6.13. When 5 mg/L H_2O_2 was present, the degradation after 90 minutes sunlight irradiation increased from 83.7% to 92.3%. However further addition of H_2O_2 did not improve the percentage of degradation, rather a decrease was observed. This may be possibly due to the reaction of excess H_2O_2 with $OH^{\bullet}$radicals which adversely affected the degradation process. The $OH^{\bullet}$ as well as hole scavenging to produce $HO_2^{\bullet}$might have slowed down the degradation.

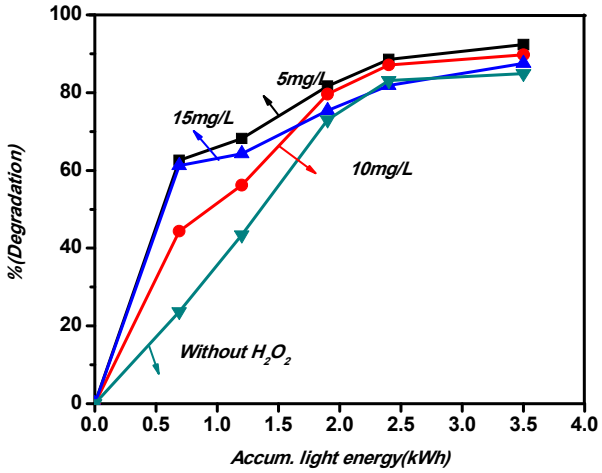

Figure 6.13: Effect of H_2O_2Concentration

6.3.2.1.5 Recyclability of TiO_2/NHG Photocatalytic System

In order to evaluate the recyclability of the TiO_2/NHG photocatalyst, three repeated cycles of photocatalytic degradation of cefixime (25 mg/L concentration) was performed under 90 minute sunlight irradiation employing the utilized and recovered photocatalyst (Figure 6.14). In the third run, there was a slight reduction in the percentage degradation from 100 to 96, probably due to the commencement of photo-oxidation of the NHG nanosheets to a small extent.

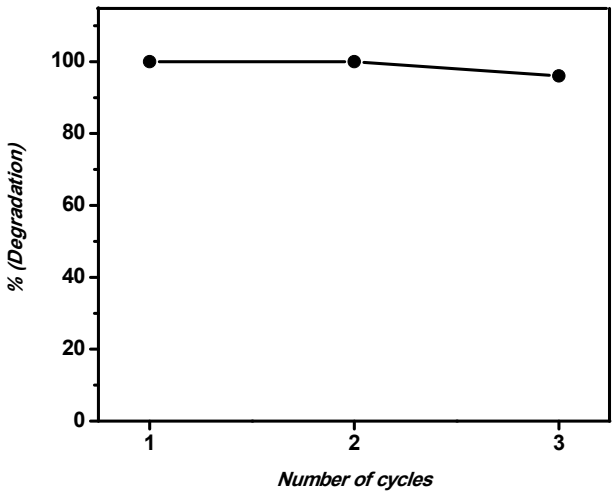

Figure 6.14: Number of Photocatalytic Cycles

6.3.2.2 Photocatalytic Water Splitting Studies

The procedure of the hydrogen evolution by water splitting reaction was described in the section 2.6.4 in the Chapter 2. It was monitored by recording the gas chromatogram for every one hour interval. The experiment was continued for a total of 5 hours.

6.3.2.2.1 Comparison of Hydrogen Evolution with TiO_2/NHG and Commercial p25 TiO_2Catalysts

The photocatalytic hydrogen production plots against time for the prepared TiO_2/NHG nanocomposite materials are provided in figure 6.15. In the case of TiO_2/NHG, it was observed that the hydrogen production rate kept on increasing up to 3h, then decreased. In both cases, the initial hydrogen production rate was low followed by

an increase. However, the TiO_2/NHG nanocomposite was found to be superior compared to commercial p25 TiO_2 calcined at 250°C. which showed the least activity in the hydrogen production.

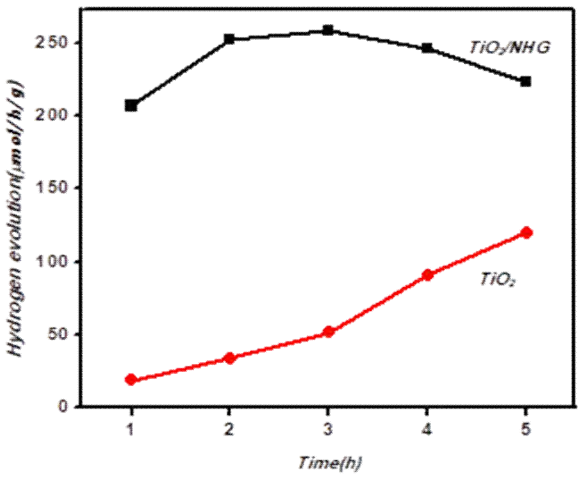

Figure 6.15: Comparison of Hydrogen Evolution with TiO_2/NHG and Commercial p25 Catalyst.

6.3.2.2.2 Effect of Catalyst Weight

The effect of catalyst weight on the hydrogen production was studied by varying the catalyst weight alone keeping all the other parameters constant. The hydrogen production experiment was carried out with TiO_2/NHG catalyst taken in seven different amounts (0.05 g, 0.075 g, 0.1 g, 0.15 g, 0.2 g, 0.25 g and 0.3 g) with 10 ml methanol as sacrificial agent and 40 ml water. Initially the hydrogen production rate was observed to increase with an increase in the amount of the catalyst up to 0.25 g when the light irradiated. Then there was a decrease in hydrogen production when the catalyst weight further increased to

0.3 g. The production was maximum when the catalyst weight was 0.25 g. The results of studies on catalyst loading are summarized in figure 6.16. The hydrogen production rate was expected to increase with amount of catalyst because of the presence of large number of photo-excitation centers created. However, with more loading, the catalyst particles make the reaction mixture more opaque by light absorption and scattering, as described by Beer–Lambert Law which was observed here.

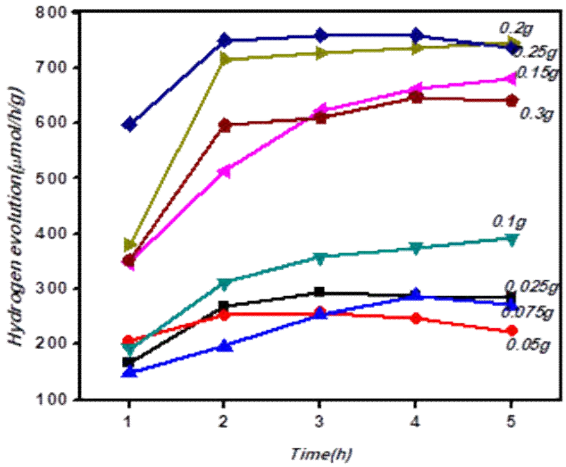

Figure 6.16: Effect of Catalyst Weight on Hydrogen Evolution Using TiO_2/NHG Catalyst

6.3.2.2.3 Performance of Different Catalysts

Photocatalytic reactions were carried out with different catalysts such as TiO_2/HGF, TiO_2/rGO and TiO_2/NHG taking 0.25 g catalyst weight and the results obtained are provided in the figure 6.17. The hydrogen production rate of the TiO_2 /NHG was observed to be

less than that of TiO_2/rGO, and TiO_2/HGF. For TiO_2/NHG, the maximum observed hydrogen production rate was only 1.748 mmol/g/h. These results showed that nitrogen doping of co-catalyst has a detrimental effect on the performance of the photocatalyst for water splitting reaction as far as the broad band irradiation with high pressure mercury lamp was concerned. A visible light irradiation source was expected to improve the hydrogen generation via this particular reaction using the TiO_2 /NHG photocatalytic system.

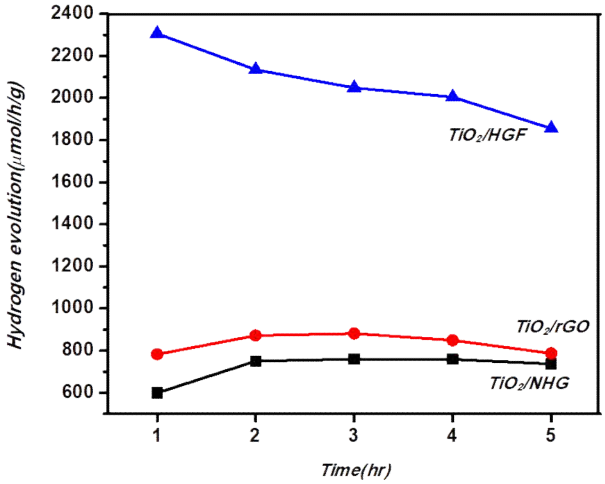

Figure 6.17: Performance of Different Photocatalysts Towards Water Splitting

6.3.2.2.4 Effect of NHG Loading in the Catalysts

The photocatalytic water splitting reactions were carried out with three different TiO_2/NHG catalysts in which the percentage of NHG was varied and the results are provided in the figure 6.18. TiO_2/NHG (5%) showed better performance than TiO_2/NHG (2%) and

TiO_2/NHG (10%). The findings are similar to that of TiO_2/HGF system, described in the previous chapter. Beyond a certain limiting value NHG loading did not enhance the photocatalytic performance, probably as a result of the masking of photocatalytically active TiO_2 nanoparticles by the NHG sheets present in excess.

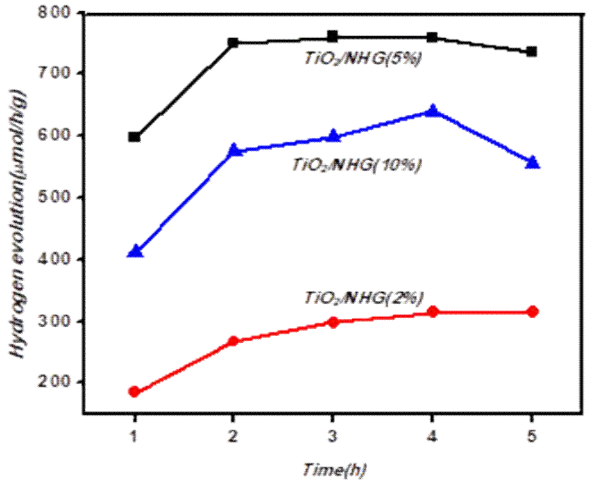

Figure 6.18: Effect of Graphene Loading in the Catalysts

6.3.2.2.5 Effect of Amount of Sacrificial Agent

Sacrificial reagents are better electron donors capable of reacting with photogenerated holes than water molecules. Their effect were studied performing the water splitting reaction with TiO_2/NHG taking 0.25 g catalyst weight varying the water methanol ratios and the results obtained are provided in the figure 6.19. The hydrogen production rate was improved when the methanol: water ratio increased from 1:4 to 2:3. However, further increase in the methanol

content decreased the hydrogen production rate which are presented in the figure 6.19. The surface blocking of the catalyst by the sacrificial agent probably might have caused the lower hydrogen production rate when the initial concentration of the sacrificial reagent was more. A 20 ml methanol and 30ml water mixture gave the best results.

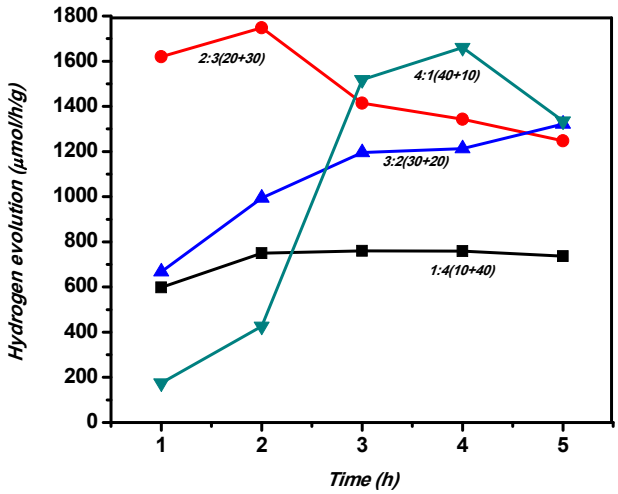

Figure 6.19: Effect of Amount of Sacrificial Agents on Hydrogen Evolution

6.4 Conclusions

In the present study, we demonstrated the practical applicability of photocatalytic degradation of antibiotics under exposure to sunlight, as an effective method towards the environmental cleaning up process, absolutely essential for curtailing the hazard of increasing antibiotic resistant bacterial strains. We have also performed a detailed study of the hydrogen production via water splitting reaction with the prepared TiO_2/NHG photocatalytic system. In the antibiotic degradation

studies, the commercial Degussa P25 TiO_2 catalyst was found not effective enough to perform a complete mineralization of the cefixime antibiotic under sunlight irradiation within 90 minutes of time. TiO_2/NHG nanocomposite showed excellent performance towards the oxidative degradation of cefixime with sunlight. The oxidative degradation rate of cefixime was found to be affected by various factors such as catalyst loading, initial antibiotic concentration, presence of H_2O_2 and so on. The nanocatalyst showed good recyclability without much decline in the activity levels up to three repeated cycles. The fact that complete mineralization of the antibiotic was achieved in a reasonable time span with naturally available and inexpensive sunlight irradiation, even without the presence of H_2O_2, can be considered as the major highlight of this work. This was the most promising aspect which offers the prospect of up-gradation of this process to a pilot scale as well as to commercial scale for the treatment of waste water with antibiotic contamination.

The photocatalytic water splitting reaction was done under 450 W high pressure mercury lamp irradiation was also studied using the same catalyst. It was found that nitrogen doping of holey graphene framework was having a detrimental effect in this case. We could achieve a maximum of only 1.748 mmol/g/h of hydrogen production. However, we think that if a photocatalytic water splitting reaction set up suitable for sunlight harvesting was developed, the TiO_2/NHG catalyst will perform excellently leading to a more economically viable technology for the green production of hydrogen.

References

1. J. Romao, D. Barata, N. Ribeiro, P. Habibovic, H. Fernandes and G. Mul, *Environ. Pollut.,* 2017, **220**, 1199-1207.

2. E. Adamek, W. Baran and A. Sobczak, *Process. Saf. Environ. Prot.,* 2016, **103**, 1-9.

3. T. W. Tzeng, S-L.Wang, Ch-Ch. Chen, Ch-Ch. Tan, Y-T. Liu, T. Y. Chen, Y-M. Tzou, C. C. Chen and J. T. Hung, *RSC Adv.,* 2016, **6**, 69301-69310.

4. C. Bojer, J. Schöbel, T. Martin, M. Ertl, H. Schmalz and J. Breu, *Appl. Catal. B Environ.,* 2017, **204**, 561-565.

5. M. A. Sousa, C. Gonçalves, V. J. P. Vilar, Rui. A.R. Boaventura and M. F. Alpendurada, *Chem. Eng. J.,* 2012, **198–199**, 301-309.

6. A. Bernabeu, R. F.Vercher, L. Santos-Juanes, P. J. Simon, C. Lardin, M. A. Martinez, J. A. Vicente, R. Gonzalez, C. Llosa, A. Arques and A. M. Amat, *Catal. Today.*, 2011, **161**, 235-240.

7. B. Ambrosetti, L. Campanella and R. Palmisano, *J. Environ. Sci. Eng. A.,* 2015, **4**, 273-281.

8. K. Vignesh, M. Rajarajan and A. Suganthi, *Mater. Sci. Semicond. Process.,* 2014, **23**, 98-103.

9. N. P. Xekoukoulotakis, N. Xinidis, M. Chroni, D. Mantzavinos, D. Venieri, E. Hapeshi and D. Fatta-Kassinos, *Catal. Today.,* 2010, **151**, 29-33.

10. V. Vaiano, O. Sacco, D. Sannino and P. Ciambelli, *Chem. Eng. J.*, 2015, **261**, 3-8.

11. Z. Xu, T. Wu, J. Shi, K. Teng, W. Wang, M. Ma, J. Li, X. Qian, C. Li and J. Fan, *J. Membr. Sci.,* 2016, **520**, 281-293.

12. A. Y. Malkhasian, M. Izadifard, G. Achari and C. H. Langford, *J. Environ. Sci. Heal. B.,* 2014, **49**, 35-40.

13. D. Li and W. Shi, *Chin. J. Catal.,* 2016, **37**, 792-799.

14. N. K. Eswar, P. Ramamurthy and G. Madras, *New J. Chem.,* 2016, **40**, 3464-3475.

15. N. Shao, J. Wang, D. Wang and P. Corvini, *Appl. Catal. B. Environ.,* 2017, **203**, 964-978.

16. M. Faraldos and A. Bahamonde., *Catal. Today.,* 2017, **285**, 13-28.

17. C. Xu, X. He, C. Wang, X. Chen, R. Yuan and W. Dai, *RSC Adv.*, 2016, **6**, 84068-84073.

18. M. Patel, W. Feng, K. Savaram, R. M. Khoshi, R. Huang, J. Sun, E. Rabie, C. Flach, R. Mendelsohn, E. Garfunkel and H. He, *Small*., 2015, **11**, 3358-3368.

19. Y. Lin, X. G. Han, C. J. Campbell, J. W. Kim, B. Zhao, W. Luo, J. Dai, L. Hu and J. W. Connell, *Adv. Funct. Mater.*, 2015, **25**, 2920-2927.

20. D. H. Deng, K. S. Novoselov, Q. Fu, N. F. Zheng, Z. Q. Tian and X. H. Bao, *Nat. Nanotechnol.,* 2016, **11**, 218-230.

21. Y. Qin, L. Chao, J. Yuan, Y. Liu., F. Q. Chu, Y. Kong, Y. X. Tao and M. L. Liu, *Chem. Commun.,* 2016, **52**, 382-385.

22. L. L. Jiang and Z. J. Fan, *Nanoscale.,* 2014, **6**, 1922-1945.

23. X. J. Bo, M. Li, C. Han, Y. F. Zhang, A. Nsabimana and L. P. Guo, *J. Mater. Chem. A.,* 2015, **3**, 1058-1067.

24. I. Michael, L. Rizzo, C.S. McArdell, C.M. Manaia, C. Merlin, T. Schwartz, C. Dagot, D. Fatta-Kassinos, *Water Res.,* 2013, **47**, 957-995.

25. I. T. Carvalho and L.Santos, *Environ. Int.,* 2016, **94**, 736-757.

26. P. Verlicchi, M. Al Aukidy, A. Galletti, M. Petrovic and D. Barceló., *Sci. Total Environ.,* 2012, **430**, 109-118.

27. M. Barza and S. L. Gorbach, editors (2002) The need to improve antimicrobial use in agriculture: ecological and human health consequences: a report of the facts about antibiotics in animals and the impact on resistance (FAAIR) project—The Alliance for the Prudent Use of Antibiotics., *Clin. Infect Dis.,***34** (Suppl 3), 71-144.

28. E. A. Belongia, B. J. Sullivan, P. H. Chyou, E. Madagame, K. D. Reed and B. Schwartz, *Pediatrics*., 2001, **108**, 575-583.

29. S. Mölstad, M. Erntell, H. Hanberger, E. Melander, C. Norman, G. Skoog, C. S. Lundborg, A. Söderström, E. Torell and O. Cars, *Lancet Infect Dis.,* 2008, **8**, 125-132.

30. K. D. Brown, J. Kulis, B. Thomson, T. H. Chapman and D. B. Mawhinney, *Sci. Total Environ.,* 2006, **366**, 772-783.

31. A. Samaneh, G. Elham and V. Alireza, *J. powtec*., 2016, **288**, 1-452.

32. J. Blackbeard, J. Lloyd, M. Magyar, J. Mieog, K. G. Linden, Y. Lester, *Environ Sci.:Water Res. Technol.,* 2016, **2**, 213-222.

33. E. S. Elmolla and M. Chaudhuri, *Desalination.,* 2010, **256**, 43-47.

34. W. R. Bowie, C. E. Shaw, D. G. W. Chan, J. Boyd and W. A. Black, *Antimicrob. Agents Chemother.,* 1986, **30**, 590-593.

35. R. Jain, V. K. Gupta, N. Jadon and K. Radhapyari, *Anal. Biochem.,* 2010, **407**, 79-88.

36. T. Wi, M. M. Lahra, F. Ndowa, M. Bala, J-AR. Dillon, P. Ramon-Pardo, S. R. Eremin, G. Bolan and M. Unemo, *PLoS Med.,* 2017, **14**, 1-16.

37. B. Issa, S. K. Ghodratollah, G. Hatam and A. Mohammad, *Desalin. Water Treat.*, 2014, 1-8.

38. S. Yurdakal, V. Loddo, V. Augugliaro, H. Berber, G. Palmisano and L. Palmisano, *Catal. Today.,* 2007, **129**, 9-15.

39. K. G. Carole, J. Marie and G. Michael, *J. Mol. Catal.*, 1990, **60**, 375-387.

40. E. D. Tusnelda and H. F. Fritz, *Water Res.*, 2004, **38**, 955-964.

41. M. Visalakshi, B. G. Susheela, V. Sinduri, G. Praveena, G. Ushasree and G. Swapna, *Adv. Nanomater. Emerg. Eng. Technol.,* 2013, 409-411.

42. P. Asieh and N.E. Alireza*, Chem Eng Res Des.,* 2015, **104**, 835-843.

43. M. S. Nawal and M. G. Mohsen, *Chem. Eng. J.,* 2017, **315**, 527-536.

44. A. Ali, D. Abdollah, M. Mitra, A. Ali, K. Amir, B. Fateme and S. Zahra*., IJPT.,* 2016, **8**, 16728-16736.

45. J. S. Jang, H. G. Kim and J. S.Lee, *Catal. Today.*, 2012, **185**, 270-277.

46. L. Shou-Heng and S. Han-Ren,*Appl. Energy.*, 2012, **100**, 148-154.

47. B. Wang, Q. Sun, S. Liu and Y. Li, *Int. J. Hydrogen. Energy.*, 2013, **38**, 7232-7240.

48. R. Dholam, N. Patel, M. Adami and A. Miotello, *Int. J. Hydrogen. Energy.*, 2008, **33**, 6896-6903.

49. J. H. Park, S. Kim and A. J. Bard, *Nano Lett*., 2006, **6**, 24-28.

50. M. A. Khan, S. I. Woo and O. B. Yang, *Int. J. Hydrogen. Energy.*, 2008, **33**, 5345-5351.

51. B. S. Kwak, J. Chae, J. Kim and M. Kang, *Bull. Korean Chem. Soc.*, 2009, **30**, 1047-1053.

52. H. Jeong, T. Kim, D. Kim and K. Kim, *Int. J. Hydrogen. Energy.*, 2006, **31**, 1142-1146.

53. A. Kudo, Catal. Surv. Asia., 2003, **7**, 31-38.

54. S. Onsuratoom, S. Chavadej and T. Sreethawong, *Int. J. Hydrogen. Energy.*, 2011, **36**, 5246-5261.

55. H. Chao-Wei, L. Chi-Hung, J. CS Wua, L. Yu-Chang, C. Chun-Ling, W. Chih-Hung, A. Masakazu, M. Masaya, T. Masato, *Int. J. Hydrogen. Energy.*, 2010, **35**, 12005-12010.

56. N. K. Muhammad and B. Javaid., *Sci. Res.*, 2011, **2**, 962-965.

57. Y. Shweta and J. Gautam, *J. Chin. Chem. Soc.,* 2017, **64**, 103-116.

58. Y. Shweta, S. MeenaKumari, K. V. Devendra and J. Gautam., *Adv. Nano. Energy.*, 2017, **1**, 73-89.

59. D. Usachov, O. Vilkov, A. Grüneis, D. Haberer, A. Fedorov, V. K. Adamchuk, A. B. Preobrajenski, P. Dudin, A. Barinov, M. Oehzelt, C. Laubschat, D. V. Vyalikh, *Nano Lett.* 2011**, 11***,* 5401–5407.

60. D. F. Ollis, E. Pelizzetti, N. Serpone, *Environ. Sci. Technol.*, 1991, **25**, 1523-1529.

61. Z. Yujing and F. Ramin, *Top. Catal.*, 2006, **37**, 2-4.

62. H. T. Dyi, C. J. Lain and H. H. Hsin, *Int. J. Photoenergy.,* 2012,**328526** (1-9) doi:10.1155/2012/328526.

Chapter 7

Summary and Conclusion

In the present chapter, our effort is to summarise the entire thesis work. The impotent conclusions and future prospects of this Ph. D project have been highlighted here.

7.1 Graphene Based Nanocomposite Catalysts

The present thesis focus on the metal oxide/ hydroxide - graphene nanocomposite catalytic systems prepared from different precursors and their utilisation for various catalytic applications including dechlorination of aryl halides, reduction reactions, photocatalytic antibiotic degradation and hydrogen production via water splitting reactions. All the heterogeneous catalysts were prepared in a cost effective manner via simple methods and the prepared systems were characterized by different analytical techniques in order to understand their structure, crystalline phase, nature and composition. Studies were also conducted to have a better understanding about the influence of different reaction parameters on these catalytic reactions.

7.2 Summary

Present study mainly focus on the preparation, characterization and catalytic activity studies of metal oxide/hydroxide - graphene nanocomposite materials. Different catalysts involved in the present investigation were $Ni(OH)_2$/rGO, ZnO/G, TiO_2/HGF and TiO_2/NHG nanocomposites. The thesis is structured as 7 chapters including the summary and conclusion chapter. The summaries of each chapter and the conclusions obtained are provided in brief in the following sections.

7.2.1 Chapter 1: Metal Oxide/Hydroxide - Graphene Nanocomposite Materials

The 1st chapter is a general introduction and literature review of metal oxide/hydroxide - graphene nanocomposite materials. Their importance, preparation methods, properties and applications are outlined in this chapter. A review of literature of nanocomposites in general and different types of graphene based nanocomposites in particular are briefly outlined here. Additionally, a brief general introduction to heterogeneous catalysis and mechanism of heterogeneous photocatalysis with semiconductors are described in this chapter. Objectives of the present work are also provided towards the end of this chapter.

7.2.2 Chapter 2: Experimental Methods and Characterization Techniques

Chapter 2 deals with the experimental methods and characterization techniques adapted for the present study. This chapter provides the details of the materials used throughout the study including their supplier/manufacturer etc. Also, the various preparation methods of different classes of metal oxide/ hydroxide catalysts decorated on reduced graphene oxide nanosheets and their designations are included here. Various characterization techniques used and their working principles are also outlined. The procedures adapted for the catalytic studies are included as well in this chapter.

7.2.3 Chapter 3: Nickel Hydroxide Platelets /Reduced Graphene Oxide ($Ni(OH)_2$/rGO) Nanocomposite and Its Catalytic Applications

The chapter 3 discuss the fabrication, characterizations and different catalytic applications of $Ni(OH)_2$/rGO nanocomposite. The catalyst preparation was straight forward which include a simple facile hydrothermal method and was found to be highly effective in the catalyst development. With the help of different characterisation techniques, it can be concluded that $Ni(OH)_2$ platelets were exfoliated and uniformly dispersed on the rGO sheets which made the nanocomposite a far superior catalyst compared to bare nickel hydroxide. $Ni(OH)_2$/rGO nanocomposite was found to be a highly efficient for the dechlorination reaction of dichlorobenzene to benzene and 1-chloronaphthalene to tetralin with 94.6% and 100 % conversion respectively in optimum reaction conditions. The reactants used were well known persistent pollutants. $Ni(OH)_2$/rGO nanocomposite also performed excellently for the reduction reaction of p-nitrophenol to p-aminophenol. When compared with bare $Ni(OH)_2$, the $Ni(OH)_2$/rGO nanocomposite attained the complete reduction of p-nitrophenol within 14 min of time whereas reaction with bare $Ni(OH)_2$ catalyst took 32 min. The high specific capacitance and remarkable cyclic stability of the $Ni(OH)_2$/rGO composite compared to that of the $Ni(OH)_2$ and rGO suggested that the material was better suited as electrode for

high-performance electrochemical pseudo capacitors than the individual components $Ni(OH)_2$ and rGO.

7.2.4 Chapter 4: Zinc Oxide/Graphene (ZnO/G) Nanocomposites and Their Photocatalytic Applications

In chapter 4, the preparations, characterizations and photocatalytic sunlight assisted mineralization studies of antibiotic cefixime with three different types of ZnO/graphene photocatalysts are provided. Bare ZnO catalyst was found to be not effective enough to perform the mineralization of the cefixime antibiotic under sunlight irradiation. ZnO/rGO nanocomposite prepared via hydrothermal route showed better performance towards the oxidative degradation of cefixime with sunlight irradiation than the ones prepared via microwave irradiation and liquid phase exfoliation. A 71.1% mineralisation of the antibiotic in 25mg/L concentration was observed within 120 minutes irradiation for the H-ZnO/rGO nanocomposite material. The oxidative degradation rate of cefixime was found to be affected by various factors such as catalyst loading, initial antibiotic concentration, presence of H_2O_2 and so on. The H-ZnO/rGO showed better photocatalytic performance under 450W high pressure mercury lamp irradiation with 88% degradation.

7.2.5 Chapter 5: Preparation of TiO_2/Holey Graphene Framework Nanocomposites and Their Application as Photocatalysts in Water Splitting Reaction

5^{th} chapter deals with the preparation of TiO_2/HGF nanocomposites, their characterization studies and application of these

catalytic systems in the photocatalytic hydrogen production reaction via water splitting. Titania was mechanically mixed with holey graphene to prepare the powder TiO_2/HGF catalyst. The photocatalytic water splitting was studied by varying various parameters of the reaction such as catalyst weight, HGF loading in the catalyst and concentration of the sacrificial agent, etc. With holey graphene titania nanocomposite, we could achieve a maximum of 2.306 mmol/g/h of hydrogen production rate . The present study demonstrated that HGF can be a suitable co-catalyst in the titania based photocatalytic systems for the photocatalytic water splitting reaction.

7.2.6 Chapter 6: TiO_2/Nitrogen Doped Holey Graphene Nanocomposite and Its Photocatalytic Applications

In the chapter 6, the preparation and characterization of TiO_2/NHG nanocomposite and its photocatalytic applicationsare described. The photocatalytic degradation of antibiotics under exposure to sunlight is necessary in the present scenario especially due to the increasing demand for an urgent control of increasing antibiotic resistant bacterial strains threatening humanity. We have also presented a detailed study of the hydrogen production via water splitting reaction with the prepared TiO_2/NHG photocatalytic system. In the antibiotic degradation studies, the commercial Degussa p25 TiO_2 catalyst was found not effective enough to perform a complete mineralization of the cefixime antibiotic under sunlight irradiation within 90 minutes of time whereas the TiO_2/NHG nanocomposite showed excellent performance towards the complete oxidative

degradation of cefixime with sunlight within 90 min. of time. The oxidative degradation rate of cefixime was found to be affected by various factors such as catalyst loading, initial antibiotic concentration, presence of H_2O_2 and so on. The nanocatalyst showed good recyclability without much decline in the activity levels up to three repeated cycles.

Nitrogen doping of holey graphene framework was found to have a detrimental effect in the photocatalytic water splitting reaction under 450 W high pressure mercury lamp irradiation. We could achieve a maximum of only 1.748 mmol/g/h of hydrogen production with TiO_2/NHG nanocatalyst.

7.2.7 Chapter 7. Summary and Conclusions

The 7th chapter summarized the results of the present work and concluded the thesis.

7.3. Conclusions

From the present study, the following major conclusions can be made.

- $Ni(OH)_2$/rGO nanocomposite was found to be a highly efficient for dechlorination reaction of aryl chlorides, which are well known persistent pollutants and also for the reduction reaction of p-nitrophenol.
- As part of the global efforts to contain the growth of antibiotic resistant bacteria, three different types of ZnO/graphene

photocatalysts were employed for the sunlight assisted mineralization of antibiotic cefixime and the photocatalyst prepared in a hydrothermal route was found to be superior.

- TiO_2/Holey graphene framework (TiO_2/HGF) nanocomposite showed very good performance in the photocatalytic hydrogen generation via water splitting with a maximum of 2.306 mmol/g/h of hydrogen production.

- Nitrogen doping of holey graphene framework was found to be less beneficial in the photocatalytic water splitting reaction under 450 W high pressure mercury lamp irradiation since we could obtain a maximum of only 1.748 mmol/g/h of hydrogen production with TiO_2/NHG nanocatalyst .

- However, the TiO_2/NHG nanocatalyst performed excellently in the photocatalytic degradation of cefixime under sunlight irradiation and a 100% degradation could be achieved within 90 min of irradiation time.

7.4. Future Outlook

The prepared heterogeneous metal oxide/hydroxide- graphene nanocomposite materials showed excellent catalytic activities and possess the prospect for their commercial production. $Ni(OH)_2$/rGO catalyst could be a highly suitable catalyst for CVOC removal technology and can be easily turned out to be an industrially important one. TiO_2/HGF and TiO_2/NHG catalysts could perform excellently as

photocatalysts for solar energy harvesting leading to a more economically viable technology for the green production of hydrogen. Similarly, TiO_2/NHG and H-ZnO/rGO also performed very well as effective catalysts towards antibiotic degradation and can easily fit in to the environmental cleaning up process, absolutely essential for curtailing the hazard of increasing antibiotic resistant bacterial strains. Especially the use of TiO_2/NHG photocatalyst offers the prospect of up-gradation of this process to a pilot scale as well as to commercial scale for the treatment of waste water with antibiotic contamination. Present investigation has its own significance for the development of economically viable technologies. It should be noted that throughout our investigation, the production of catalysts were carried out via simple and facile routes.

List of Publications

Publication

1. C. P. Shaniba, M. Akbar, K. K. Ramseena, P. Raveendran, N. N. Binitha, M. R. Resmi, Sunlight-assisted oxidative degradation of cefixime antibiotic from aqueous medium using TiO_2/nitrogen doped holey graphene nanocomposite as a high performance Photocatalyst, *Journal of Environmental Chemical Engineering*, 2018, DOI: 10.1016/j.jece.2018.02.012.

Paper Communicated/under Preparation

1. Exfoliated $Ni(OH)_2$ Nano Platelets Anchored on Graphene : An Efficient Catalyst for the Reductive Dechlorination of Aryl Chlorides, C. P. Shaniba, P. Raveendran, N. N. Binitha and M. R. Resmi.

2. Titania/Holey Graphene Framework Nanocomposite: An Efficient Photocatalyst for the Hydrogen Production via Water Splitting, C P Shaniba, Mohammed Akbar, P Raveendran, B N Narayanan and M R Resmi.

List of Papers Presented

1. C. P. Shaniba, M. R. Resmi, Hydrothermal Preparation of ZnO Nanorod/Reduced Graphene Oxide Nanocomposites and Their Application for the Sunlight Driven Photocatalytic Degradation of Cefixime Antibiotic, National seminar on Emerging Trends in Nonmaterial's Science and Technology (ENST-2017), Research and Post Graduate Department of Chemistry, Sree Neelakanta Government Sanskrit College Pattambi, Palakkad, 19-20 December 2017.

2. K. K. Ramseena, C. P. Shaniba, P. Mohammed Akbar, U. Rajeena, N. N. Binitha And M. R. Resmi, Synthesis Of Nitrogen Doped Holey Graphene and Its Application as an Efficient Catalyst for the Reduction of Nitro Arenes in to Aromatic Amines, National seminar on Emerging Trends in Chemical Research, Research and Post graduate Department of Chemistry, Christ College (autonomous), Irinjalakuda, 28 February – 1 March 2017.

3. C. P. Shaniba, E. Jijitha, K. Pranitha, P. Mohammed Akbar, U. Rajeena, N. N. Binitha, M. R. Resmi, A Facile Route for the Synthesis of GO/$Ni(OH)_2$ Nanocomposites and Its Catalytic Application, National seminar on Computational Chemistry(NSCC-2016), Post graduate Department of Chemistry, KAHM Unity Women's College, Manjeri, 20-21 January 2016.

4. M. Aswathy, C. P. Shaniba, P. Mohammed Akbar, M. R. Resmi, Synthesis and Charecterisation of Conductive Graphene/Polyaniline Nanocomposites, National seminar on Recent Advances in Chemistry, Department of Chemistry, M.E.S Ponnani college, Ponnani,2-3 September 2014.